A Nanomechanical Investigation of the Crack Tip Process Zone of Marble

by

Zenzile Brooks

B.S., University of Southern California (2007)

Submitted to the Department of Civil and Environmental Engineering in Partial Fulfillment of the Requirements for the Degree of

Master of Science in Civil and Environmental Engineering
at the Massachusetts Institute of Technology

June 2010

Signature of Author: _____
Department of Civil and Environmental Engineering
May 7, 2010

Certified by: _____
Herbert Einstein
Professor of Civil and Environmental Engineering
Thesis Co-Supervisor

Certified by: _____
Franz-Josef Ulm
Professor of Civil and Environmental Engineering
Thesis Co-Supervisor

Accepted by: _____
Daniele Veneziano
Chairman, Departmental Committee for Graduate Students

A Nanomechanical Investigation of the Crack Tip Process Zone of Marble

by

Zenzile Brooks

Submitted to the Department of Civil and Environmental Engineering
on May 7, 2010, in partial fulfillment of the
requirements for the degree of
Master of Science in Civil and Environmental Engineering

Abstract

This study explores the interaction between crack initiation and nanomechanical properties in the crack tip process zone (zone of microcracking at the tip of a propagating crack) of a brittle geomaterial. Samples of Carrara marble with pre-existing cracks ("flaws") were loaded in a uniaxial testing machine until the process zone appeared at the tips of the pre-existing cracks in form of "white patching". Three techniques were then used to obtain nanomechanical properties of the process zone and relate them to macroscale crack initiation: digital photography, to visually assess the macrostructure and crack formation, environmental scanning electron microscopy (ESEM), to visually assess microstructure, and nanoindentation, to yield nanomechanical properties and assess nano/microheterogeneities. Nanoindentation testing was comprised of lines and grids of single nanoindentations located both near and far from the process zone. The purpose of nanoindentation testing is to investigate the underlying trend in nanomechanical property change between intact and process zone marble. Analysis of nanoindentation testing results showed a decrease of both modulus and hardness (a) near grain boundaries in intact material, and (b) with closeness to the process zone. Ultimately, the study confirms that the crack tip process zone manifests itself as an area of reduced nanomechanical properties in marble.

Thesis Co-Supervisor: Herbert Einstein
Title: Professor of Civil and Environmental Engineering

Thesis Co-Supervisor: Franz-Josef Ulm
Title: Professor of Civil and Environmental Engineering

Contents

Acknowledgments

An ancient proverb reminds us, "He that would have the fruit, must first climb the tree." I would like to thank all who have helped me to climb the first branches of this tree.

Firstly, to Professors Franz-Josef Ulm and Herbert Einstein, your wisdom and guidance have provided me a rich learning experience; thank you for your mentorship. Secondly, to the members of the Rock Mechanics and Nanomechanics research groups at MIT, I am proud to share a lab, an office, and a project with such brilliant thinkers; thank you for your support and your enthusiasm. I send special thanks to Khalea Ross Robinson and Sara John; their excellent work and tireless spirits greatly enhanced this project, and greatly motivated me. Hayami Arakawa and Ken Stone of the MIT Hobby Shop, Dr. Libby Shaw and Patrick Boisvert of the MIT Center for Materials Science and Engineering, Dr. Brian Evans of the MIT Department of Earth, Atmospheric, and Planetary Sciences, and Alan Schwartzman of the MIT Nanolab have also made invaluable contributions to this project.

To my friends and colleagues all over this campus and beyond, you inspire me daily in more ways than you know; thank you.

Finally, to my mother, my father, and my sister, from my very first steps to my very latest late-night phone calls – "thank you" seems not enough to cover all that you have done for me, so I will also add this: I love you, and this is for you.

Chapter 1

Introduction

1.1 Industrial Problem

This thesis addresses cracking mechanisms in geomaterials; these cracking mechanisms lead to failure at a variety of scales. At the scale of plate tectonics, cracking is the underlying mechanism of faulting, and thus earthquakes [21] [71]. Faults in rock masses lie further down on the macro scale, but may pose an equally important threat. These fractures initiate slope failures that may induce landslides. This scale of crack also applies to underground structures such as tunnels, radioactive waste disposal facilities, petroleum reservoirs, and power plants [45] [40] [63].

A fracture crack at any scale probably begins at the nanoscale. Recent advances in nanotechnology allow one to understand processes at this fundamental scale. Application of nano-investigative techniques to cracking processes in geomaterials will help engineers to thoroughly understand, and ultimately design solutions to control, cracking of geomaterials. Given the presence of geomaterial cracking at so many scales, the understanding and control of cracking provided by such a nanoscale investigation is crucial to the success of the structural, geotechnical, and geophysical engineering industries.

1.2 Research Question

Scientists and engineers have assessed cracking for many years. From theoretical approaches to experimental approaches, there exist nearly as many methods of analyzing a crack as there exist cracks. The red thread shared by nearly all approaches is the pursuit of the extent and type of damage caused by cracks.

Hence, the damage caused by cracks in a geomaterial is the main topic of this study. This study focuses on the process zone in particular; the process zone is a zone of damage near the tip of a propagating crack (more detail in Section 2.2). With the type of geomaterial damage thusly defined for the study, the study explores the answers to three compelling research questions:

What fundamental micro-mechanism controls the cracking of a brittle material? Does the mechanism drive cracking, retard cracking, or both? What is the precise scale of this micro-mechanism?

An assessment of the mechanism at a small scale will provide insights into crack behavior at larger scales.

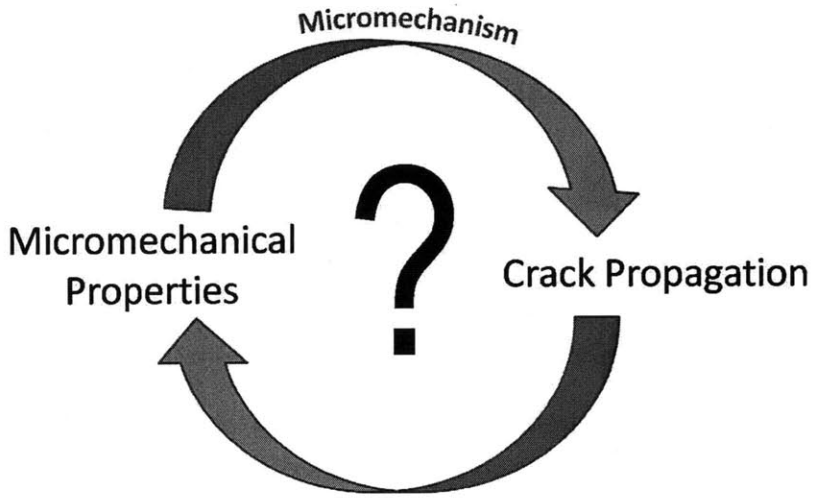

Figure 1-1: A schematic of the Research Question. The study assesses micromechanical properties as a means of probing the micromechanism which controls crack propagation.

1.2.1 Research Objectives

A thorough investigation of cracking micromechanisms will cross the disciplines of materials science, classical mechanics, rock mechanics, and geology. The attainment of several research objectives marks the course of the investigation:

Objective 1: Develop a multi-disciplinary investigative technique to assess both intact and process zone material. A robust and exhaustive technique must be developed in order to compare the relevant properties of different types of material. This technique will probe both structure and mechanical properties at the most fundamental scale of the experimental material.

Objective 2: Assess the fundamental properties (microstructure, nanoindentation response) of both intact and process zone material. The developed technique must be applied to the material in order to actually obtain – and thereby assess – the relevant properties. This assessment will combine visual and mechanical investigative techniques in order to thoroughly understand microproperties of the material within the process zone, in close proximity to the process zone, and far from the process zone. Anisotropy will also be assessed by visually and mechanically investigating at different orientations.

Objective 3: Identify the micro-mechanism at play in the process zone. An identification of the fundamental cause of cracking links the current study with the future designs of solutions to control cracking. Trends in microproperty change near the crack tip process zone of marble provide powerful clues of the mechanism which controls cracking. The scale and rate of microproperty change near crack tip process zone will be determined by comparison of all investigative results.

1.3 Outline of Thesis

The first chapter of this thesis (Chapter 1: Introduction) places the study into the practical and scientific context. The second chapter (Chapter 2: Background) provides a review of existing work in two areas: the process under investigation (the cracking of brittle materials), and the investigative techniques (nanoindentation and environmental scanning electron microscopy,

ESEM) used to explore this process. This chapter also defines key terms used throughout the study. The third chapter (Chapter 3: Method) explains how the two investigative techniques were applied. The next chapter (Chapter 4: Results) presents, expands, and discusses the results obtained by each investigative technique. Chapter 5: Analysis and Discussion highlights the findings, and reconnects them with the original research question; this section presents the first answers to this motivating question. The final chapter (Chapter 6: Summary and Perspectives) links the results of the study back to the larger scientific and practical context, and charts out the next steps in this particular research area.

Chapter 2

Background

The current investigation is composed of three key elements: nanomechanical properties, process zone, and geomaterials. Although each element has been pursued individually in the literature, this study presents the first occasion to bring these elements together in such a way. A full understanding of each element, as presented in this chapter, provides a solid foundation for the investigation before it explores the answer to the fundamental question of the scale, type, and behavior of micromechanism that drives the cracking of geomaterials.

2.1 Nanomechanical Properties

This section explains how nanoindentation provides the first element of the study: nanomechanical properties. Nanoindentation is an ideal method for probing the mechanical response of a material at fundamental scales. Included is a discussion of the self-similarity of nanoindentation; this property of nanoindentation aids with and streamlines the analysis. The section closes with a brief review of existing applications of nanoindentation to brittle materials.

2.1.1 Nanoindentation Procedure

The Nanoindentation Test

Nanoindentation tests in this investigation were conducted on a CSM Instruments Nano-Hardness Tester© (Figures 2-1, 2-2). An indentation test consists of pushing a probe onto a specimen surface at a specified loading rate and peak load (Figure 2-3; [10]). Figure 2-3

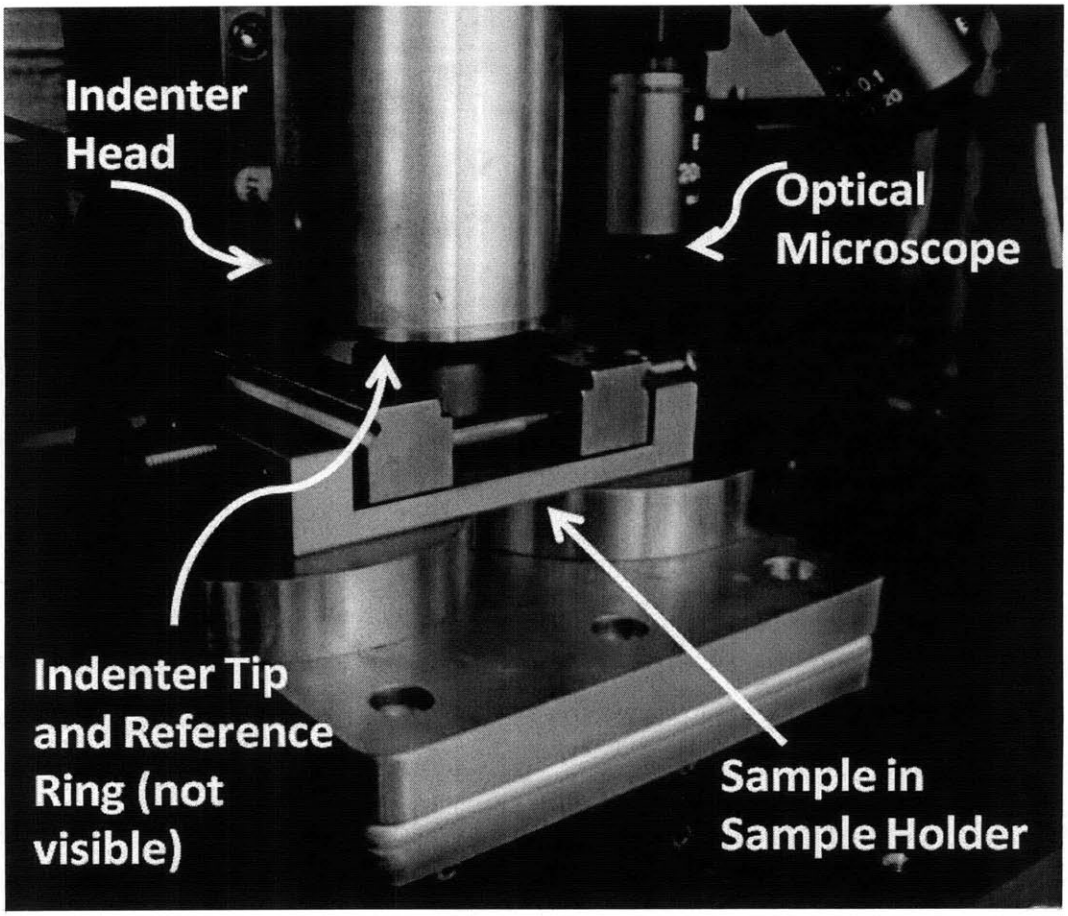

Figure 2-1: The CSM Instruments Nano-Hardness Tester©. A cross-section of the indenter head is presented in Figure 2-2.

depicts the geometry of the surface before and during indentation for a conical probe. Before indentation, the surface is assumed to be infinitely flat. During indentation, the tip of the indenter deforms the surface to an "indentation depth" h at a maximum load P, where h is measured from the surface before indentation to the maximum depth during loading. The actual height of contact between indenter probe and material is denoted by h_c; h_c is also known as the "contact depth". The projection of the region of indenter-surface contact at maximum load onto the original undeformed surface is the contact area, A_c.

The particular deformation of the surface during indentation reveals information about the stress-strain behavior and strength of the indented material. This information is contained in

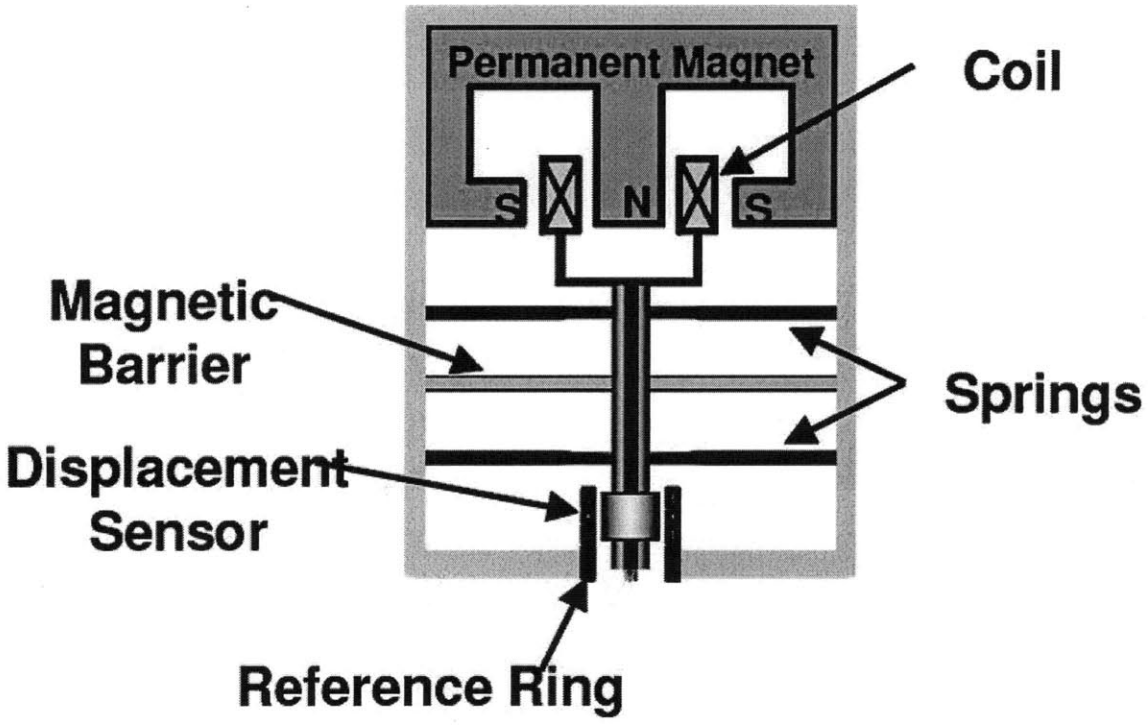

Figure 2-2: Cross-section of components of CSM Instruments Nano-Hardness Tester© Indenter Head (Figure 2-1). The specimen is placed beneath the reference ring; the reference ring contacts the specimen surface prior to each indentation. From [10].

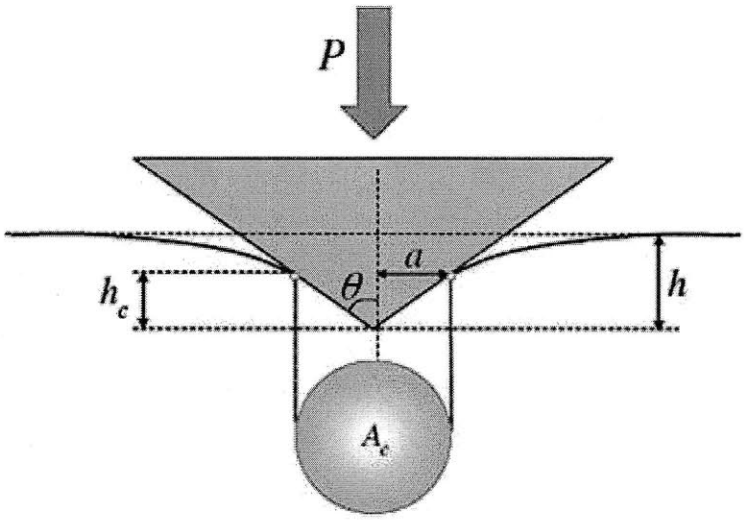

Figure 2-3: This diagram of a typical conical probe indentation indicates contact depth h_c, indentation depth h, contact radius a, equivalent cone angle θ. From [10].

two of the material properties yielded by nanoindentation: indentation modulus, and indentation hardness. The details of these properties are explained throughout this section. Nonetheless, during each indentation, surface deformation is monitored via a force-depth curve (Figure 2-4).

The important physical quantities which constitute indentation modulus and indentation hardness formulation are obtained from the force-depth curve.

Calibrations[1]

Accuracy of Nano-Hardness Tester data relies upon calibration of four components. Firstly, the springs indicated in Figure 2-2 are the key components in determining the force-depth curve. The spring constants of these springs must be determined annually with a spring calibration. Secondly, the platform which holds the sample must translate the sample from beneath the optical microscope to beneath the indenter head with minimal error. This user-performed calibration is conducted when the machine undergoes a major change, such as replacement of the probe. Thirdly, the probe is critical to accurate indentation analysis, but the particular

[1] **This discussion of this section inspired by that of [10].**

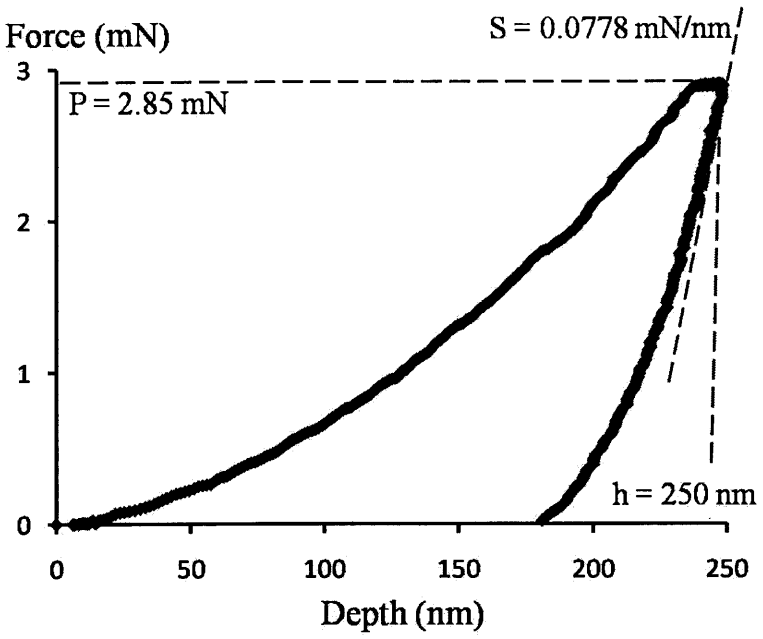

Figure 2-4: Force-indentation depth curve of an indentation test into marble. The important physical quantities which determine indentation modulus and hardness are obtained from this curve.

probe geometry blunts over time and with extensive use. The probe area function calibration is user-performed several times a year by conducting indents in a material of known properties, such as fused silica. Finally, the compliance of the entire machine is fixed and based on the reference design provided by CSM.

2.1.2 Self-Similarity of Indentation Test

The self-similarity of any research problem is of value to the researcher. For a time-dependent process such as indentation, self-similarity means that a similarity transformation can relate the distribution of properties in space at one point in time to that of the properties at another point in time [6]. In particular, the displacement fields at a particular load P_0 can help determine the displacement fields at any load P.

Indentation meets self-similarity [11], provided the particular indentation test satisfies three established criteria. Firstly, the strains and stresses of the indenter material follow homogenous constitutive relations; the operator F of these constitutive relations is described by homogenous,

degree κ functions with respect to the components of the strain tensor $\boldsymbol{\varepsilon}$ (and strain rates $\dot{\boldsymbol{\varepsilon}}$):

$$F(\lambda\boldsymbol{\varepsilon}) = \lambda^{\kappa} F(\boldsymbol{\varepsilon}) \tag{2.1}$$

Secondly, the shape of the indenter must be a homogenous function of degree $d = 1$ or greater. The height z of the surface of the probe in the indented material thus must follow:

$$z(\lambda x_1, \lambda x_2) = \lambda^{d} z(x_1, x_2) \text{ with } \lambda > 0 \tag{2.2}$$

The expression assumes a Cartesian coordinate system $Ox_1x_2x_3$ with the origin at the tip of the probe (and x_3 into the depth of the probe; z is measured along x_3). Third and finally, the load must always increase during the test. Upon load decrease, the indentation problem no longer meets the conditions of self-similarity, except in the case of elastic material behavior.

As a result of satisfying self-similarity, indentation analysis is simplified: straighforward scaling relations describe contact area or depth as a function of known homogenous functions and initial contact area or depth. This section reviews the conditions of self-similarity as they apply to indentation, and presents the resulting scaling relations.[2]

Material Behavior

In order for the indentation problem to be self-similar, the indented material must satisfy a particular condition: the constitutive relations of the material should be homogenous with respect to the strains, $\boldsymbol{\varepsilon}$ (or stresses, $\boldsymbol{\sigma}(\boldsymbol{\varepsilon})$). In other words, the indented material can be described by Equation (2.1). Applied to materials operating in their elastic range (both linear and non-linear elastic range), this condition is satisfied as follows:

$$\mathbb{C}(\lambda\boldsymbol{\varepsilon}) = \lambda^{\kappa-1}\mathbb{C}(\boldsymbol{\varepsilon}) \tag{2.3}$$

where $\kappa = 1$ in the case of linear elasticity, and $\mathbb{C}(\boldsymbol{\varepsilon})$, the secant stiffness tensor, defines the stress tensor $\boldsymbol{\sigma} = \mathbb{C}(\boldsymbol{\varepsilon}) : \boldsymbol{\varepsilon}$. Note that the expression also applies to materials operating at the rigid plastic limit behavior; for such materials, the dissipation function $\boldsymbol{\sigma} : \mathbf{D} = \pi(\mathbf{D})$ defines

[2] The self-similarity discussion of this section is inspired by those of [19], [10], and [70].

the stress tensor: $\boldsymbol{\sigma} = \frac{\partial \pi}{\partial \mathbf{D}}(\mathbf{D})$ [25].

Note that Equation (2.3) does not apply to linear-elastic perfectly-plastic materials This is because there exists no unique κ which can apply for all the strains realized during an indentation in these materials: $\kappa = 1$ in the elastic range and $\kappa = 0$ at the limit of the elastic domain.

Probe Geometry

A variety of indenter tips, or probes, have been successfully employed for indentation: flat punch, Berkovich (Figure 2-5), Vickers (4-sided pyramidal probe with 68^o solid angle), sphere, or cone. The flat punch probe maintains a constant area of contact throughout indentation, but

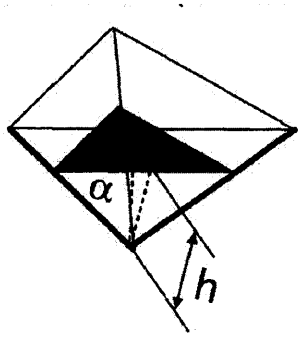

$$A = 3\sqrt{3}h^2 \tan^2 \alpha$$
$$A = 24.56h^2$$

Figure 2-5: The particular geometry of a Berkovich indenter, with solid angle 65.3^o. h denotes the depth of indentation, and the dark triangle denotes the projected area of contact, A. From [19].

is more commonly used in indentation theory than actual testing. The spherical probe realizes only the elastic range of the indented material for low-load indentations, and is challenging to manufacture. The advantage of the Berkovich probe arises from its sharp geometry; this probe accesses, and thus requires, a smaller volume of material when testing. Additionally, the particular geometry of the Berkovich probe can be more accurately manufactured. The Berkovich probe is thus popular in research. Nevertheless, even at low loads the Berkovich probe generates high stress concentrations directly beneath the probe, and thereby solicits the

material plastically.

For all probe types, the height z of the surface of the probe in the indented material thus must follow Equation (2.2). The expression assumes a Cartesian coordinate system $Ox_1x_2x_3$ with the origin at the tip of the probe (and x_3 into the depth of the probe). Axisymmetric probes with a radius r realize a further simplifcation of this expression:

$$z(r) = Br^d \tag{2.4}$$

where B is a proportionality factor representing the radius at unit radius, and d is the degree of the homegenous function (1 for both Berkovich and conical probes) of the probe geometry. The expression simplifies even further for the Berkovich probe:

$$z(r) = r \tan \theta_{eq} \tag{2.5}$$

where θ_{eq} is an "equivalent cone angle". A conical probe which subtends θ_{eq} gives the same projected contact area at a given depth as the Berkovich probe. Given the contact area expression of the Berkovich probe [53]:

$$A(h) = 24.56h^2 \tag{2.6}$$

and the contact area expression of a conical probe:

$$A(h) = \pi(h \tan \theta)^2 \tag{2.7}$$

equating the two contact area expressions reveals the θ_{eq} of the Berkovich probe:

$$\theta_{eq} = \tan^{-1}\left(\sqrt{\frac{24.56}{\pi}}\right) \approx 70.32^o \tag{2.8}$$

Self-Similar Scaling Relations

The previous sections applied the concept of self-similarity to the setup of the indentation problem; this section presents the resulting scaling relations. Self-similar processes such as indentation are defined by this ability to use scaling relations to determine certain properties

(load P, depth h, contact area A_c) at any point during the loading based on the properties for an initial indentation response (load P_0, depth h_0, contact area A_{c0}). The work of Borodich informs [11] the scaling relations for all probe types. The scaling relation from a consideration of load and depth is:

$$\frac{P}{P_0} = \left(\frac{h}{h_0}\right)^{\frac{2+\kappa(d-1)}{d}} \tag{2.9}$$

where d is the degree of the homogenous function describing the shape of the indenter (Figure 2-5); d approaches ∞ for flat-punch (cylindrical) indenters, 1 for pyramidal and conical indenters (also Berkovich), and 2 for spherical indenters [70]. A second important scaling relation relates depth and contact area:

$$\frac{h}{h_0} = \left(\frac{A_c}{A_{c0}}\right)^{\frac{d}{2}} \tag{2.10}$$

Indentation hardness (discussed further in Section 2.1.4) is here defined as the load for a given contact area, or average pressure beneath the probe:

$$H = \frac{P}{A_c} \tag{2.11}$$

Hardness is expressed by two quantities for which scaling relations were just presented; a combination of the scaling relations reveals a scaling relation for hardness::

$$\frac{H}{H_0} = \left(\frac{h}{h_0}\right)^{\frac{\kappa(d-1)}{d}} \tag{2.12}$$

Note that the hardness does not depend on the applied load throughout the loading process for rigid plastic behavior ($\kappa = 0$), or for conical or Berkovich probes ($d = 1$)

The scaling relations are futher simplified with a consideration of the contact radius of the probe, a (Figure 2-3). With a reminder that $A_c = \pi a^2$, the first scaling relation (Equation 2.10) reduces to:

$$\frac{a^d}{h} = \text{constant} \tag{2.13}$$

Axisymmetric probes realize a further simplification of the relation by incorporating Equation

(2.4):

$$\frac{h_c}{h} = \text{constant} \tag{2.14}$$

Note that the ratio of contact depth to indentation depth also does not depend on the applied load.

2.1.3 Indentation Modulus

Indentation modulus reveals material stress-strain behavior. The quantity provides a snapshot of the elasticity, and coincides for isotropic materials with the plane-stress modulus. Through the use of the Galin-Sneddon solution and a consideration of the assumptions of the solution, this section formally describes the essential links between indentation modulus, physical quantities measured during the indentation test, and fundamental material properties. These links are the foundations of a meaningul nanoindentation analysis.[3]

The Galin-Sneddon Solution

The Galin-Sneddon solution provides expressions for three components of indentation analysis [64]: the indentation load P as a function of indentation depth h, the displacement field u_z of the indented material, and the stress field σ_{zz} of the indented material.

The solution considers a conical probe, for which the depth z at any time during loading is some function of the contact radius ρ and contact radius at maximum depth (probe radius, a), or $z = f(\rho/a)$. Galin and Sneddon employ the theory of Hankel transformations (two-dimensional Fourier transforms which apply to circular symmetric functions) in the expression of the elastic equilibrium equations, and eventually the indentation depth h:

$$h = a \int_{\rho=0}^{\rho=a} \frac{f'(\rho)\partial\rho}{\sqrt{a^2 - \rho^2}} \tag{2.15}$$

[3]The indentation modulus discussion in this section is inspired by those of Bobko 2008, Vandamme 2008, and Constantinides 2006.

as well as the indentation load P:

$$P = 2\frac{E}{1-\nu^2}\int_{\rho=0}^{\rho=a}\frac{\rho^2 f'(\rho)\partial\rho}{\sqrt{a^2-\rho^2}} \tag{2.16}$$

In the case of the conical indentation, this load P and depth h, thus expressed, assist in the expression of the displacement field u_z of the indented material:

$$u_z(\rho,0) = \frac{2h}{\pi a}\left(a\sin^{-1}(a/\rho) - \rho + \sqrt{\rho^2-a^2}\right) \tag{2.17}$$

for $\rho > a$, and the stress field σ_{zz} of the indented material:

$$\sigma_{zz}(\rho,0) = -\frac{Eh}{2(1-\nu^2)\pi a}\cosh^{-1}(a/\rho) \tag{2.18}$$

for $\rho < a$ [64]. When applied to an axisymmetric cone of angle θ, the depth and load expressions reduce to:

$$h = \frac{\pi}{2}\frac{a}{\tan\theta} \tag{2.19}$$

$$P = \frac{2}{\pi}\frac{E\tan\theta}{1-\nu^2}h^2 = \frac{1}{2}\frac{E}{1-\nu^2}\frac{A_c}{\tan\theta} \tag{2.20}$$

Finally, a derivative of the load expression with respect to depth yields Bulychev-Alekhin-Shoroshorov (BASh) equation [15]:

$$S = \frac{dP}{dh} = \frac{2}{\sqrt{\pi}}M_0\sqrt{A_c} \tag{2.21}$$

where M_0, defined both as plane stress modulus and indentation modulus, links with the elastic properties (E,ν) of the indented material through the expression $M_0 = \frac{E}{1-\nu^2}$. Thus presented, the solution of Galin and Sneddon, in conjunction with the BASh equation, provides an important link between measurable indentation quantities P, h and the sought-after material property, intentation modulus M.

Galin-Sneddon Assumptions

The Galin-Sneddon solution rests on two assumptions: an assumption of small perturbations, i.e., small displacements and small deformation, and an assumption of a rigid probe. Regarding the first assumption, a correction γ may be applied to the stiffness to account for the radial displacement of the compressible indented material [32]:

$$S = \gamma \frac{2}{\sqrt{\pi}} M_0 \sqrt{A_c} \tag{2.22}$$

Regarding the second assumption, it may be noted that in practice, the probe deforms elastically. Even diamond probes exhibit a finite Young's Modulus ($E_i \simeq 1,141$ GPa) and Poisson's ratio ($\nu_i = 0.07$) [22]; ultimately, the elasticity of the probe corresponds to a displacement of both the probe and the indented material. This additional displacement affects measured indentation quantities. Thus, based on Hertz's contact solution [34], the indentation modulus M is corrected by a consideration of the elasticity of both the probe and the indented material in series [53]:

$$\frac{1}{M_0} = \frac{1-\nu^2}{E} + \frac{1-\nu_i^2}{E_i} \tag{2.23}$$

Dimensional Analysis

Dimensional analysis is of importance to the researcher and scientist because it allows the reduction of a complex problem with many variables into a system of a finite number of dimensionless quantities. The method, pioneered by Buckingham [14], is employed here as a means of better understanding indentation hardness.

Consider again the probe which indents a material (with cohesion c, poisson's ratio ν, and plane stress modulus M) to a depth h under applied load P. Initially, the two dependent variables of the problem, P and A_c, are expressed as functions of the remaining independent variables:

$$P = f(h, \theta, M_0, \nu, c, \mu) \tag{2.24}$$

$$A_c = f(h, \theta, M_0, \nu, c, \mu) \tag{2.25}$$

The application of Buckingham's Π-Theorem yields the relation between the dependent variables and independent variables as two dimensionless parameters:

$$\frac{P}{ch^2} = \Pi_{P,\text{ load}}\left(\theta, \frac{M_0}{c}, \nu, \mu\right) \tag{2.26}$$

$$\frac{A_c}{h^2} = \Pi_{A_C}\left(\theta, \frac{M_0}{c}, \nu, \mu\right) \tag{2.27}$$

The indentation modulus can also be considered with a dimensional analysis, with the inclusion of an additional quantity activated during unloading: $h_{\max}$, indentation depth. Another dimensionless parameter results from a reworking of Equation (2.26):

$$\frac{P}{M_0 h^2} = \Pi_{P,\text{ unload}}(\theta, \frac{c}{M_0}, \nu, \mu, \frac{h}{h_{\max}}) \tag{2.28}$$

The stiffness dimensionless parameter appears by recalling stiffness as defined in Equation (2.21), and subsequently deriving Equation (2.28) with respect to indentation depth h at $\frac{h}{h_{\max}} = 1$:

$$\frac{S}{M_0 h_{\max}} = \Pi_S(\theta, \frac{c}{M_0}, \nu, \mu) \tag{2.29}$$

Finally, a return to the BASH Equation (2.21) yields the indentation modulus dimensionless parameter:

$$\frac{S}{M_0\sqrt{A_c}} = \frac{2}{\sqrt{\pi}}\frac{M}{M_0} = \Pi_M(\theta, \frac{c}{M_0}, \nu, \mu) \tag{2.30}$$

With the assumption based on the work of Stillwell and Tabor [66] that initial unloading presents a virtually elastic material response, the dimensionless parameter may be further simplified:

$$\frac{S}{M_0\sqrt{A_c(\theta)}} = \text{ constant} \tag{2.31}$$

2.1.4 Indentation Hardness

Indentation hardness reveals information about material strength. This section opens with a return to dimensional analysis, and formally describes the essential links between indentation hardness, physical quantities measured during the indentation test, and fundamental material

properties. These links are the foundations of a meaningul nanoindentation analysis.[4]

Dimensional Analysis

Noting that hardness is defined as the ratio between the two independent variables ($H = \frac{P}{A_c}$, Equation (2.11)), a relation of the dimensionless parameters yields a third dimensionless relation, the ratio of hardness to cohesion:

$$\frac{\Pi_P}{\Pi_{A_c}} = \frac{H}{c} = \Pi_H \left(\theta, \mu, \nu, \frac{M_0}{c}\right) \tag{2.32}$$

Note that the hardness-cohesion ratio does not depend on the depth of indentation.

Link with Strength

The work of Tabor [67] first linked hardness with material strength; he noted experimentally that the average pressure sustained beneath an indentation at the onset of plastic yielding, H, tended towards 2.6 to 3 times the material yield strength Y, or $H/Y \simeq 3$. With the incorporation of the relation between material yield strength Y, and cohesion c as $Y = \sqrt{3}c$ for a Von Mises material ($\mu = 0$), the hardness-cohesion dimensionless relations transforms to a hardness-material strength relation, provided that $\frac{M}{c} \to \infty$:

$$\frac{H}{Y} = \frac{1}{\sqrt{3}}\Pi_H \simeq 3 \tag{2.33}$$

Thus expressed for the indentation problem in a Von Mises material, hardness fundamentally connects with material yield strength through dimensionless relations.

The hardness of cohesive-frictional materials links also with strength. Ganneau et al [27] applied yield design theorems to conical probe indentations with varying apex angles to develop cone-angle dependent hardness-cohesion solutions:

$$\frac{H}{c} = \Pi_c(\mu, \theta) \tag{2.34}$$

where μ is the friction coefficient of the indented material. Thus expressed for the indenta-

[4] The discussion of this section is inspired by that of [10] and [70].

tion problem in a cohesive-frictional material, hardness fundamentally connects with material strength. Indentation hardness links with the maximum stress sustained by the material before undergoing plastic deformation, and provides an idea of the material's strength behavior

Activated Volume of Indented Material

A question of interest to the researcher is the size d_s of the volume of material accessed by the indentation. This volume size may also be formulated as a dimensional analysis problem for the cohesive-frictional material in this investigation:

$$\frac{d_s}{h} = \Pi_{d_s}(\theta, \frac{M}{H}, \nu, \mu, \frac{h}{D}) \tag{2.35}$$

where D is the characteristic size of a particular phase of indented material (See 3.2.1 for more explanation of D). For indentations much smaller than the material characteristic size ($\frac{h}{D} \rightarrow 0$), this final material invariant drops out of the analysis; it remains that for the indented phase of size D, d_s is proportional to h [70]:

$$\frac{h}{D} \rightarrow 0 \implies d_s \propto h \tag{2.36}$$

Finally, a comparison of the simulated isocontours for Von Mises effective stress and effective plastic strain suggest that the d_s activated elastically by an indentation is greater than the d_s activated plastically (Figure 2-6; [44]).

2.1.5 Indentation in Heterogeneous Materials

Indentation test design is especially important when testing heterogeneous materials.[5] In order to approach the test analysis with the tools of continuum micromechanics, three scales of the indentation problem must not interfere with each other. The scale separability condition [20] describes the constituents and relationship of these three scales:

$$d << L << (h, a, D) \tag{2.37}$$

[5]The hardness discussion of this section is inspired by that of [70].

where d is the size of the largest heterogeneity of interest contained within the REV, L is the size of a representative elementary volume (REV), h is indentation depth, a is indentation radius, and D is a characteristic length scale of the material microstructure. The condition $L << (h, a)$ ensures that the mathematical relationships between indentation data and mechanical properties are valid, and the condition $d << L$ ensures that the REV contains enough heterogeneties to statistically represent the material. If the scale separability condition (Equation (2.37)) is satisfied, indentation to a depth h will reveal information about the material properties at the scale of the elementary volume L. In order to reveal information about material properties at the characteristic material scale D, an h/D ratio of $1/10$ should be satisfied as well [20].

2.1.6 Application of Nanoindentation to Brittle Materials

Nanoindentation of brittle materials is a developing area of research. To review a few representative applications, the technique has been used a means of characterizing the strength of heterogenous brittle materials, and the spatial distribution of their strength [18][76][23]. One interesting study has linked nanoindentation hardness with Mohs' hardness; the Mohs number has a logarithmic relationship with microhardness values, but this relationship disappears at small loads [35] [13]. The disappearance of this relationship could potentially be due to the different mechanisms that govern Mohs' hardness and nanoindentation hardness; Mohs' hardness is a scratch-type test that relates with both shear and strength properties of the material, whereas indentation hardness is a compressive test that links mostly with strength.

Recent nanoindentation of other brittle materials such as cement and shale has established techniques to assess the characteristic nanomechanical nature of these materials. Of importance to the current investigation, these studies have laid a foundation for the steps of the sample preparation of brittle materials, as well as assessment of nanoindentation results [50][10]. The current investigation extends this work to the process zone of marble as discussed in the next section.

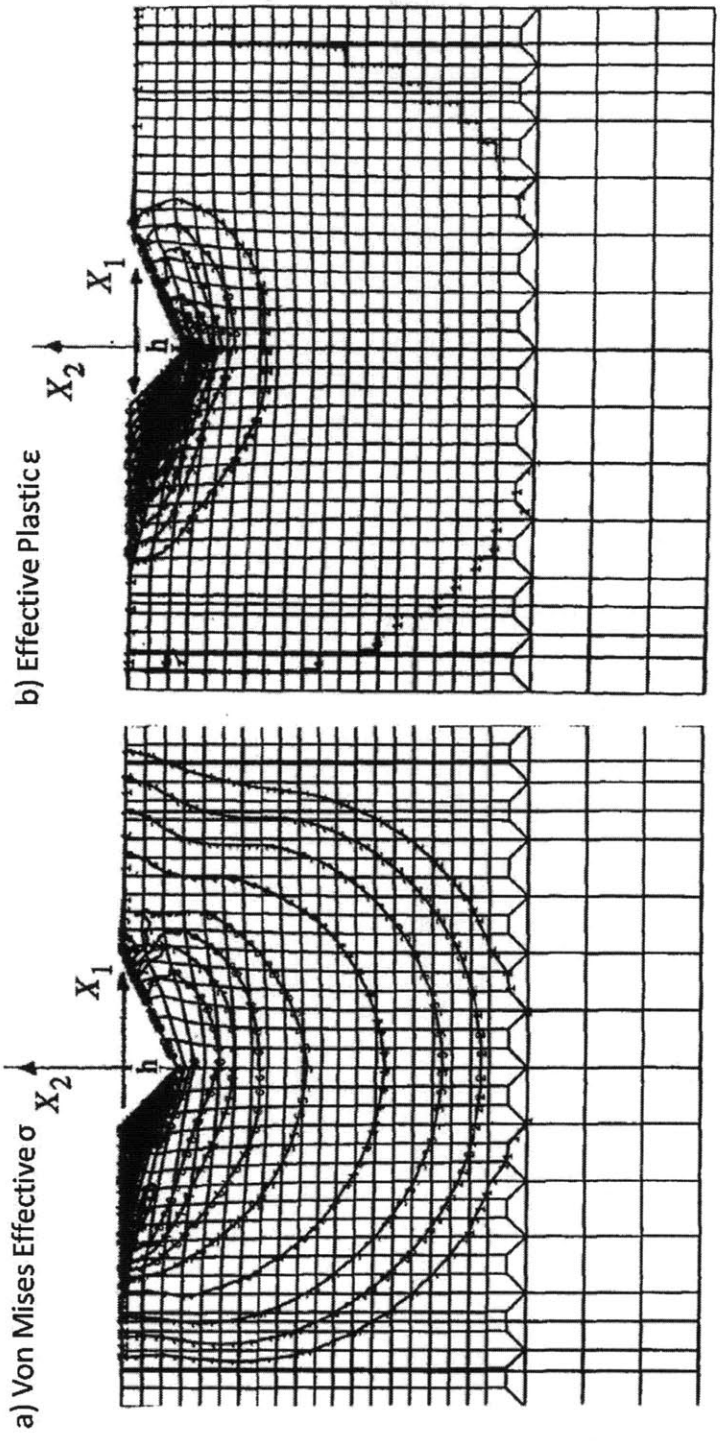

Figure 2-6: A comparison of the simulated isocontours for a) Von Mises effective stress and b) effective plastic strain suggest that the size d_s of the volume activated elastically by an indentation is greater than the d_s activated plastically. From [44].

2.2 Process Zone

This section presents the current understanding of, and the need for further study of, the second cornerstone: the process zone. A discussion of the process zone must begin with the process which generates the process zone: fracture. The section closes with a review of various size measurement techniques of the process zone; the results of these techniques reveal potential for the nanoindentation methods employed in the current investigation.

2.2.1 Fracture Mechanics of Rocks

Well-established theory has defined the stress distribution around a crack [36] [46], and the critical length at which a pre-existing crack propagates under constant stress in an isotropic, elastic solid. This theory was later extended to equilibrium cracking in a brittle material. The result of various important investigations [30][37][38][5] is the classic Linear Elastic Fracture Mechanics (LEFM) expression for the stress distribution σ_{ij} in the vicinity of the crack tip:

$$\sigma_{ij} = \frac{K_J}{\sqrt{2\pi r}} f(\theta) + \ldots \tag{2.38}$$

where θ describes the position around the crack, K_J is the stress intensity factor by which the remote stress is magnified (subscript J refers to the mode of crack opening; $J = I$ for the classic Mode I crack), and r is the radial distance from the boundary of the crack [38][69]. The physical quantities of importance are defined in Figure 2-7. According to Irwin's criterion, the crack will extend when K_J meets the material fracture toughness K_I, an intrinsic material property [69]. Rice investigated the crack tip from a theoretical perspective to ultimately configure the J-Integral, which expresses the energy release rate [59]. The integral does not consider plastic deformation and considers homogenous material properties in the vicinity of the crack tip.

Cracking of brittle material has been experimentally pursued at the macroscale extensively and in a variety of materials [31][54][72][62]. A recent study of the cracking of various brittle materials (marble, gypsum, granite) classified a finite number of crack geometries, defined their coalescence (the way cracks grow and interact with each other), and numerically modeled their macroscale cracking behavior [58][8]. However, the numerical model requires the size of the

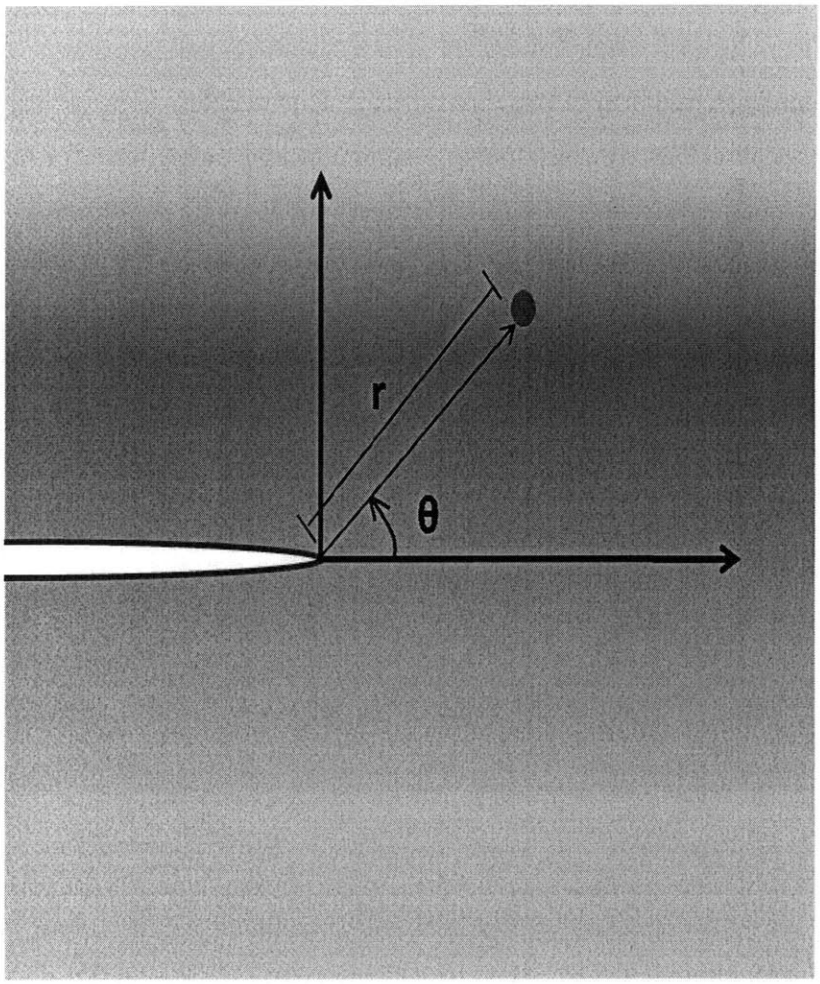

Figure 2-7: The physical quantities of importance when determining the stress distribution around a crack tip. Stress is greatest for small values of r and theta (i.e., close to the crack boundary).

process zone as an input [9]. Although as discussed in the next section, the process zone has been somewhat pursued experimentally, the micro/nanoscale information provided by the current study will further illuminate and support this macroscale work by providing that critical input: the strength and size information on the process zone.

2.2.2 Process Zone

The crucial area around the tip of a crack is termed differently in different fields, but the definitions converge on the same concept: a region of inelastically deformed material. This section presents the fundamental models of process zone material, as well as the interesting extension of these models to the large scale

Fundamental Theory

In metals, the region around the crack tip which undergoes a plastic deformation is termed the plastic zone [68]. An estimate of the size of the plastic zone r_p is provided by considering the local material yield stress σ_{ys} for the stress distribution in the vicinity of a crack tip σ_{ij} [69]:

$$r_p = \frac{1}{2\pi}\left(\frac{K_J}{\sigma_{ys}}\right)^2 f(\theta) \tag{2.39}$$

where K_J is the stress intensity factor. At fracture, the plastic zone corresponds to:

$$r_p = \frac{1}{2\pi}\left(\frac{K_{Ic}}{\sigma_{ys}}\right)^2 \tag{2.40}$$

where K_{Ic} is the material fracture toughness. Carrara marble exhibits a typical fracture toughness of $K_{Ic} = 0.65$ to $1.25\,\mathrm{MPa}\sqrt{\mathrm{m}}$ [3][2] and a tensile strength of $\sigma_{ys} = 3.32$ to $5.86\,\mathrm{MPa}$ [17][75]; these material properties yield an estimated LEFM process zone size of $r_p = 0.19$ to $2.3\,\mathrm{cm}$ for a Mode I crack in Carrara marble, [1][39]. Note that this extent varies based on the yield criterion used to determine the maximum stress [68].

In LEFM, the process zone is also termed the core region of plastic-behaving material. Nevertheless, a single core region criterion which applies to various loading conditions and is experimentally validated in rocks is lacking [42].

Theory Extension to Fault Scale

Study of the process zone at large scales reveals the potential for driving mechanisms best understood with investigation at a more fundamental scale: the micro- and nanoscales. The Dugdale model is a popular fault-scale process zone model. The model develops an expression for the size of the plastic zone s, or "inelastic zone," given an initial slit of length l, but with a consideration of the yield stress of the material and the remote tensile loading σ_t, rather than the fracture toughness K_{Jc} [26]:

$$2sin^2\left(\frac{\pi\sigma_t}{4\sigma_{ys}}\right) = \frac{s}{s+l} \tag{2.41}$$

As displayed in Figure 2-8, the model assumes an internally-loaded crack with length at most 1/5 of the sheet width in an infinite sheet of some thickness [26]. An application of the Dugdale model to faults reveals the stress-state of this region. The zone is larger for low-yield strength materials, and small or infinitessimal in high yield-strength materials. Most notably, as noted by Cowie and Scholz [21] for large-scale cracks or faults, friction is activated in the inelastic zone to lead to the term Frictional Breakdown Zone (FBZ). The zone begins at a distance $\frac{l}{2} - s$ from the center of the fault (Figure 2-9). For example, when the Dugdale model is applied to a Mode III fault, the stress within the FBZ is a reduced tip stress σ_{tip}:

$$\sigma_{tip} = \sigma_0 - \sigma_f \tag{2.42}$$

where σ_0 is the shear strength of the rock, and σ_f is the frictional stress on the fault. The tip stress and the remote stress are constant with time, which makes sense if friction is a scale-independent phenomenon. This model yields several fault properties confirmed by a comparison with data from actual faults: the most displacement occurs at the center of the fault, there is a constant relationship between the center displacement and the length of the fault, the fault may be only discontinuously open within the FBZ, and various deformation mechanisms may occur along the fault (Figures 2-10, 2-11 [21]). Figure 2-10 shows that longer faults tend to displace more. Figure 2-11 shows that even at large scales, and even in faults that traverse several different material types ((c) in Figure 2-11), the greatest displacement occurs at the

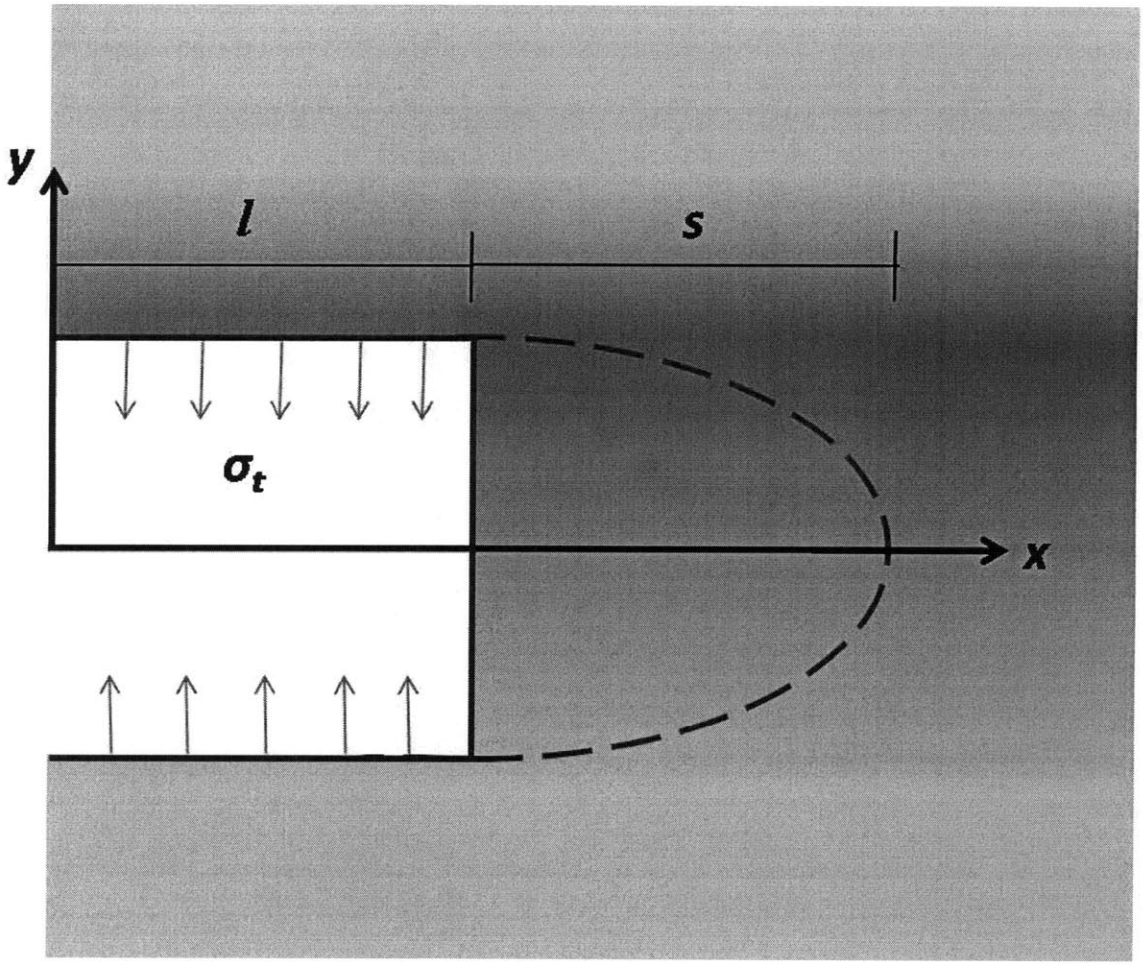

Figure 2-8: The physical quantities of importance for the Dugdale model. Adapted from [26].

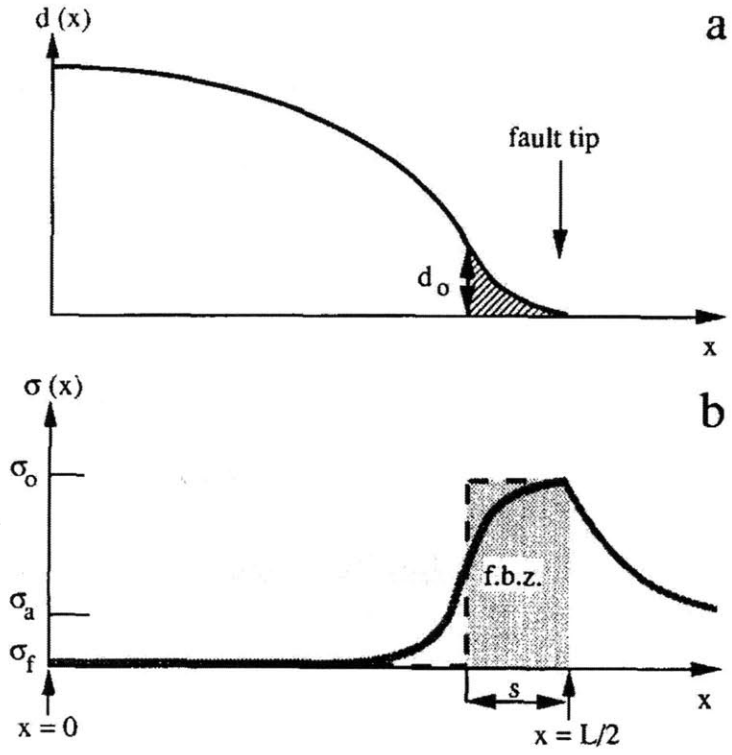

Figure 2-9: The Cowie and Scholz model reveals a frictional breakdown zone (f.b.z.) where intact friction is activated and the stress is the shear strength of the rock minus the frictional strength of the rock. From [21].

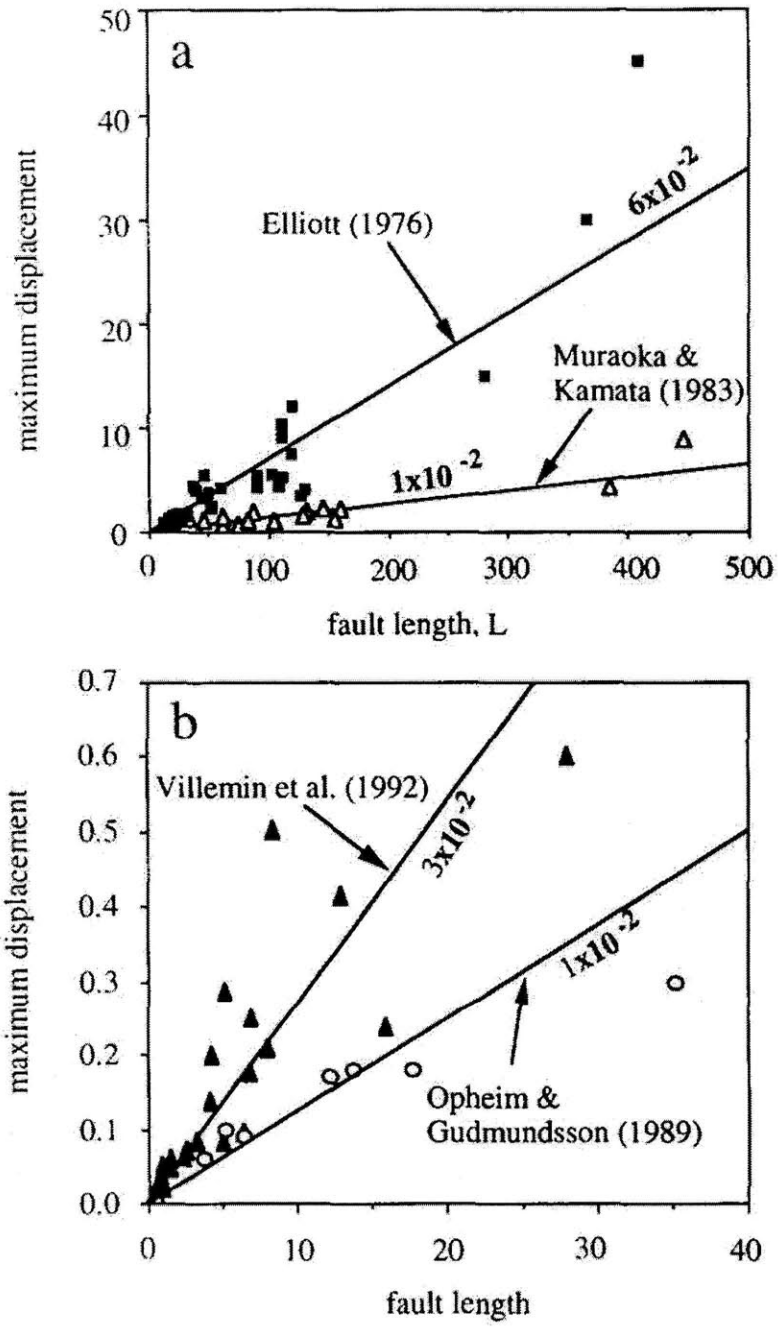

Figure 2-10: Faults at both (a) large and (b) small scales indicate a positive correlation between fault length and maximum displacement. All lengths are in hundreds of meters. From [21].

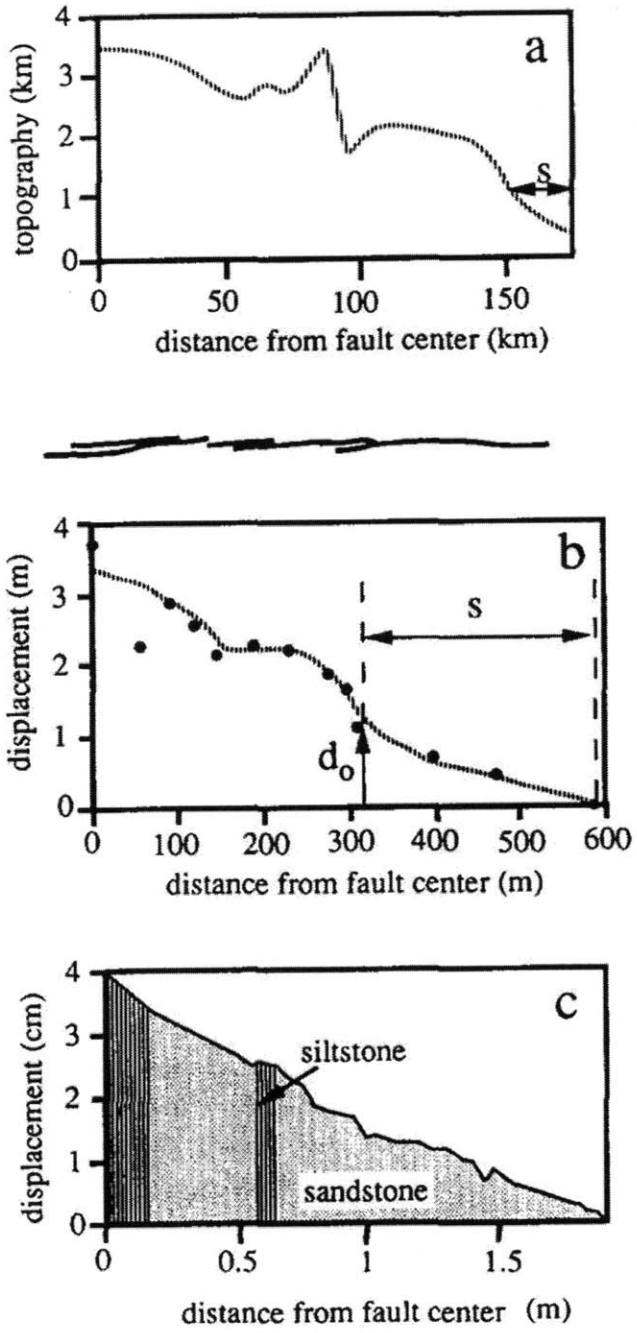

Figure 2-11: Faults at both (a) large and (b), (c) small scales indicate that the most displacement occurs at the center of the fault. (a) profile of the footwall block of the Wasatch fault in Utah; (b) displacement profile along normal fault in British coalfields; (c) displacment profile along normal fault in Japan. From [21].

center of the fault; displacement significantly decreases at the fault boundaries; the figure even indicates an estimation of plastic zone size based on the Dugdale model (Equation 2.41) [21]. Furthermore, the presence of deformation micromechanisms (microveins, fractures, deformation lamellae, pressure solution structures, etc.) even for large scale fault decreases at a logarithmic rate with distance from the fault. Microfractures also tend to form small angles with the fault plane [71].

Thus, the Dugdale model has been applied even at the fault scale (several kilometers), and as illustrated in Figures 2-10 and 2-11 shows similarities at several levels of this scale. These similarities suggest that mechanisms at a more fundamental scale – the micro- and nanoscales – ultimately determine cracking behavior.

Desipte this potentiality, the Dugdale model does not consider the variability of properties in the region [26]. However, application of the closely related Cowie and Scholz model to existing faults reveals a logarithmically decreasing microfracture density within and moving away from the "cohesion zone," (a low-strength area surrounding a displaced fault), and a finite scale-independent limiting microfracture density [71]. The Cowie and Scholz model also considers a Frictional Breakdown Zone, a region within the cohesion zone, at the very tip of the fault, where intact friction is activated and the stress is the shear strength of the rock minus the frictional strength of the rock [21]. The documentation in the Vermilye-Scholz study of small scale fractures within the cohesion zone suggests the potential for the as yet unexplored nanomechanical property change within the cohesion. The current investigation explores nanomechanical property change within the process zones predicted by classic LEFM, Dugdale, and Cowie-Scholz models, including the frictional breakdown zone of the Cowie-Scholz model (Table 2.1).

Process Zone Size Measurement

Many theories exist regarding the process zone (See Table 2.1), but the experimental investigation of this theoretical region in rocks is a relatively recent development. Historically, metallic materials have been a popular domain for crack studies because of the ease with which specimens are obtained and created, and the direct industrial applications. Investigations into the plastic zone have assumed different forms in different material types. In metals, various meth-

Model	Outputs	Inputs
LEFM [69]	Size of plastic zone	Material fracture toughness (K_{Ic}), material strength (in tension, σ_{ys})
Dugdale [26]	Size of plastic zone	Material strength (in tension, σ_{ys}); Tensile loading σ_t; Size of initial crack l
Cowie/Scholz [21]	Size of plastic zone; Frictional breakdown zone (FBZ)	Same as Dugdale

Table 2.1: Existing process zone models.

ods of microscopy have been most successful in defining the limits and shape of the plastic zone. However, most similar to the technique employed in the current investigation, a fluctuation in the microhardness values reveals the plastic boundary in steel [68]. As illustrated in Figure 2-12, microhardness traverses were run in various directions with respect to the tip of a stopped fatigue crack. The fluctuation in the microhardness values, in conjunction with interpolation, allowed for the sketching of the plastic zone [61]. Similarly, in single crystal copper a region of high microhardness develops within the plastic zone defined by fracture mechanics (Figure 2-13). The hardness was measured with a microhardness tester with a Vickers head and 15g load. Both statically and dynamically tested samples exhibited this trait, but samples with longer pre-existing cracks exhibited a higher hardness in this zone. Transmission Electron Microscopy (TEM) revealed that the mechanism responsible for the high measured microhardness was a higher density of dislocations ("dislocation cells", or thick-walled openings in the boundaries between grains of copper) [56]. A link of microstructure with nanomechanical properties in the brittle geomaterial of the current study will explore whether the same mechanisms are potentially at play for cracking in a brittle geomaterial as for copper.

Several studies have undertaken experimental investigation of the process zone in rock, but do not link with nanomechanical properties. A recent study at MIT of the process zone in marble presented microscale information of a unique process zone phenomenon in marble [73]. The study linked crack coalescence in gypsum and marble specimens with various pre-existing crack ("flaw") geometries. In this study, it was noted that marble physically brightens, or displays

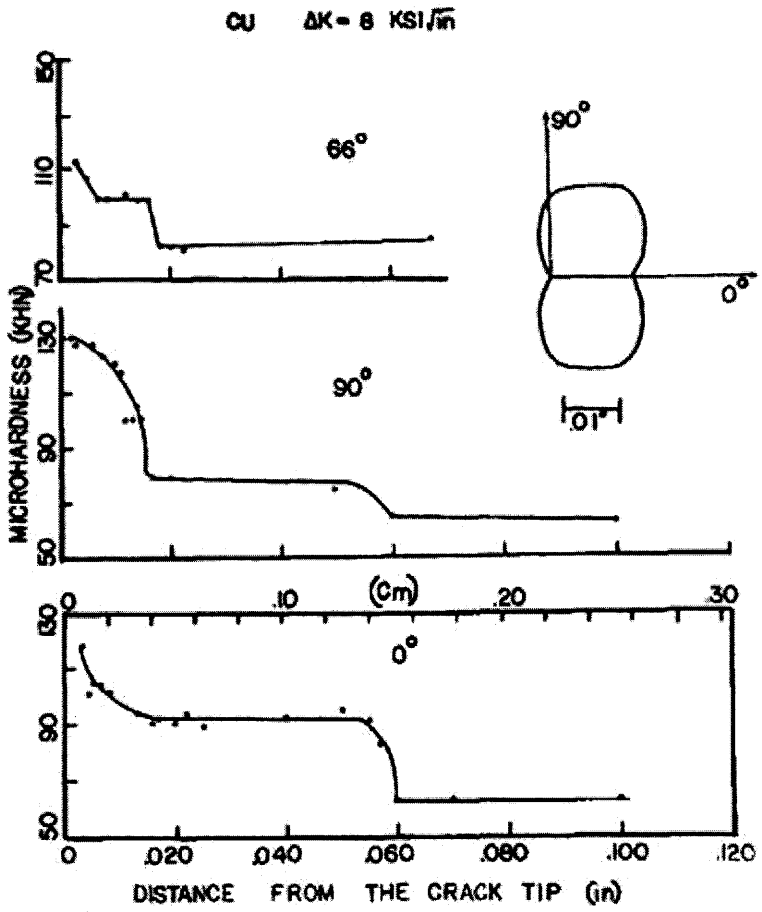

Figure 2-12: Microhardness traverses run in three directions ((a) 66°, (b) 90°, and (c) 0°) with respect to the crack tip revealed a fluctuation in hardness at a distance from the crack tip. From [Saxena 1975].

"white patching" at the tips of flaws prior to crack coalescence. As determined by scanning electron microscopy, the white patches result from the growth and extension of networks of microcracks, which manifest in one of four qualitative densities: Background (natural density of microcracks in the intact rock), Low, Medium, and High Crack Density [73]. The study thus investigated the scale and structure of this process zone phenomenon at the microscale. The next step, which is addressed by the current study, is to investigate the accompanying nanomechanical properties.

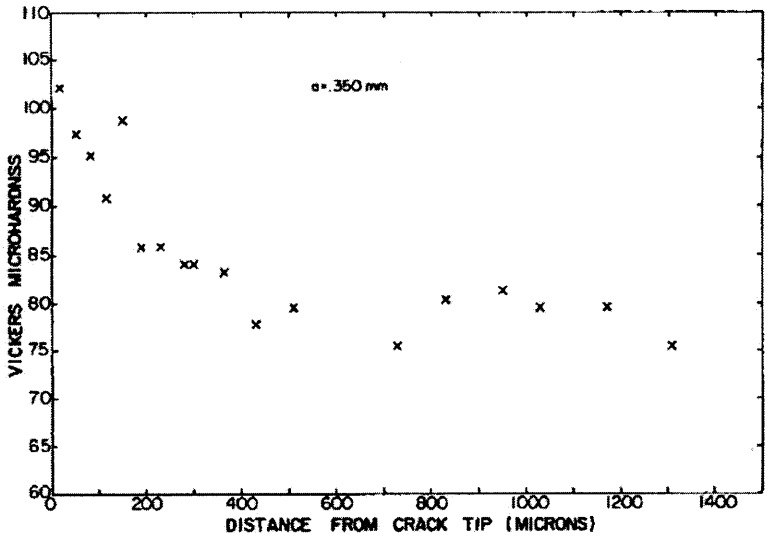

Figure 2-13: Single-crystal copper having undergone cyclic fatigue loading shows high hardness near the crack tip. From [Purcell 1974].

Synthesis with Current Investigation

Existing studies of the process zone have revealed important information for the current investigation. LEFM provides a theoretical estimate of process zone size based on material properties and loading conditions (Equations (2.39) and (2.41)). Experimental evidence reveals the potential for a fundamental scale-independent cracking mechanism ([21]) , as well as a change in the process zone in either structure, mechanical properties, or both at small scales in various materials ([56], [73], [61], [68]). The current investigation synthesizes evidence from these various studies into an exploration of similar trends in a brittle geomaterial.

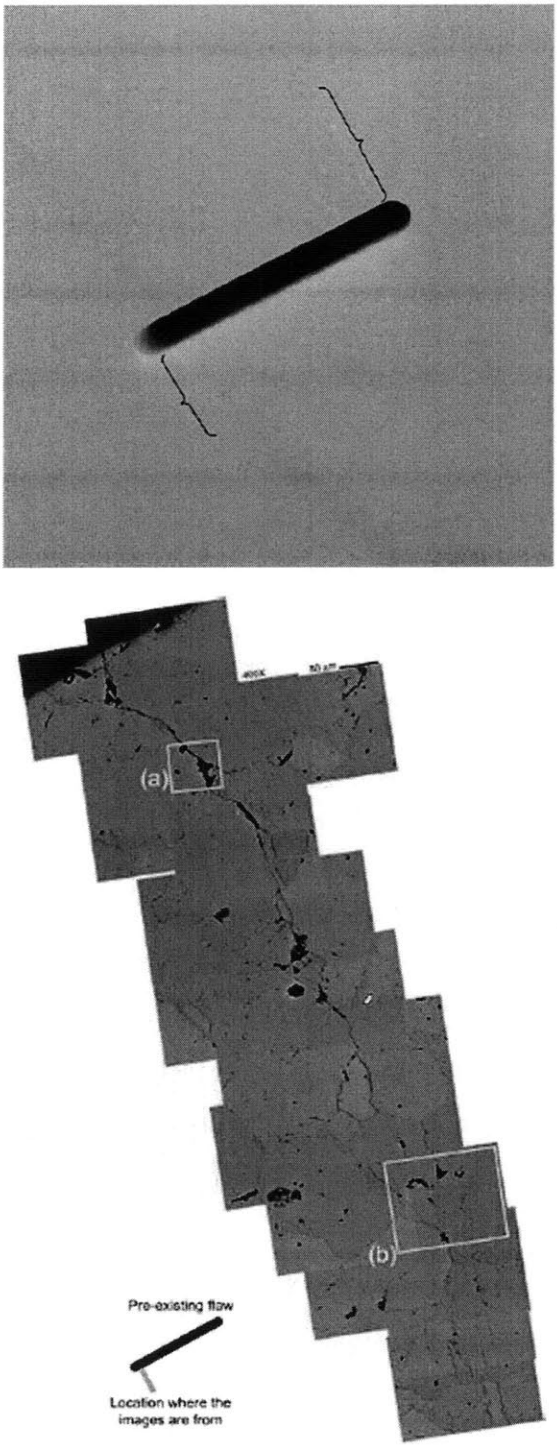

Figure 2-14: (Top) White patching, indicated by the brackets, is visible at the tips of the flaw after loading. (Bottom) Assemblage of SEM images of microcracking and spalling, (a) and (b), from the bottom left corner of the flaw shown at top. The current study investigates mechanical properties at the scale of the bottom image.

2.3 Scanning Electron Microscopy (SEM) and Environmental Scanning Electron Microscopy (ESEM)

Electron microscopy is an ideal technique for obtaining the third element of the current investigation: structural information at fundamental material scales. Many studies have established SEM as an effective means of investigating process zone microstructures. Its ability to sense changes in topography makes the SEM ideally suited for observation of microcracks, spalling, and other process zone microstructures. This section presents the technique, its function, and application.

2.3.1 Operation of the SEM

There are three basic parts to the operation of the SEM: the electron gun, the lenses, and the evacuated tube (Figure 2-16). The evacuated tube houses all the elements. The electron gun emits an electron beam, and the lenses demagnify and redirect this beam to ultimately focus the beam onto the specimen as a spot with a size of 10 nm (100 Å). The beam is composed of electrons which have been accelerated to a high energy (0.1 - 30 kV) at the gun. The beam interacts with the topmost 1 μm of the specimen ("Electron Range" in Figure 2-15, from [29]). The image is ultimately formed from the detection of electrons that are reflected or re-emitted from the specimen. A scintillator/photomultiplier will amplify the image for display on a cathode-ray tube. Older SEMs, such as the SEM used in work by Wong [73] and displayed in Figure 2-14, also include a slow-scan option for the recording of images onto photography film, and a videoprinter for instant printing of images [28].

The full image is developed by scanning the beam over the specimen surface in a line-by-line fashion, also known as "rastering." Rastering occurs due to a mechanism within the evacuated tube: a pair of coils near the electron gun deflects the beam away from the optical axis of the microscope, and then a second lower pair of coils bends the beam back onto the optical axis. Magnification of a scanned image is achieved by rastering a smaller area of specimen, which is done by deflecting the beam less. Magnification, M, is defined as

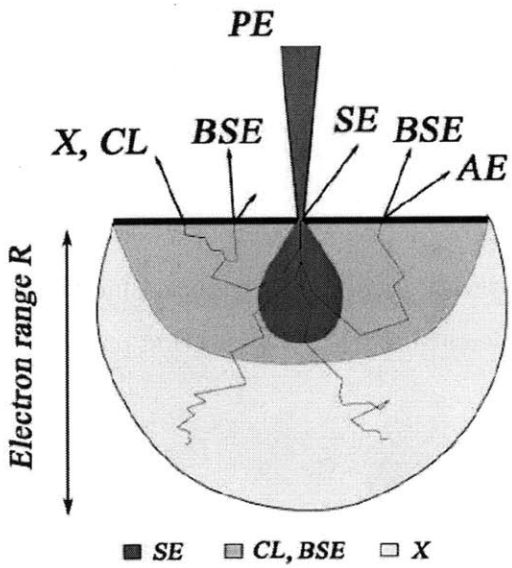

Figure 2-15: The various signals detected in SEM. PE indicates "primary electrons", i.e. the electron beam. BSE (backscattered electrons) and SE (secondary electrons) are the signals used in the current study. X (X-ray), CL (cathodoluminescence), and AE (Auger electrons) are not used. From [29].

$$M = \frac{\text{length of raster on viewing screen}}{\text{length of raster on specimen}} \tag{2.43}$$

When the signal from one point differs from the signal at another point (due to differences in material, or distance traveled by the electron because of changes in topography), the difference manifests as contrast, or a change of intensity, in the image [28].

SEM has been used to monitor microcracks in granite with a typical opening of 0.5 μm and length of 20-30 μm [12]. The visibility of features smaller than this microcrack size such as thin bridges between cracks, as well as scalloping and tiny crystallites at the edges of pores in the rock, suggest that the surface preparation for SEM does not introduce significant damage to the microstructure [12]. Because brittle materials that have undergone stressing to induce a process zone have even more such structures visible, it has been suggested that the

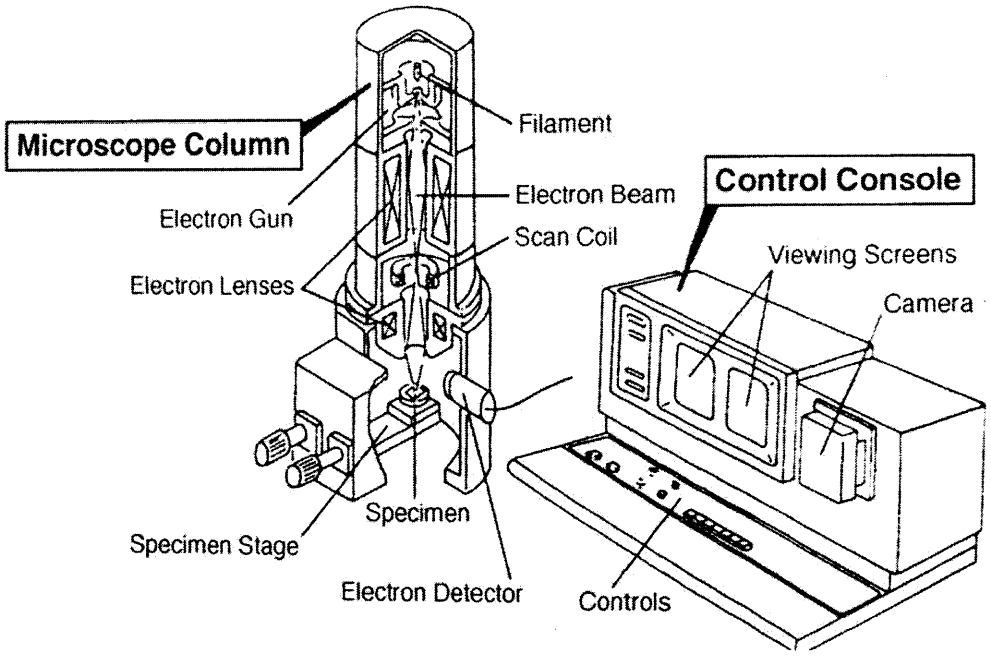

Figure 2-16: The components and layout of the standard Scanning Electron Microscope [20].

surface preparation for SEM is even less significant when observing process zone or microcracked materials. However, if used as a final polishing stage, ion thinning may heat the specimen, introduce dimples with diameters ranging from 5 to 50 μm, and some debris may get trapped by larger cavities [65]. These consequences may damage the specimen and compromise any image obtained. ESEM, discussed in the next section, is thus an ideal alternative for the assessment of microstructure.

Despite the advantages of SEM, many samples are damaged if placed in a vacuum, and are not conductive to the electron beam. The advent of Environmental SEM (ESEM) and Variable Pressure SEM (VPSEM) had made microscopic imaging of these samples possible, and now over half of the SEM market is devoted to ESEM and VPSEM [28].

2.3.2 Operation of the ESEM

The ESEM operates at pressures ranging from 10 to 2700 Pa, and with higher energy electron beams (10-30 keV, as opposed to 1 - 5 keV for standard SEM). The machinery for ESEM is

the same as for standard SEM, with the addition of a few components::

- High Vacuum Pump. This runs parallel to the evacuated tube containing the electron gun and lenses, and connects to the column in several places.
- Pressure Limiting Aperture (PLA). The PLA is an aperture with a diameter of a few hundred microns. It resides at the base of the evacuated tube, and its tiny diameter allows the chamber pressure to be 100 to 1000 times that of the pressure in the tube, or even higher if two PLA's are connected in series.
- Gas. The gas in the chamber is typically water mist. Rather than operating in vacuum conditions as in a standard SEM, operating the chamber with a water mist at the saturated vapor pressure of water, 2700 Pa, stabilizes any water present in the sample.

The presence of gas in the ESEM has competing effects. In one respect, gas serves as the limiting feature of the ESEM; electrons from the beam may collide with the gas which affects the ESEM image by reducing image contrast due to beam broadening, or a skirt appearing about a beam in the image. High beam energy and low gas pressure combat beam broadening. Additionally, mounting the PLA even closer to the specimen reduces the Gas Path Length (GPL). Helium, due to its low atomic number, also prevents beam broadening, but it easily ionizes so may allow for sample charging [28].

However, the intent of placing gas in the chamber is to assist the imaging process. If the energy of the beam is four times the ionization energy of the bound outer electron of the gas particles, electrons will ionize the gas as they pass through. The ionized gas particles then adhere to the specimen surface (negative ions to positive regions of the specimen, and positive ions to negative) to prevent a buildup of charge on the specimen. However, this advantage of having gas in the chamber is very unlikely to occur when the beam energy is much less or much greater than four times the ionization energy of the bound outer electron [28].

2.3.3 Imaging Modes

Because the electron beam actually interacts with the topmost micron (depending on imaging mode, discussed below) of the specimen, the image reflects not only surface features but also

subsurface features such as inclusions, voids, and porosity. This accessbility of the subsurface results in a lower image resolution than the resolution defined by the beam parameters. The volume of specimen with which the beam interacts is the "interaction volume." [28].

Electrons interact with the volume in various ways to result in the different imaging modes. Both the Backscattered and Secondary Electron imaging modes were used in this study (Chapter 4: Environmental Scanning Electron Microscopy (ESEM)). Once the electrons enter the specimen, the positive charges in the nuclei of the specimen atoms attract the electron and redirect their otherwise straight trajectories. This occurrence is called "elastic scattering". Specimens with a high atomic number induce more elastic scattering events. Once so much elastic scattering has occurred that the electron is deflected back out of the specimen, the electron is referred to as a "backscattered electron." Additionally, the electron may transfer a lot of energy while traveling within the specimen; these electrons are detected as "secondary electrons", or electrons with less than 50 eV of energy. Backscattered electrons are particularly well suited for the relatively high morphology of process zone areas imaged in this study because they must travel deep within the specimen compared to secondary electrons (Figure 2-15).

2.4 Definition of Terms

The definition of the following terms varies in the literature; they are here defined for the scope of this study. The main difference between the terms is the material to which they each apply; whereas "Process Zone" is used generally, "White Patching" applies to marble in particular.

Process Zone: In various types of brittle materials, the process zone is a zone of inelastic deformation at the tip of a propagating crack. The type of loading determines the nature of deformation. For example, for Mode III (in-plane/out-of-plane) cracks, the plastic zone deformation is arrays of tensile cracks [21]. For this study, the white patching near the flaw tip is a process zone region. White patching contains established process zone microstructural features [73], but the nanomechanical properties of the region will provide new information on the process zone.

White Patching: In marble specifically, white patching is a zone of inelastic deformation at the tip of a propagating crack. The abundance of microcracks, spalling, and other microfeatures

grant the region a white appearance.

2.5 Chapter Summary

This chapter has reviewed the three key elements of the current investigation: nanoindentation, the process zone, and ESEM. Basic principles and equations for each element were presented, and thus a solid foundation was laid to understand how the elements can work together to reveal the answers to the fundamental research question of the precise mechanism at play in the process zone. As displayed in Table 2.2, this study presents the first occasion to bring the elements of nanomechanical properties, the process zone, and microstructure together in such a way for a brittle geomaterial. The contributions of Barenblatt, Irwin, and others [5][38] established fundamental process zone theory (Section 2.2.2), but an extension to the nanomechanical properties of indentation modulus and hardness was yet to be made. Uguz and others [68] explored process zone size, and in some cases process zone size as a function of indentation hardness (Section 2.2.2), but an extension to a brittle geomaterial is yet to be made. The studies by Bobko, Vandamme, Constantinides, and others [10] have established a means of investigating the nanomechanical properties of brittle geomaterials with nanoindentation (Section 2.1); an extension of this work to the particular brittle geomaterial process zone documented by Wong [73] remains. The next chapter presents the precise application of all key elements in this investigation.

	Barenblatt 1959 [5], Irwin 1957 [38]	**Uguz 1996** [68]	**Bobko 2008** [10]	**Wong 2008** [73]	**Current Study**
Geomaterial	Y	Y	N	Y	Y
Process Zone	Y	N	Y	Y	Y
Microstructure	N	Y	Y	Y	Y
Nanomechanical Properties	N	Y/N	Y	N	Y

Table 2.2: Although the topics of geomaterials, process zone, microstructure, and nanomechanical properties have been pursued individually in the literature, this study presents the first occasion to bring all four elements together in such a way.

Chapter 3

Material and Methods

3.1 Material

This study focuses on Carrara marble because of its homogeneous microstructure and unique crack tip process zone (See Section 2.2 for a general discussion of the process zone). Marble physically brightens, or displays "white patching" at the tips of existing cracks prior to the growth of new cracks. Some white patching occurs within the process zone, or the theoretical region of plastic deformation directly around the tip of an existing crack, as defined by classical Fracture Mechanics (Table 2.1; [5][41][56][68][71][26]). Some white patching occurs outside of the theoretical process zone, further from the tip of the existing crack. These white patches result from the growth and extension of networks of microcracks through grain boundaries, the microscale heterogeneties of marble [73].

This study investigates the nanomechanical properties of the white patching in marble. The study rests on the hypothesis that this white patching may be considered a process zone because it contains microstructural process zone features (i.e., microcracks, and spalling), and because of the trends found in nanomechanical properties. The investigation aims to shed light on the nanomechanical properties of this type of near-crack-tip process zone.

Marble is a metamorphic rock. Metamorphic rocks form under extreme subterranean pressure and/or temperature conditions, which can drive moisture, oxygen, and carbon dioxide out of existing rocks. Marble typically forms from limestone or dolomite, both single-mineral sedimentary rocks. The varied colors of different types of marble are attributed to the parent rock

Property	Value
Material	Carrara Marble
Constituents	Calcium Carbonate ($CaCO_3$), Organic Foliation [51]
Young's Modulus, E	49 GPa [73]
Poisson's ratio, ν	0.19 [73]
Porosity	0.33 - 0.48% [1]
Flexural Strength	13 MPa [48]
Tensile Strength, σ_{yt}	3.32 to 5.86 MPa [17][75]
Fracture Toughness, K_{Ic}	0.65 to 1.25 MPa$\sqrt{\text{m}}$ [3][2]

Table 3.1: Typical properties of Carrara marble.

from which they form. Marble is relatively soluble and supports vegetation, properties which can complicate the quarrying, or marble extraction, process, and is thus often more vulnerable to chemical rather than mechanical weathering processes [55].

Carrara Marble originates from the marble quarries near the town of Carrara, in the north-western part of the Alpi Apuane metamorphic complex in Italy (See the circle indicated in Figure 3-1). Typical material properties are displayed in Table 3.1. The constituents of this type of marble are tightly packed grains of calcium carbonate crystals. The grain sizes range from 40-200 μm, and the rock mass is often interspersed with dark ribbons of mineralogical and organic foliation. Despite the relative purity of the marble, other minerals such as quartz, albite, white mica, and opaque minerals may be present. Nevertheless, the microstructure of the rock contributes to its historic popularity as an artistic and structural material. Carrara marble has a homogenous fabric and is composed almost entirely of pure calcite. No preferred grain shape or crystallographic orientation has been identified, contributing further to the homogeneity of the rock [51].

The three chief microfabrics of Carrara marble provide insight into the two geologic events that were involved in its creation. Type A microfabric, the type used in this investigation, is located in the normal limb of a northeast-facing isoclinal fold. The precise location of the marble used in this study is displayed in Figure 3-2. The typical grain size of this microfabric is large, 300 μm (D in the scale separability condition, Equation (2.37)), and the grain shape is equant polygonal with straight or slightly curved boundaries. There is an increase in the grain size from east (80 – 100 μm) to west (250 – 300 μm). The location of the microfabric, the isoclinals fold, characterizes the first geologic event: nappe emplacement to develop isoclinal folds. Type

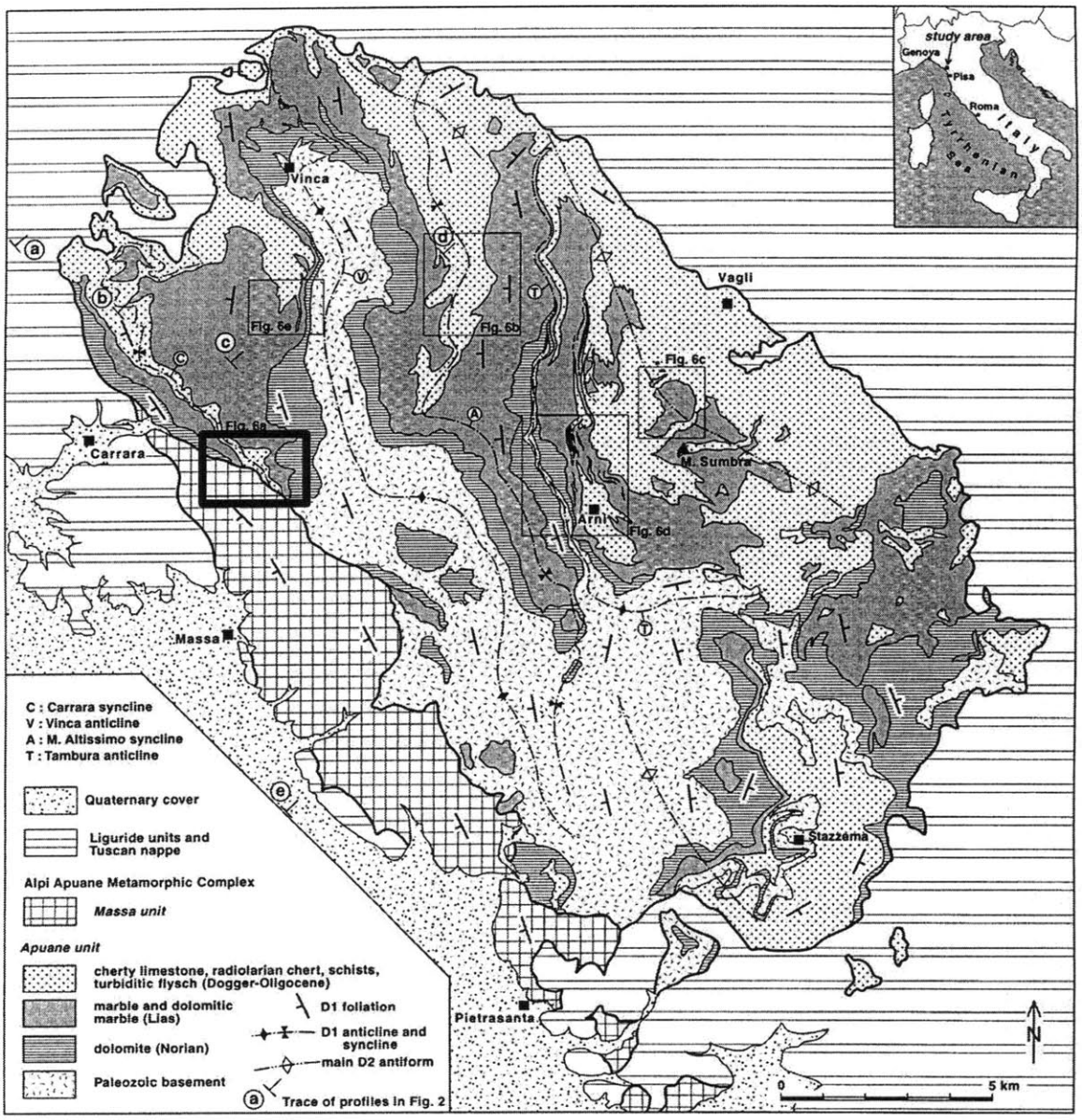

Figure 3-1: The Alpi Apuane marble complex in northern Italy. The town of Carrara is circled on the left. Detail of the boxed inset is shown in Figure 3-2 [Molli 2000].

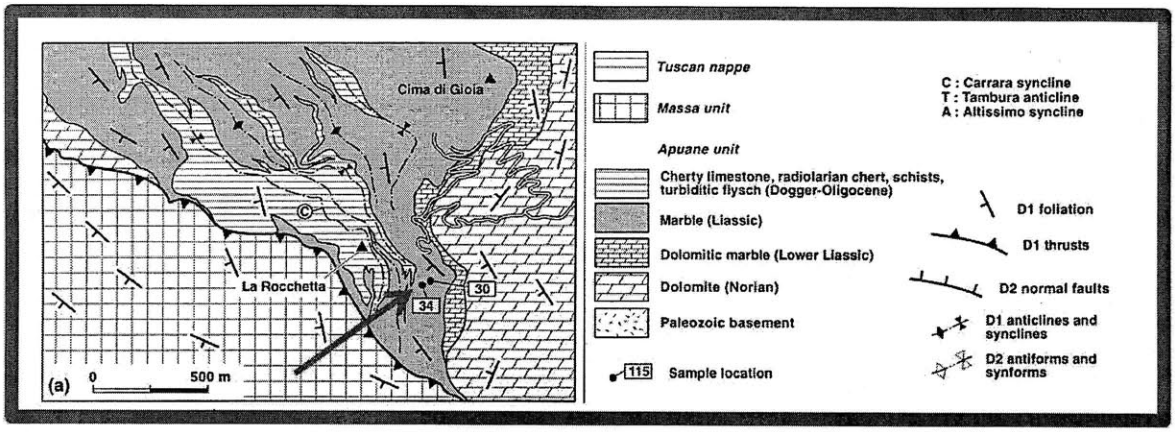

Figure 3-2: Close-up of the boxed region in Figure 3-1. The arrow indicates the precise origin of the marble used in the study, the normal limb of a northest-facing isoclinal fold.

B microfabric consists of a dynamically recrystallized microfabric, and references the end of the first geologic event: stacking after the nappe emplacement. The final microfabric, Type C, is a twinned microfabric. This microfabric suggests the second geologic event: deformation, in conjunction with folding and the development of shear zones.

To summarize, after an early folding stage, thermal relaxation occurred, and then heating to statically recrystallize the rock and produce the annealed Type A microfabric. Stacking reworked the Type A microfabric into the dynamically recrystallized Type B microfabric. Finally, late deformation produced the twinned Type C [51].

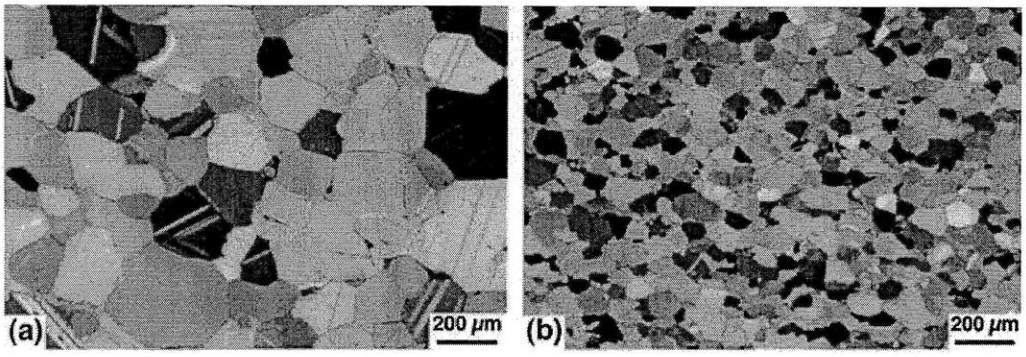

Figure 3-3: Both images are Type A microfabric, but have different microstructures [Molli 2000].

Whereas microfabric describes the shape, arrangement and orientation of the grains, microstructure describes the individual grains in particular. Two main microstructures dominate: coarse grains with a typical size of 150 – 200 μm (this microstructure corresponds with the material used in this investigation), and fine grains with a size of 40 – 50 μm (Figure 3-3). The relatively pure and homogenous microstructure of Carrara marble makes the rock an interesting material for scientific research, especially in the area of rock mechanics [51].

3.2 Method

The study seeks answers to the question of the type, scale, and behavior of the micromechanism which controls the cracking of marble. These answers rest in the microstructure and nanomechanical properties of intact and process zone materials. Thus, the very core of the experimental investigation is the monitoring of the microstructural appearance, nanoindentation modulus, and nanoindentation hardness of intact and process zone materials. Three techniques are used to obtain these microproperties and relate them to macroscale crack initiation:

1. *Digital Photography*, to visually assess macrostructure and crack formation,
2. *Environmental Scanning Electron Microscopy (ESEM),* to visually assess microstructure, and
3. *Nanoindentation*, to yield micromechanical properties and assess microheterogeneities.

The techniques collectively assess cracking of a particular brittle material, marble, from the macroscale through the microscale, and link directly with previous work by Wong [73][74]. Whereas Wong visually related macroscale cracking behavior with the initiation and propagation of cracks at the microscale, this investigation uses the tool of nanoindentation to pursue the micromechanisms of crack initiation and coalescence of marble.

3.2.1 Specimen Preparation

Two block specimens were prepared to explore the influence of loading and load type on the microproperties (Figure 3-4):

1. *Intact Specimen*: a specimen with no process zone.

2. *Flawed Specimen*: a specimen with a single flaw, but no process zone (not shown in Figure 3-4).

3. *Process Zone Specimen*: a specimen with a flaw and a process zone.

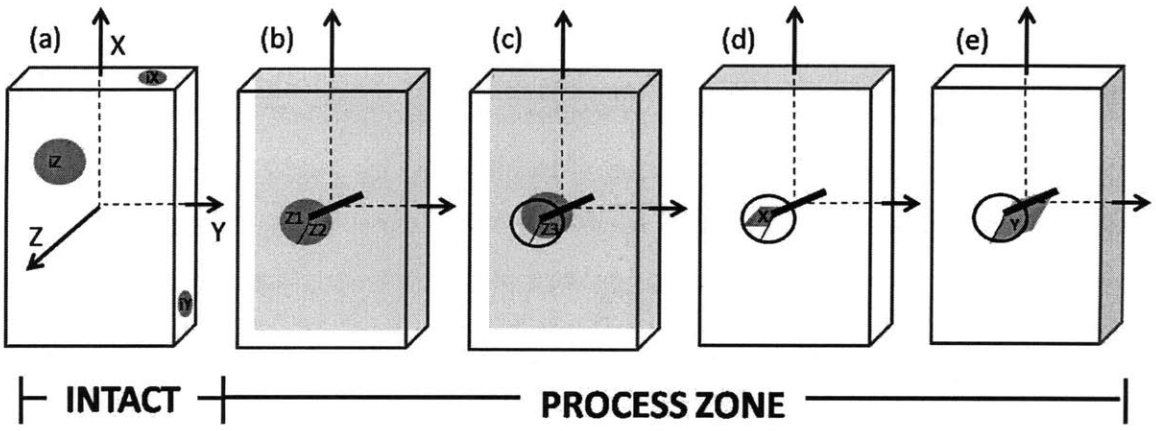

Figure 3-4: Two specimens (Intact, and Process Zone) were prepared for this investigation. Dark gray regions indicate surfaces extracted for nanoindentation testing and microscopy, and are parallel to the corresponding shaded face (i.e., axis of nanoindentation is axis corresponding to shaded plane). (a) "Intact" Specimen, testing surfaces normal to X, Y, and Z, (b) "Process Zone" Specimen, testing surface normal to Z (i.e., parallel to top surface of cylindrical specimen) (c) "Process Zone" Specimen, testing surface within slab normal to Z (i.e., parallel to top surface of cylindrical specimen) (d) "Process Zone" Specimen, testing surface normal to X (i.e., parallel to long axis of cylindrical specimen) (e) "Process Zone" Specimen, testing surface normal to Y (i.e., parallel to short axis of cylindrical specimen).

As indicated in Figure 3-4, smaller specimens were removed from the Intact and Process Zone Specimens for microscopy and nanoindentation testing. This section details the six steps to create these specimens.

Cut Samples

Slices of marble were cut from a Carrara marble slab with a Covington Engineering Heavy Duty Slab Saw in the Department of Earth, Atmosphere, and Planetary Sciences at MIT (Figure 3-5). In this saw, a large disk rotates at a constant speed. The marble slab slides by its own

self-weight along a track towards the disk. Abrasives embedded in the sides of the disk abrade the marble to ultimately cut through the marble. The process is slow, and induces a relatively small amount of stress.

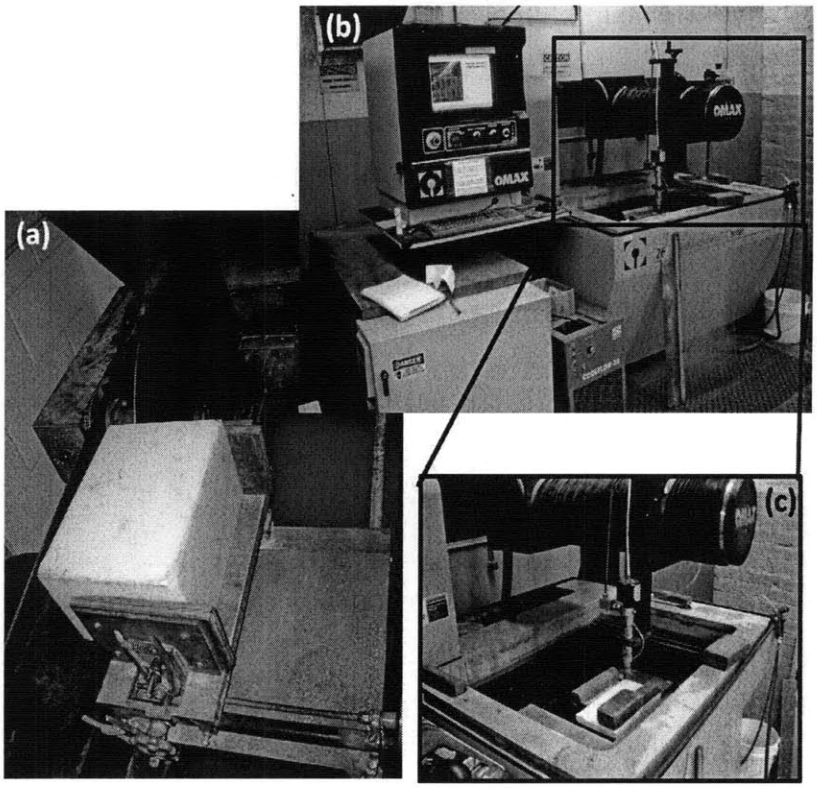

Figure 3-5: The tools used to cut the samples: (a) Covington Engineering Heavy Duty Slab Saw, (b) OMAX Water Jet, and (c) close-up of sample prior to cutting in Water Jet.

The slices of marble were then trimmed into 6" x 3" x 1.5" (15.2 cm x 7.6 cm x 3.8 cm) block specimens with an OMAX© Water Jet in the Hobby Shop at the Massachusetts Institute of Technology (Figure 3-5). As a basis of comparison, the dimensions were selected to conform to those of a previous study by Wong [73]. The Water Jet operates by emitting a high-pressure stream of water and garnet, an abrasive, at a user-selected rate and trajectory. This cutting method also induces a relatively small amount of stress in the specimen.

Generate Flaw

In order to generate different types of loading, an initial crack, or "flaw", was cut into two specimens with the OMAX© Water Jet. No flaw was cut into the Intact Specimen ((a) of Figure 3-4), but a flaw oriented 30^o from the horizontal short axis was cut into the Process Zone Specimen ((b) through (e) of Figure 3-4).

Note that the orientation of the flaw grants the specimen a Mixed-Mode loading condition when loaded in a uniaxial testing machine (Figure 3-6). Whereas Mode I cracks propagate perpendicular to the in-plane far-field stress, and Mode II cracks propagate parallel to the in-plane far field stress, the propagation of a diagonal pre-existing crack has both perpendicular (i.e., Mode I) and parallel (i.e., Mode II) components; the Mode I and Mode II stress intensity factors have formulations:

$$K_I = \sigma\sqrt{\pi a}\cos^2(\alpha) \tag{3.1}$$

$$K_{II} = \sigma\sqrt{\pi a}\cos(\alpha)\sin(\alpha) \tag{3.2}$$

For a flaw length of $a = .0013\,\mathrm{m}$, and an inclination $\alpha = 60^o$, the magnitude of the stress intensity factors under a tensile load with equal magnitude to the compressive stress of the current investigation would be $K_I = 0.272\ \mathrm{MPa}\sqrt{\mathrm{m}}$ and $K_{II} = 0.470\,\mathrm{MPa}\sqrt{\mathrm{m}}$. The stress field in the vicinity of the crack tip superimposes the Mode I and Mode II stress components:

$$\boldsymbol{T} = [\boldsymbol{\sigma}^I + \boldsymbol{\sigma}^{II}] \cdot \mathbf{n} \tag{3.3}$$

where $\boldsymbol{\sigma}^I$ and $\boldsymbol{\sigma}^{II}$ refer to the stress fields due to the Mode I and Mode II stress fields (i.e., due to the perpendicular and parallel components of the applied stress, respectively), and T is a stress vector on a plane near the crack tip with unit normal $\mathbf{n}$. Thus, the propagation is termed Mixed-Mode [69].

Nevertheless, note that in the case of the current investigation, the applied stress is compressive, the stress field is negative, and the above model must be accordingly modified. The potential exists for tensile stresses to act at the tips of the flaw to generate the white patching, as indicated in Figure 3-7. At the flaw, the heterogeneity of the stress field (i.e., the flow of

the compressive stresses around the flaw) may be responsible for this tensile opening.

Generate White Patching

White patching was generated in the Process Zone Specimen by loading in a uniaxial testing machine (Figure 3-8). The samples were loaded through the vertical long axis. Steel brush-platens at the top and bottom of the sample ensured that far-field stresses were homoegenously applied.

The loading sequence was as follows. Each sample was loaded at a slow initial rate to eliminate seating effects. After the load reached a preset initial stress, loading continued at a constant rate. The flaw tip was continuously monitored with a high-resolution Phantom© High-Speed Camera from the Edgerton Center at MIT, and high-resolution still pictures were taken at intervals with this camera. Once a significant amount of white patching had developed at the flaw tip, the load was reversed and the sample was unloaded. The final process zone and flaw were imaged with an ACME, Inc. Digital Camera from the Rock Mechanics Group in the Department of Civil Engineering at MIT.

Extract White Patching

The smaller surfaces (dark regions in Figure 3-4) were extracted as follows: the OMAX© Water Jet cut 12 mm cylinders which contained the region of interest. These cylinders correspond with the scale of both the observed white patching and the theoretical process zone predicted by LEFM (Table 2.1).

A diamond drop-saw sliced the cylinder to obtain a disc of the region of interest (Figure 3-9). The final discs had a diameter of 12 mm, and a height of less than 4 mm. The discs were then mounted on stainless steel AFM plates with cyanoacrylate, and prepared for nanoindentation as described in Section 3.2.1.

During extraction with the Water Jet, Surfaces Z1 and Z2 (Figure (b) of Figure 3-4) separated along the white patching. These specimens were mounted, prepared, and tested separately (Figure 3-10).

Image White Patching

The white patching of the Process Zone Specimen was visually assessed with the FEI/Philips© XL30 FEG ESEM, in the Center for Materials Science and Engineering Electron Microscopy Shared Experimental Facility at MIT (See Section 2.3: Scanning Electron Microscopy (SEM) and Environmental Scanning Electron Microscopy (ESEM) for a detailed explanation of ESEM). The ESEM emits electrons at a controlled rate and trajectory onto the surface of a sample. Information about surface topography, material contrast, and other sample properties is derived from the deflection of the electrons off of the sample surface, or absorption and emission of electrons from the sample [57].

Surface Preparation for Nanoindentation

All specimens required proper surface preparation before nanoindentation testing. Surface preparation is a vital aspect of any nano- or microscale investigation, and is especially important for micro- and nanomechanical investigations. The ultimate goal is to obtain a smooth surface that best approaches the infinite half-space model of indentation contact models from which Equations (2.21) and (2.11) derive. Furthermore, minor deformations disrupt the motion of the nanoindenter head, and thereby induce inaccurate data or scatter. In other words, the derived indentation properties exhibit greater spread for surfaces with a high roughness, but not necessarily an overal decrease in properties [50].

Polishing, or rubbing the sample surface with abrasives in stages of decreasing abrasive size, reduces roughness and enhances nanoindentation results. Micro- and nanomechanical investigation of geomaterials is a relatively new field, so a well-established surface preparation procedure for marble did not exist in the literature at the time of this investigation. Ultimately, two surface preparation procedures were combined to develop the marble surface preparation procedure used in this study: the optical microscopy surface preparation procedure for marble, and the nanoindentation surface preparation procedure for cement paste [50][4] (Figure 3.2). The optical microscopy surface procedure suggested the abrasive types and sizes, and the cement paste surface preparation procedure suggested the long duration of the final stage, as well as the type of polishing equipment. The initial and final polishing stages are conducted on an automated turntable. The sample is secured within a cylindrical steel "jig" and beneath a steel

Stage	Abrasive Size (μm)	Abrasive Type	Lubricant	Duration
1	76	Silicon Carbide	none	5 min
2	22	Aluminum Oxide	none	5 min
3	9	Diamond	Oil	5 min
4	3	Diamond	Oil	5 min
5	0.25	Diamond	Oil	9 hr

Table 3.2: Specimen surfaces are prepared for nanoindentation with a five-stage polishing procedure.

"post" (Figure 3-11). The jig and post ensure that the sample rotates about its own axis in addition to the rotation of the table. This double rotation creates an even polish by reducing any tracks or scratches due to polishing.

After an initial stage of testing on the specimens, the specimens were re-polished more intensively (i.e., with a longer duration of the final polishing stage) to expose a smoother surface within the white patching region.

The Asylum Research MFP-3D AFM© at the Nanolab in the MIT Department of Material Science verified the adequacy of this polishing procedure. An Atomic Force Microscope (AFM) is a type of Scanning Probe Microscope (SPM) which traces surfaces with a silicon cantilever to develop high-resolution, microscale interpretations of surface topography. The force of the silicon cantiliver must be closely monitored to prevent damage to the sample surface, and also to correctly calibrate its height at any given moment. Piezocrystals control this force. The height and displacement of the cantilever is monitored by a laser; an incident laser beam reflects off of the cantilever onto a photodiode. The position of the reflected laser beam on the photodiode reveals cantilever height information [29].

Following statistical corrections for surface sloping and large scale surface waviness, the final roughness, was determined from (via Mountains SPM Image Analysis Software; Figure 3-12):

$$R_q = \sqrt{\frac{1}{N^2}\sum_{i=1}^{n}\sum_{j=1}^{n} z_{ij}^2} \tag{3.4}$$

where N is the number of pixels along the edge of the AFM scan, and z_{ij} is the height at a position (i, j) above or below a mean reference plane [50]. Essentially, the roughness value represents the average distance from a reference point near the sample surface to the highest

peaks or the deepest valleys on the surface. The scans in this investigation had a resolution of 40 pixels by 40 pixels, and a size of 50 μm by 50 μm. This yielded a final roughness of $R_q = 9.32$ nm. Figure 3-12 (c) depicts the topographical information from a single scan; the dark line through the middle represents the reference point. Roughness is formulated with respect to distances from this datum.

Existing surface roughness criteria for nanoindentation recommend, dependent on the scanning size, a roughness less than five times the depth of nanoindentation [50]. Thus, the above polishing procedure represents an adequate polish for nanoindentation tests conducted to a minimum depth of 50 nm. Nanoindentations in this investigation were conducted to a peak load of 2.85 mN and a typical maximum depth of 250 nm; thus the sample preparation is sufficient for this investigation. A consideration of surface roughness should also consider the scale separability condition (Equation (2.37)). If this condition is satisfied, indentation to a depth h will reveal information about the material properties at the scale of the elementary volume L. Both the indentation depth $h = 250\,\text{nm}$ and the characteristic material microstructure length scale $D = 300\,\mu\text{m}$ greatly exceeds the heterogeneity of roughness with $d = 9.32\,\text{nm}$. Thus, as interpreted by nanoindentation, the roughness serves as a sub-microstructural component potentially on the same order as other heterogeneities of interest. Nevertheless, consistent low roughnesses ($5R_q < h$, for a scan size of length $l \approx 200h$) for each specimen should still allow for the accurate interpretation of nanoindentation results [50].

3.2.2 Testing Approach

This section details the application of nanoindentation to the specimens in this investigation. In this study, a nanoindentation "test" consists of several hundred nanoindentations over an area. Although these areas may seem small in comparison to the specimen dimensions, the large number of nanoindentations conducted within the area successfully captures trends and variations in microproperties. These trends and variations ultimately reveal the information sought by this investigation: the difference between process zone and intact brittle materials.

Technique

Nanoindentation tests were conducted on the CSM Instruments Nano-Hardness Tester in the Geomaterials Laboratory in the MIT Department of Civil and Environmental Engineering. For this investigation, nanoindentations were conducted to a maximum load of 2.85 mN and a typical depth of 250 nm, which corresponds to a typical contact area of 900,000 nm^2. The tests were conducted with a CSM Instruments Nano-Hardness Tester (Figure 3-13). The nanoindentation testing geometry was designed to capture trends in nanomechanical properties over extensive areas. Each nanoindentation test series typically consists of more than 300 individual nanoindentations, conducted in either a straight line or grid geometry.

Accuracy of Experimental Technique

The accuracy of nanoindentation data from the CSM Instruments Nano-Hardness Tester is enhanced by an additional "depth-offset" calibration before the nanoindentation test begins. During the depth-offset calibration, the specimen is raised to make contact with a plastic reference ring which surrounds the indenter head (Figure 2-2). Then the indenter head lowers within the plastic ring to contact the sample and create a single, large indentation. The position of the indenter head relative to the plastic ring at contact serves as the initial depth-offset calibration, and a reference value for all indentations in the test [10]. During the indentation test (which consists of hundreds of individual indentations), each indentation is conducted with respect to this localized system. Before each individual indentation the sample is again raised to contact the plastic ring, and after each indentation, the sample is lowered from the plastic ring (Figure 2-2). During each indentation, the indenter head lowers to the sample surface, conducts an indentation, and retracts. Moving with respect to the plastic ring minimizes any error associated with thermal drift of the sample or vibrations of the system. If the sample expands or contracts due to vibrations or a slight temperature change in the environment during the test, the indentations will still be conducted and measured with respect to the current sample dimensions. [10].

Additionally, the testing parameters were carefully selected to ensure the accuracy of the experimental technique. Nanoindentations conducted to high loads or at high loading rates may fracture the material. Fractures extending from one nanoindentation to the next would in-

	"Exaggerated" Indentation	Typical Indentation
P_{max} *(mN)*	250	2.85
Depth of Indentation (nm)	2800	240
Inter-indentation Spacing (μm)	—	8
Length of Indentation-induced Fracture (μm)	< 17.6	neligible

Table 3.3: A comparison of typical indentations and a large-load "exaggerated" indentation.

fluence the mechanical properties derived from nanoindentation testing. For this investigation, it was checked and verified that nanoindentations do not induce significant fracture, if spaced at 8 μm. To investigate this potentiality, "exaggerated" nanoindentations were imaged with ESEM (Figure 3-14). These nanoindentations were "exaggerated" because they were conducted at higher loads (by a factor of nearly 100) than typical indentations in the testing campaign.

Cracks extending from one indentation to the next would indicate that the nanoindentation process induced significant fracture in the material. However, as shown in Figure 3-14, indentations 80 times the typical load do not induce cracks extending more than 17.2 μm. It is inferred that typical, low-load indentations would induce cracks of insignificant length. Typical indentations were also imaged with ESEM. Note that inter-indentation cracks are not visible at even high magnifications, and are thus assumed insignificant.

A look to the scale separability condition (Equation (2.37)) provides a quantitative corollary to the qualitative discussion of indentation spacing. Indentation parameters (spacing between indents s, and depth h) must be carefully selected in order to prevent not only the overlap of indented areas, but also more importantly the overlap of the accessed indentation volumes. As indicated in Table 3.3, the typical depth of indentation h is 240 nm. Provided that the typical microstructure size D is 2.4 μm or larger, the indentations provide information on the material properties of the the microstructure. As discussed in the next section, typical marble grain sizes in this study are upwards of 100 μm; thus, the indentation depth is well within the sought-after scale separability range for this investigation.

A final note of interest is the quality of indentation-induced fracture (in the case of the exaggerated indents, microindentation-induced). Slightly curving cracks emanate from the top and right tips of the impression (see right half of Figure 3-14); they resemble classic tensile wing

cracks [73]. Additionally, sets of deformation lines parallel to the impression extend outwards from the impression. The regularity and straightness of the lines contrasts with more irregular macro- and microscale crack propagation around grain boundaries. These deformation lines ultimately indicate the regularity of the crystal microstructure of marble within the particular marble grain imaged.

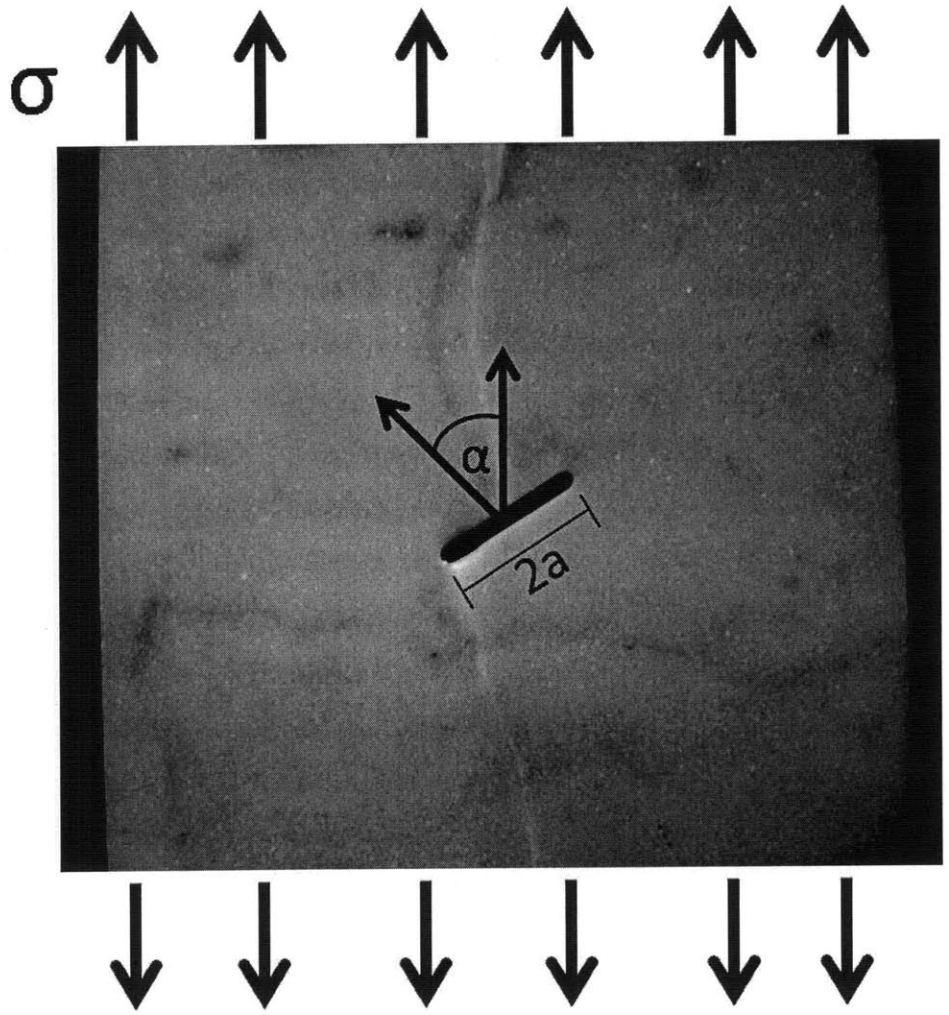

Figure 3-6: Physical quantities of importance when determining stress intensity factors for a mixed-mode loading condition.

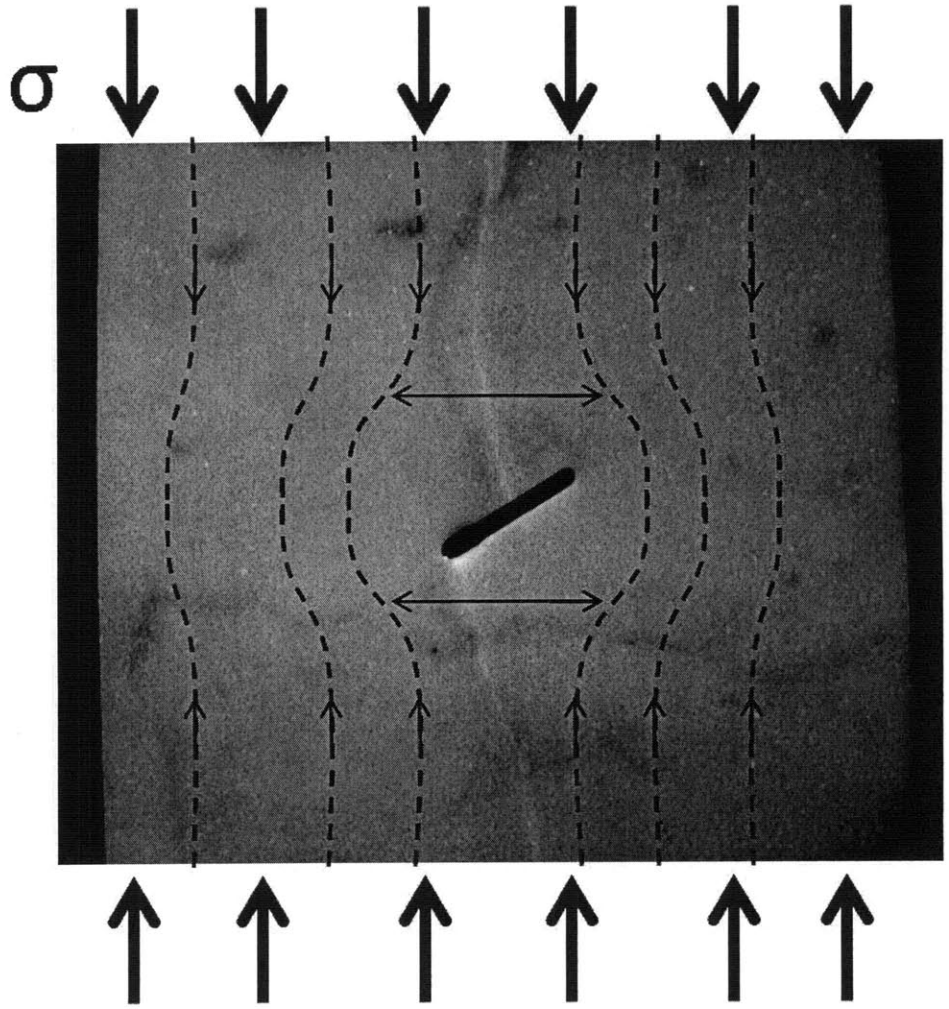

Figure 3-7: The heterogeneity of the compressive stress field (i.e., stresses flow around the flaw) may be responsible for the tensile conditions at the flaw tip which generate the white patching.

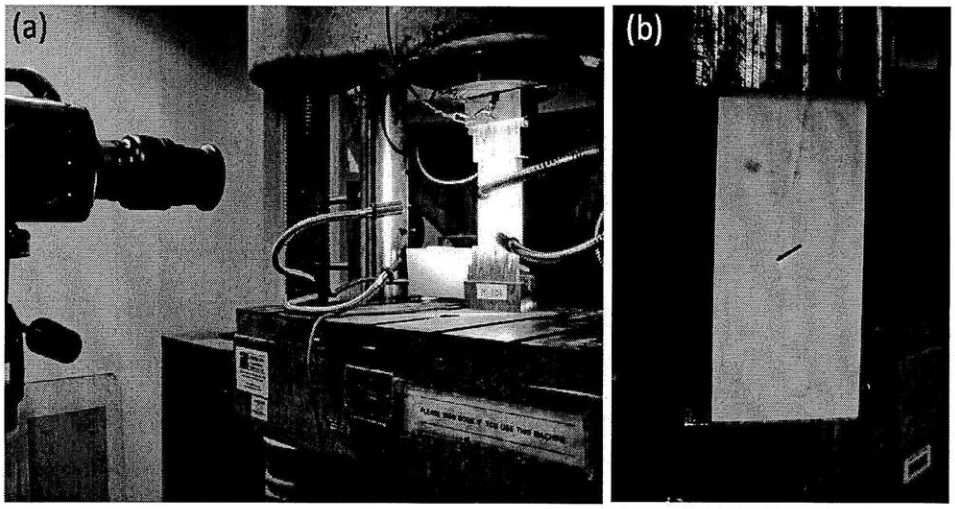

Figure 3-8: (a) Typical test setup including Phantom© High-Speed Camera on left, and sample in uniaxial testing machine on right. (b) Close-up of Process Zone Specimen with steel brush-platens in uniaxial testing machine, post-loading.

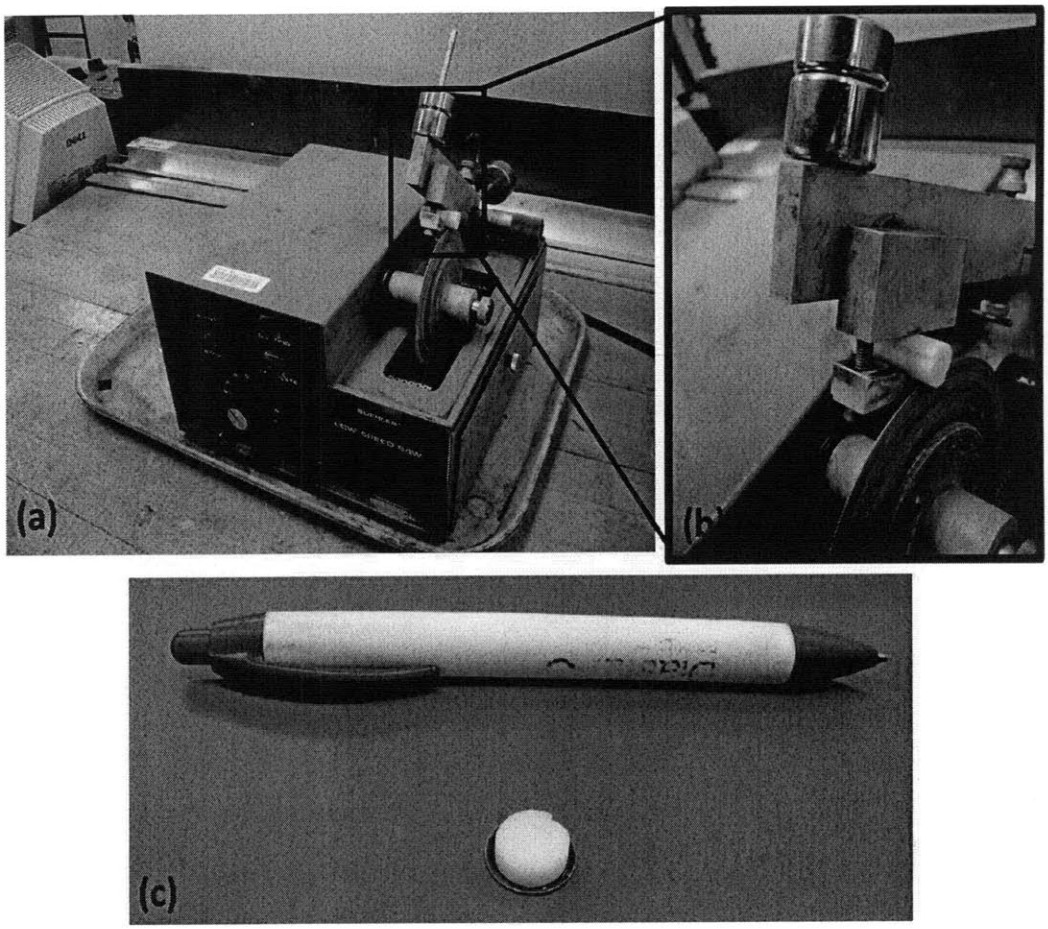

Figure 3-9: (a) The diamond drop-saw trimmed marble cylinders cut with the OMAX© Water Jet. (b) Close-up of diamond-drop saw cutting a marble cylinder. (c) Final specimen mounted on stainless steel AFM plate.

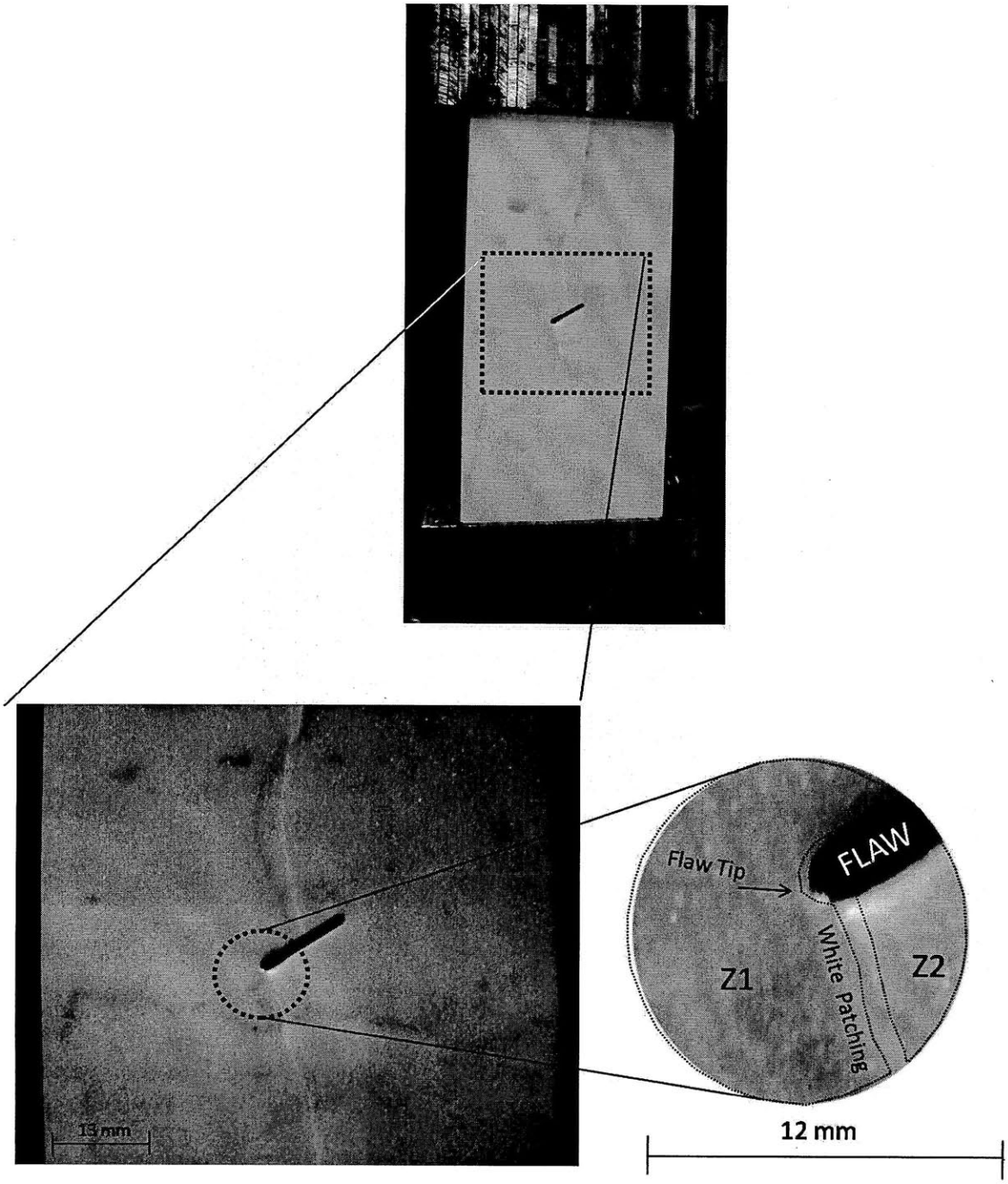

Figure 3-10: Detail of (b) in Figure 3-4. Surfaces Z1 and Z2 separated from either side of the white patching during cutting.

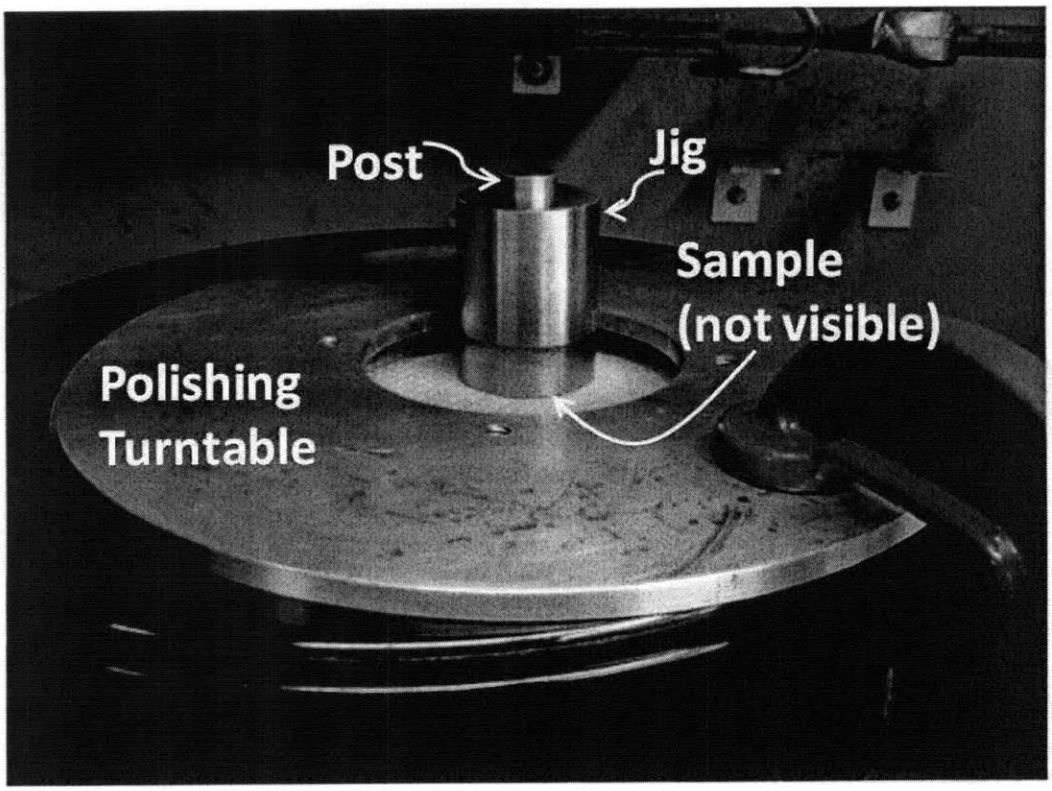

Figure 3-11: The sample (not visible) is secured within a cylindrical steel "jig" and beneath a steel "post" so as to come in direct contact with the polishing pad on the polishing turntable. Adapted from [10].

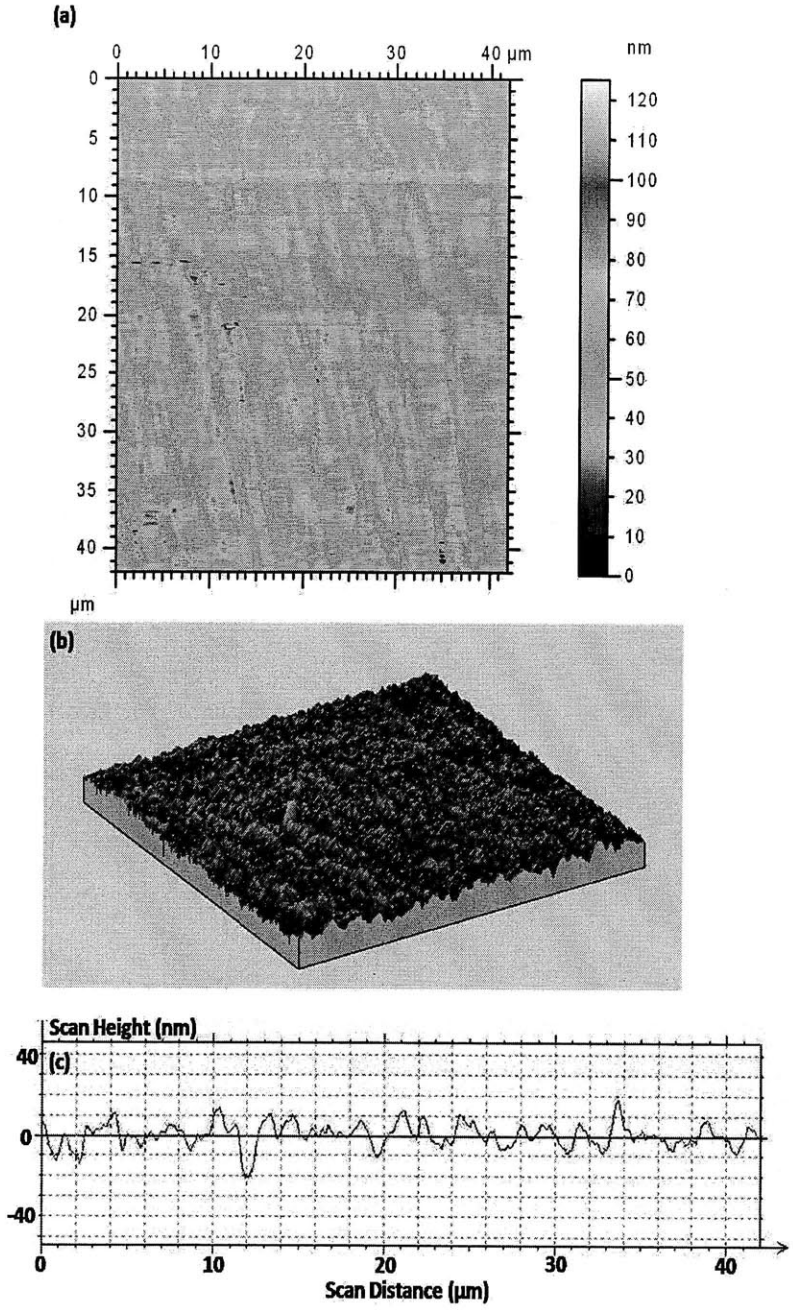

Figure 3-12: An AFM scan yields (a) a color-gradient contour plot of the surface, which may also be displayed as (b) a 3D isometric diagram. (c) depicts height information from a single scan with respect to a reference point, or datum.

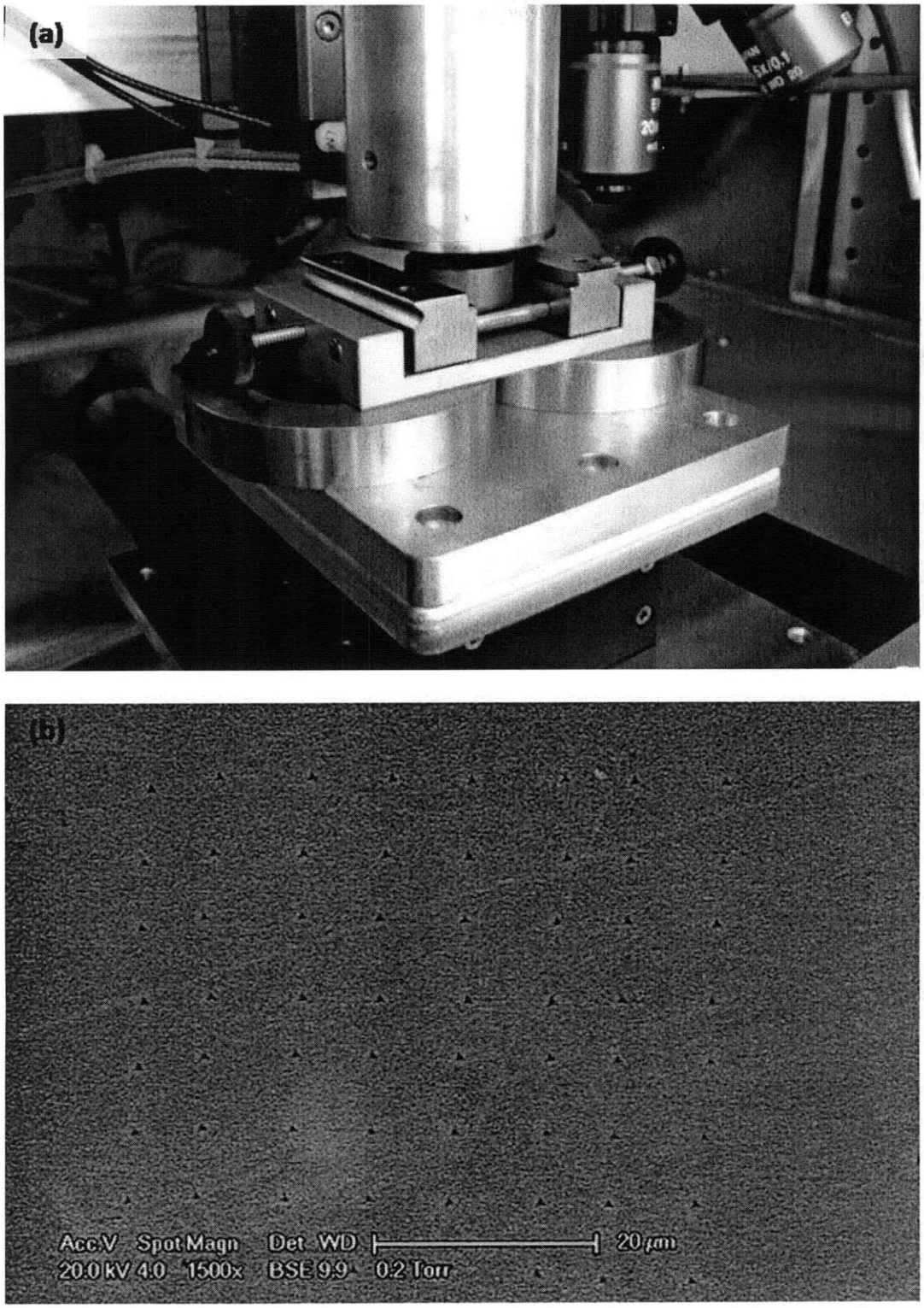

Figure 3-13: (a) The CSM Instruments Nano-Hardness Tester. (b) An ESEM image of a grid indentation test. Line indentation tests resemble a single row from a grid indentation test.

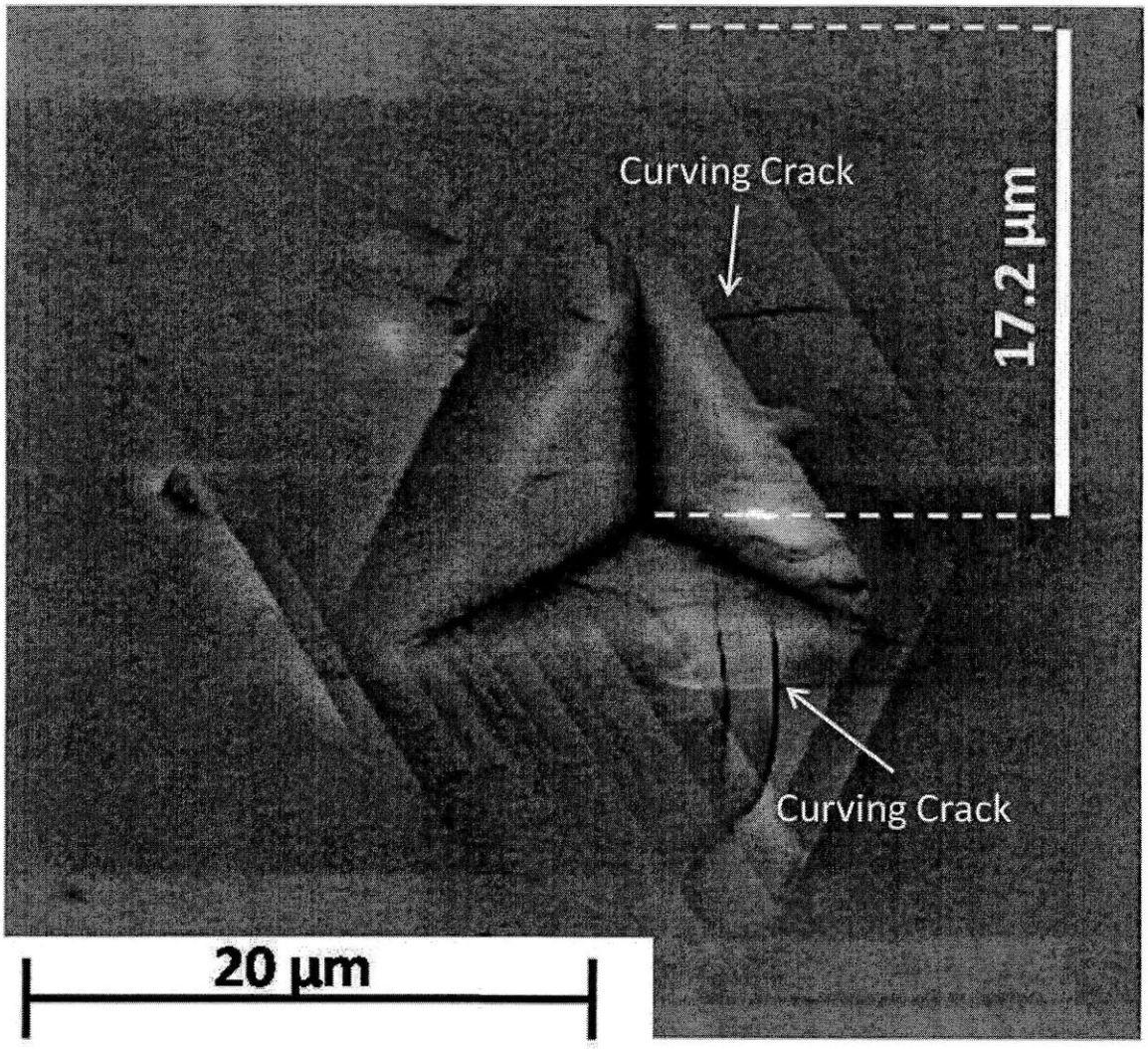

Figure 3-14: An "exaggerated" indentation shows little indentation-induced cracking.

3.3 Chapter Summary

This chapter has presented the precise investigative technique employed in the study. A review of the material selection and introduction to the analytical technique was also presented. The next section explores the results obtained by this investigative technique; these results are the first answers towards the fundamental research question of the precise mechanism at play in the process zone.

Chapter 4

Results

Two clues provide information about what is actually happening at the tip of a propagating crack: the differences in microstructure between intact and process zone materials, and the differences in nanomechanical properties between intact and process zone material. This chapter presents these key findings. These differences are the first answers to the essential question of the type and scale of mechanism which fundamentally drives the cracking of marble. First, the chapter presents images from ESEM conducted on both intact and process zone specimens. Then, the results of nanoindentation on both intact and process zone specimens are presented.

4.1 ESEM Results

As a reminder, two samples – one Intact and one Process Zone – were explored with various specimens for this study. Figure 3-4 presents an overview of all specimens explored with nanoindentation, microscopy, or both.

The first approach which investigates the crack tip process zone is the differences in microstructure between intact and process zone materials. This section presents the results as obtained by ESEM.

ESEM was applied to two types of specimens: intact, and process zone. The features measured were grain size and shape, and the nature of the grain boundaries, or separation between grains. These features were identified as critical to the process zone in previous work by Wong [73], but in this study they are captured at a higher magnification, at various scales,

and at their most intact state. Also in previous studies, the features were viewed only on specimens that had been polished and carbon-sputtered; here they are visible with no surface preparation [73].

The process zone in marble contains two characteristic features [73]: microcracks (both intergranular and intragranular), and spalling (Figure 4-1). In intact marble, the grains of marble lie very close to each other with no distinct separation. The visible separation of one marble grain from an adjacent marble grain is interpreted as a microcrack. This separation manifests as thick, dark, and very distinct grain boundaries. Spalling is the removal of material from the surface. This feature manifests as large, often triangular pits both within and on the boundaries of marble grains.

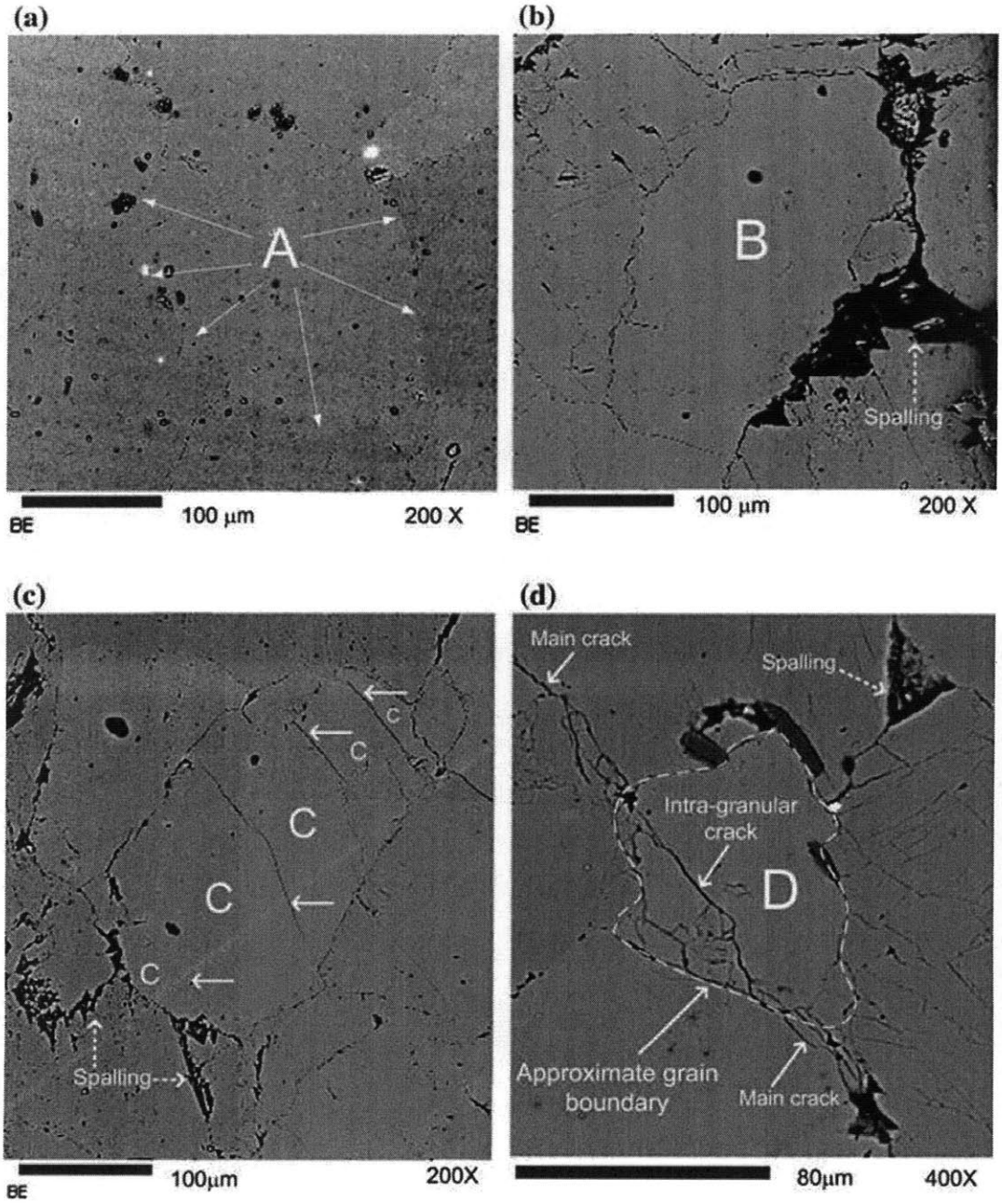

Figure 4-1: Established microstructural features of the process zone in marble viewed with standard Scanning Electron Microscopy. a) Intact marble grain b) Intergranular cracking c) Spalling d) Intergranular and intragranular cracking. From [3].

4.1.1 Microstructure of Intact Material

A region around the tip of the flaw of an unloaded sample was viewed with ESEM (Figure 4-2).

The flaw was cut with the OMAX© Water Jet (Section 3.2.1). The lack of microcracks in the region indicates the minimal stress imposed by the Water Jet. The image provides an overal assessment of flaw tip microstructure in intact material.

4.1.2 Microstructure of Process Zone Material

Specimen Z1

Immediately after process zone generation and separation, and without surface preparation, the pre-existing flaw tip and adjacent white patching of Specimen Z1 (Figure 4-3) were imaged with ESEM. The white patching extended from the tip of the pre-existing flaw to the tip of the propagating crack (Figure 4-4).

By not polishing the specimen or utilizing any type of surface preparation, the original crack pattern is preserved. As indicated in Figure 4-3, the specimen unfortunately fractured in the white patching between marble grains during preparation. The surfaces of the subsequently exposed marble grains are clearly visible on the bottom of the image, as well as along the right side of the image. Widened grain boundaries (at the tips of the red arrows in Figure 4-4) are evidence of microcracks that have propagated through grain boundaries.

The arch on the top right of the image (circled in Figure 4-4) is the tip of a flaw cut by the water jet. The edges of the flaw are smooth and virtually free of microcracks, whereas the white patching displays many distinct grain boundaries. It can be concluded that microcracks do not occur at the tip of the pre-existing flaw under mixed-mode loading conditions, but rather start at another location along the flaw boundary.

Specimen Z1 was polished and tested with nanoindentation, then re-imaged with ESEM as a means of determining the influence of sample preparation (polishing) on process zone microstructure (Figure 4-5).

Fewer microcracks are apparent in the polished specimen compared to the unprepared specimen, but a few microcracks (Figure 4-6) and a region of spalling (Figure 4-7) is visible. Note that the spotlight effect (explained in the Appendix, Section A.2.1) is especially apparent

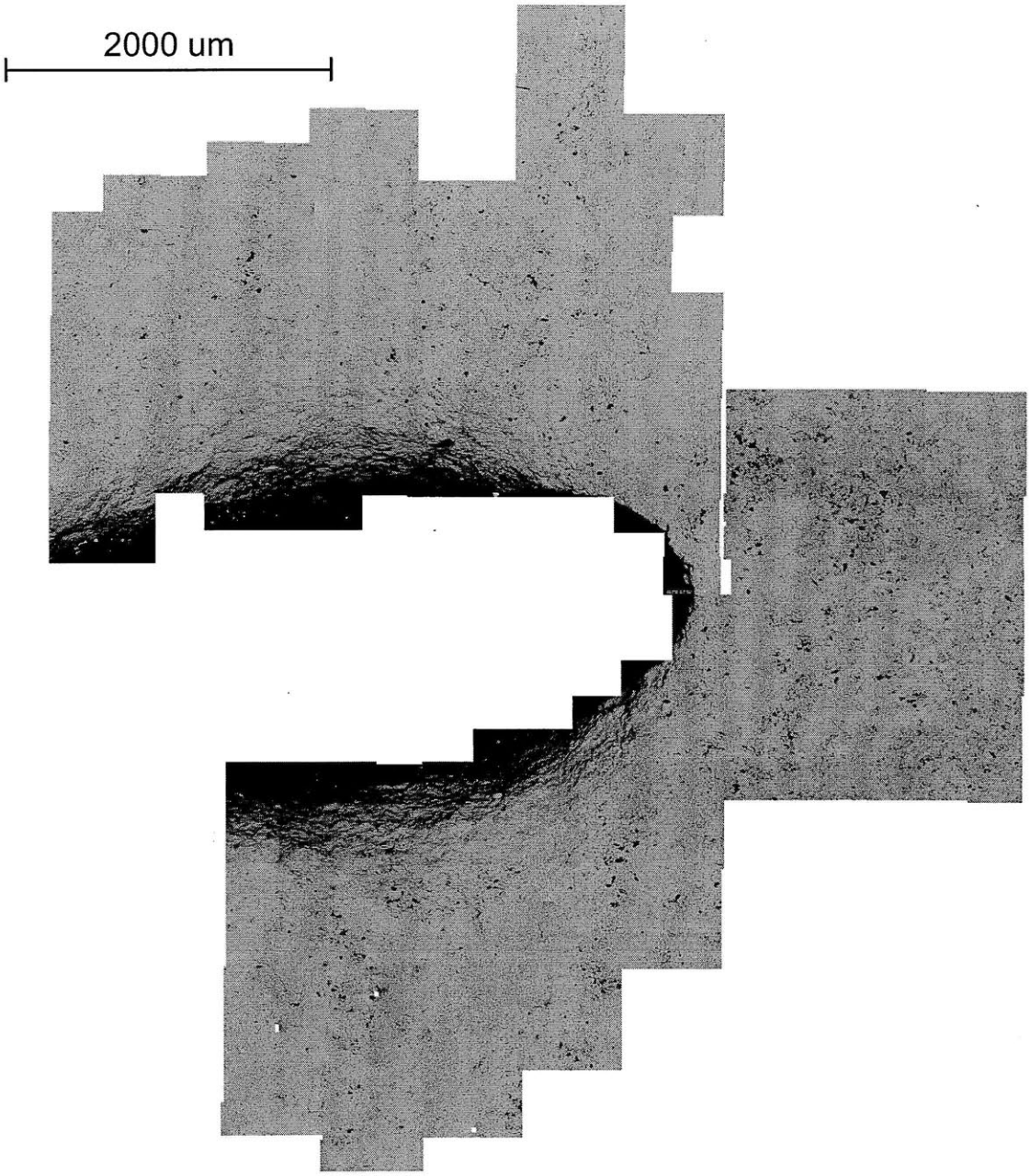

Figure 4-2: Tip of pre-existing flaw, viewed with the FEI/Philips XL30 FEG Environmental Scanning Electron Microscope (ESEM). After loading, the process zone will lie in and near this region. The lack of microcracks in the region indicates the minimal stress imposed by the Water Jet. The image provides an overal assessment of flaw tip microstructure in intact material.

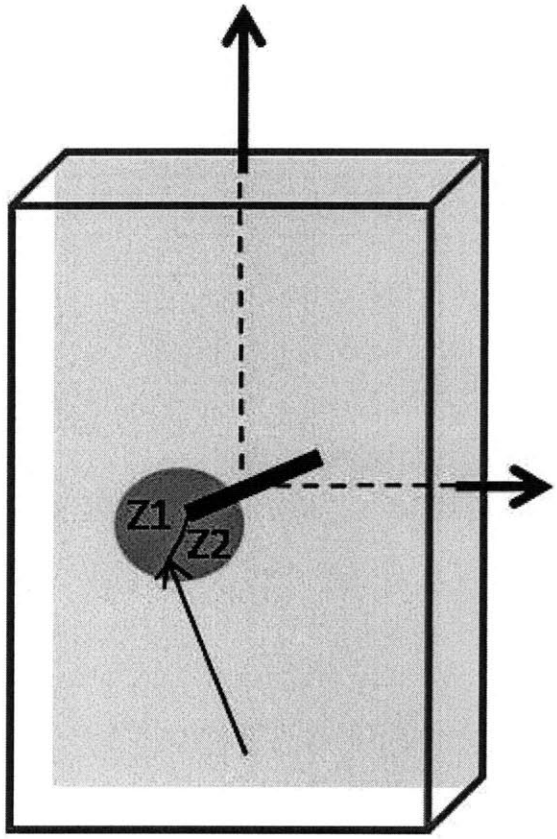

Figure 4-3: Excerpt from Figure 3-4. White patching at the edge of Specimen Z1 (indicated by arrow) was imaged with ESEM. The ESEM images are displayed in the next figure.

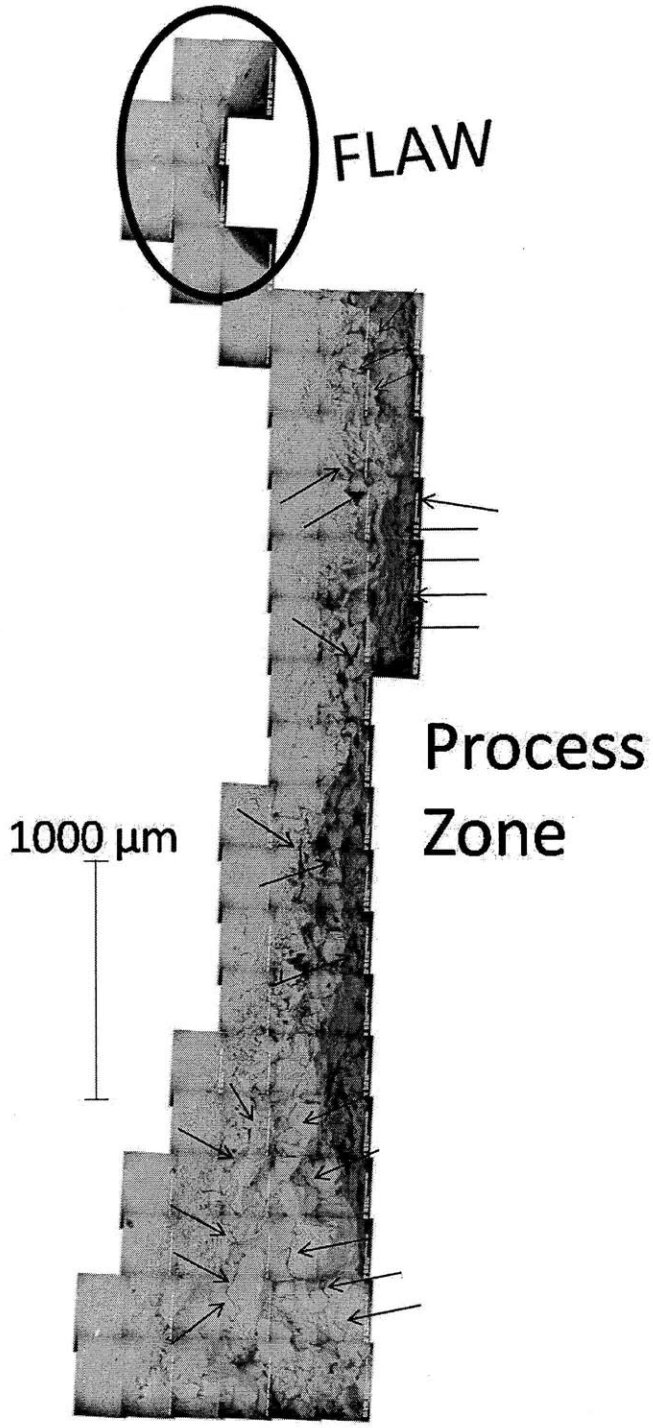

Figure 4-4: Process zone region on Specimen Z1. Widened grain boundaries, indicated by red arrows, are evidence of microcracking.

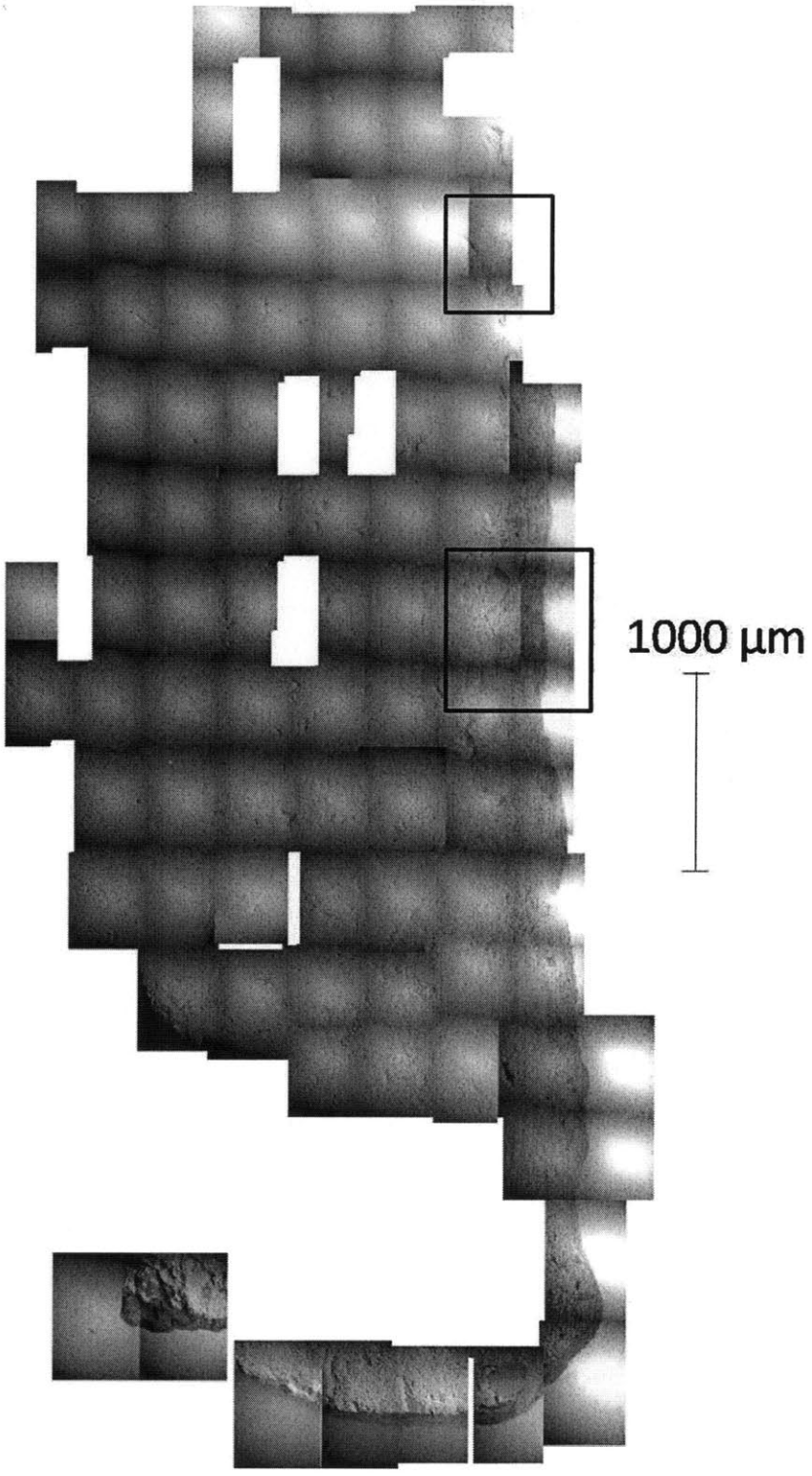

Figure 4-5: Specimen Z1 was polished and tested with nanoindentation, then re-imaged with ESEM. Sample preparation has significantly reduced the number of apparent microcracks and spalling (compare with previous figure).

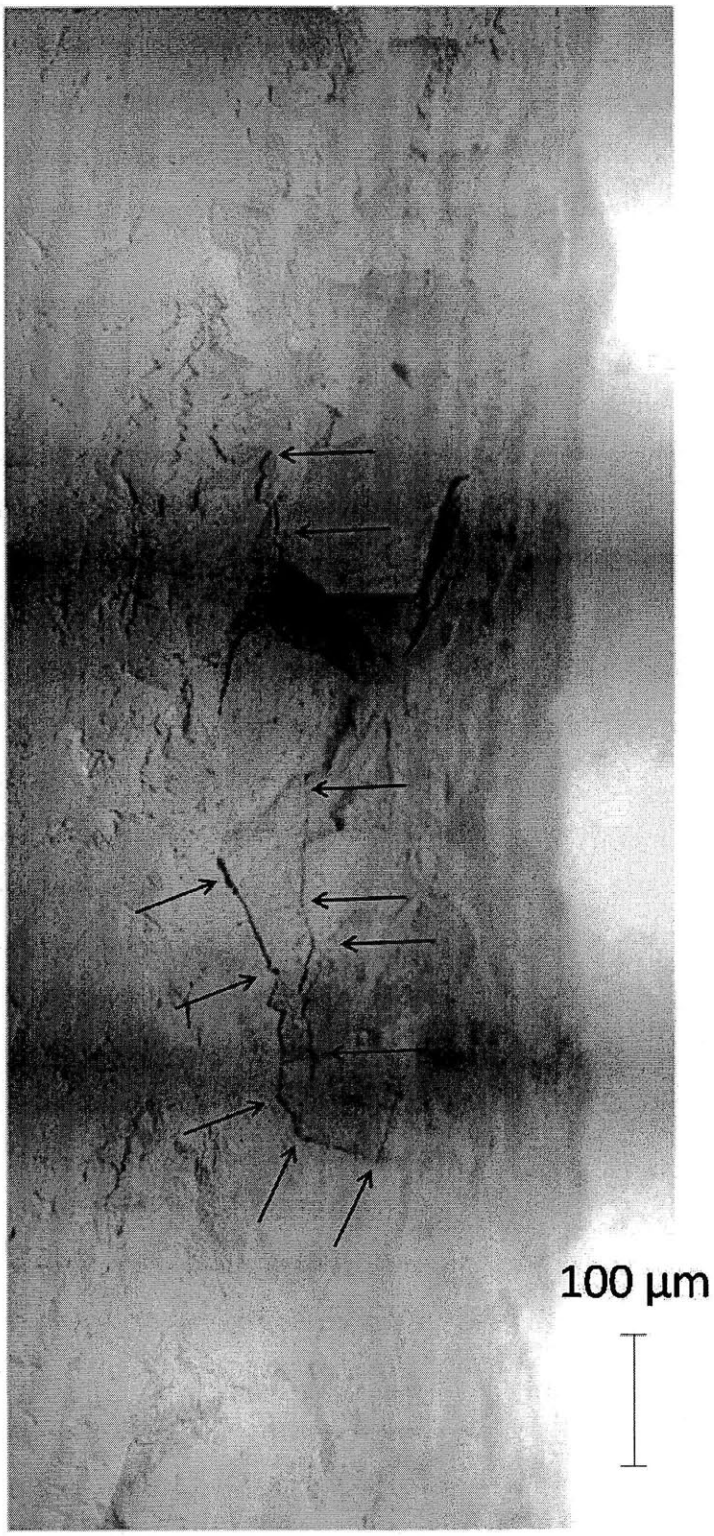

Figure 4-6: Despite surface preparation, a few microcracks (indicated by arrows) are still visible on Specimen Z1.

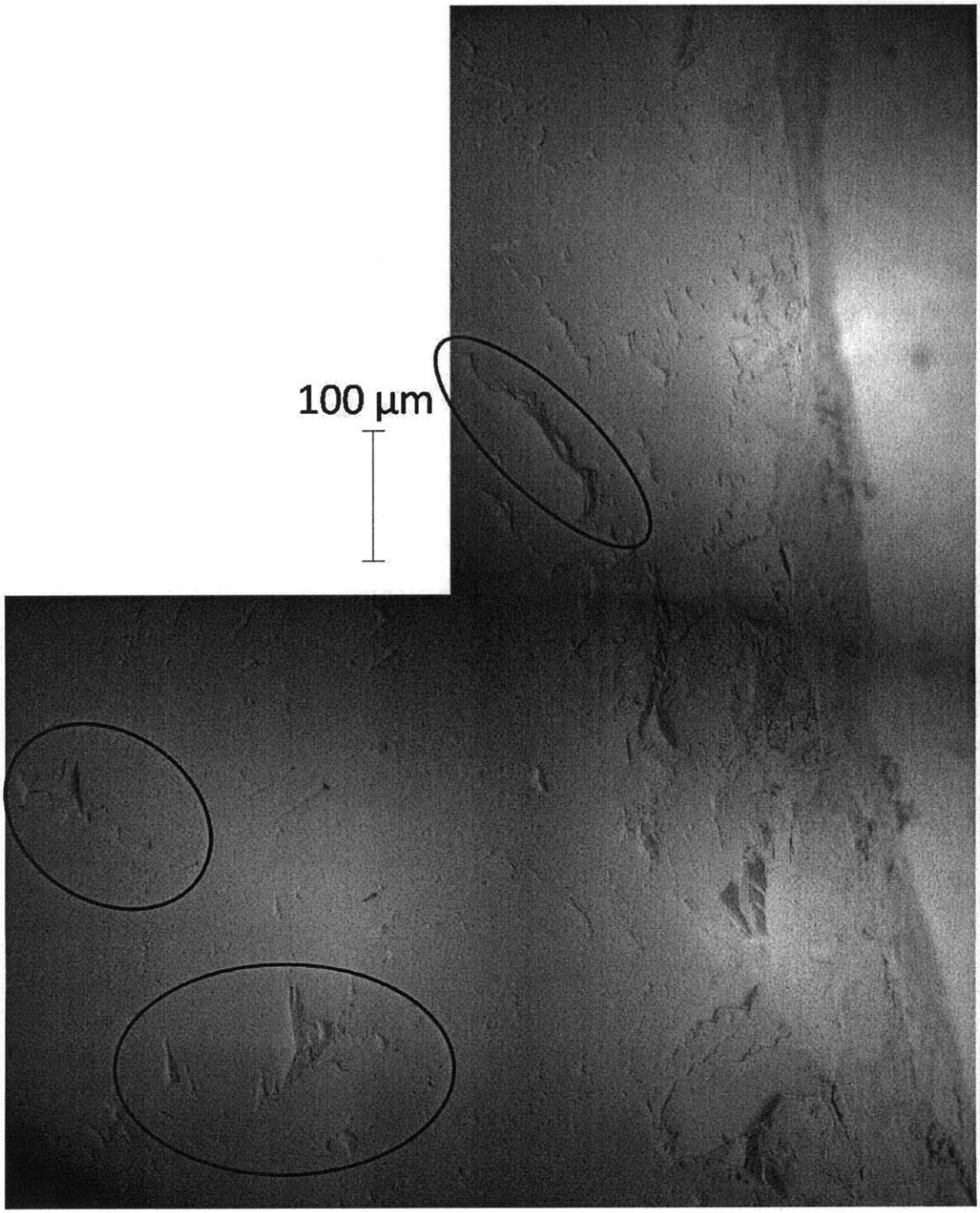

Figure 4-7: Despite surface preparation, some spalling (circled) is visible on Specimen Z1.

in these images. This spotlight effect reflects user error in microscope settings more so than surface structure. The size and brightness of the electron beam, as well as the size of the scanned area for each image, have not been optimized. The higher quality ESEM images in other sections of this chapter display a smaller specimen area in each image, as well as in some cases a less bright beam and a smaller or larger beam; the end result is to remove the darkened regions from the edges of the images.

Tip of White Patching

The white patching shown in the previous section would result in a macro-crack if loading had continued. The tip of the white patching was imaged with ESEM (Figure 4-8), and is shown over three consecutive images (Figures 4-9, 4-10, and 4-11).

This region, despite being far from the tip of the flaw, still exhibits signature process zone identifiers. Closest to Specimens Z1 and Z2 (i.e., top of the red box in Figure 4-8), a large region of spalling is apparent. Shorter microcracks are also visible within and just outside of the spalling region (Figure 4-9 and Figure 4-10) Additionally, a longer and continuous microcrack develops beneath the spalling region (Figure 4-11).

Figures 4-9, 4-10, and 4-11 are collages of multiple individual images. When imaging this region, due to the size of the specimen (the entire Process Zone slab was inserted into the ESEM), the specimen had to be positioned very far from the electron detector. Electrons on the edges of the image are farthest from the detector, and could not always be detected. Thus, the images appear darkest on the edges, an effect termed "Spotlighting". As explained in the Appendix, all three figures were corrected for spotlighting.

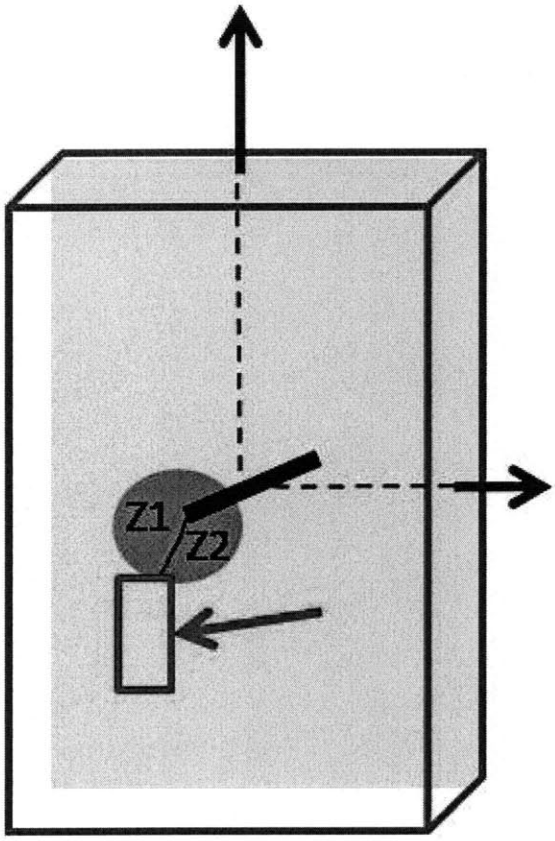

Figure 4-8: Image excerpt; (b) from Figure 3-4. The white patching below Specimens Z1 and Z2, outlined and indicated by an arrow, was imaged with ESEM. The next three figures display the images, and progress consecutively from the top of the red box to the bottom.

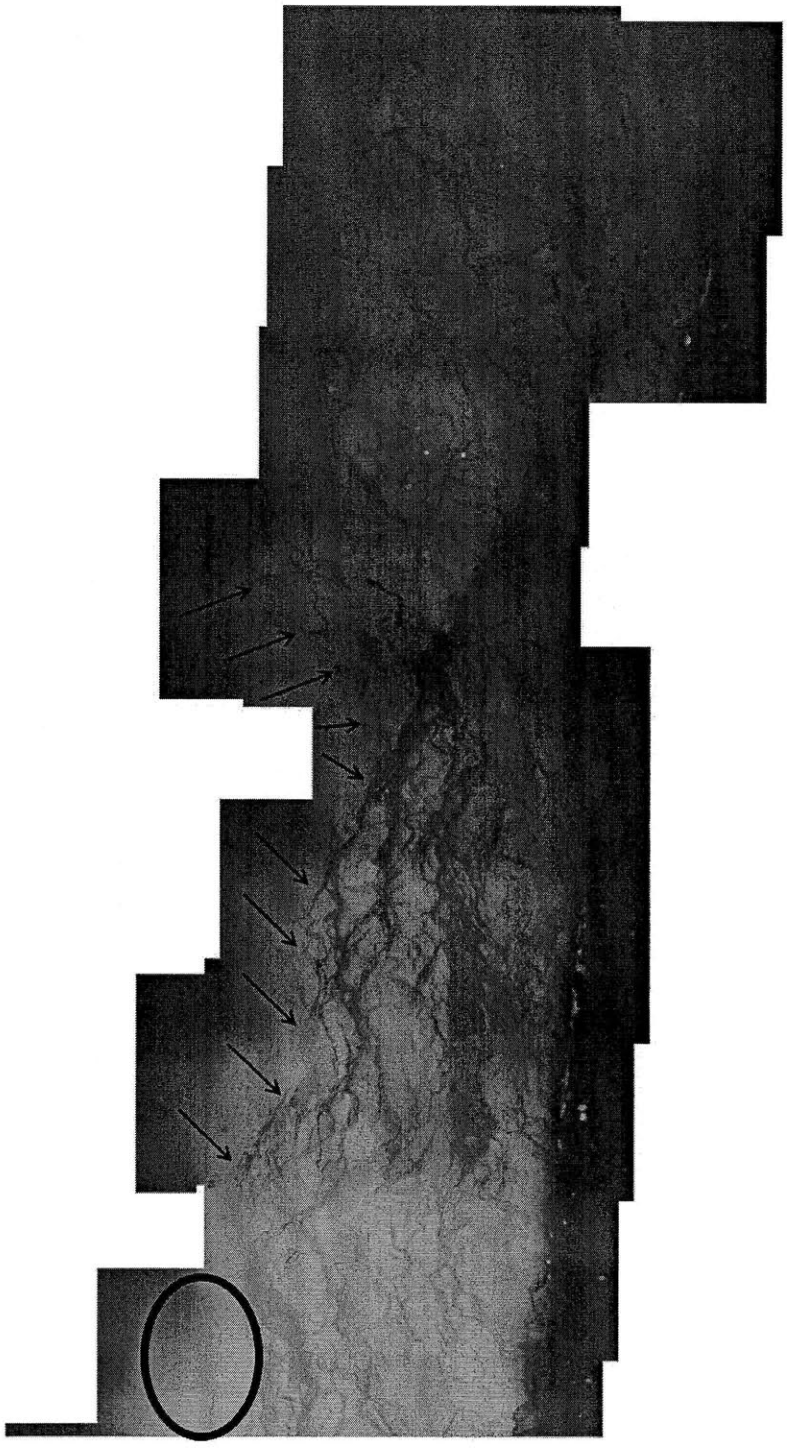

Figure 4-9: Both spalling (indicated by red arrows) and microcracks (red circles) are visible in the white patching region directly below Specimens Z1 and Z2

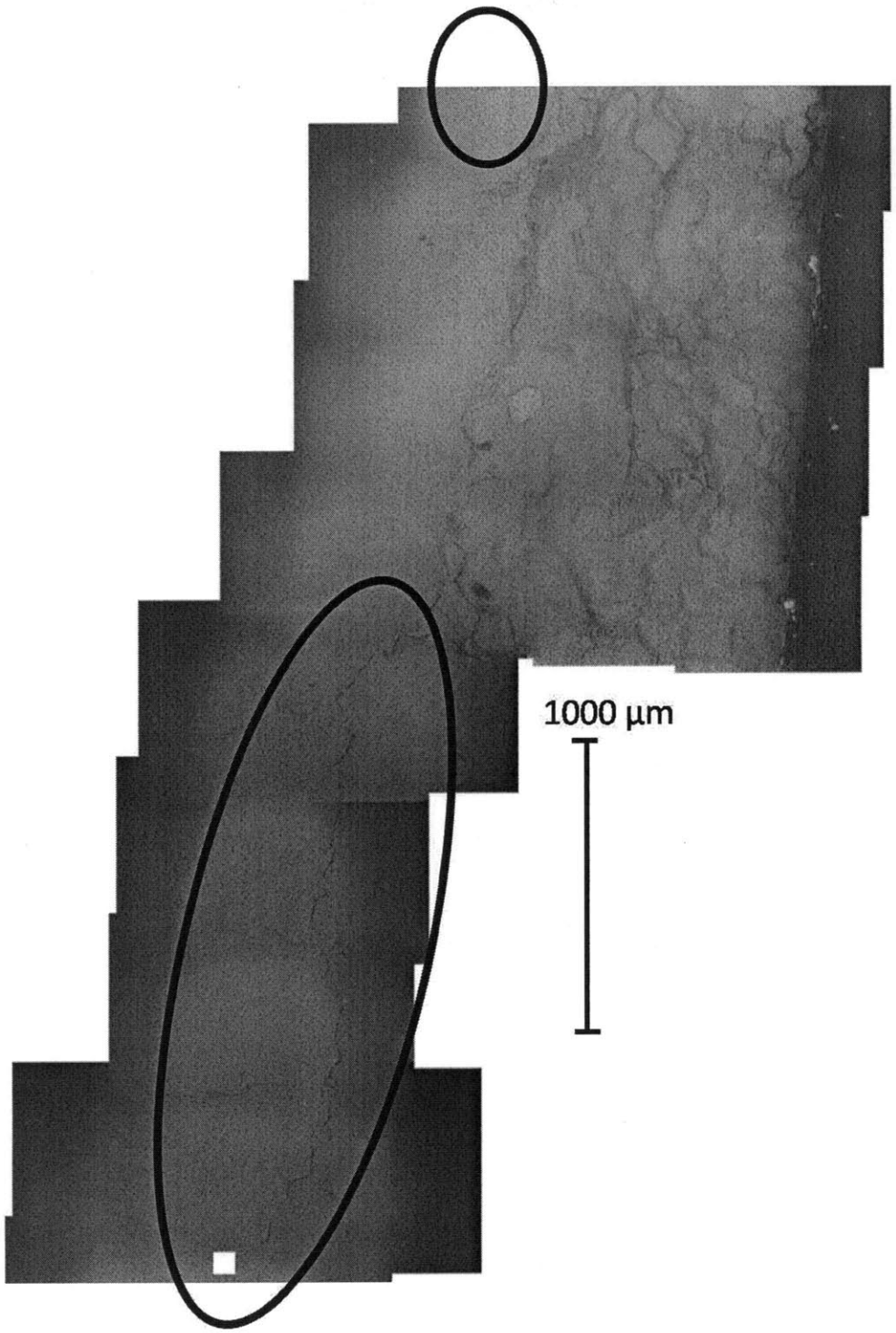

Figure 4-10: Further below Specimens Z1 and Z2, a single continuous and tortuous microcrack becomes apparent (long circle) beneath the region of spalling.

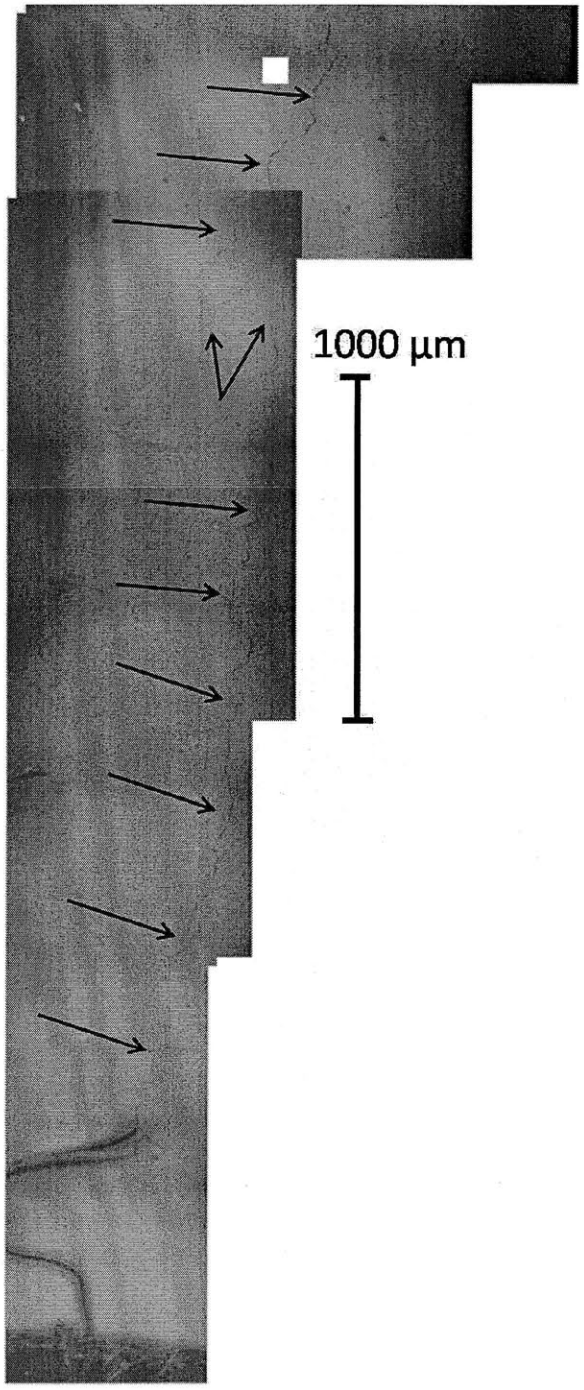

Figure 4-11: Furthest from Specimens Z1 and Z2, no spalling is visible, but a single microcrack decreases in width.

Specimen Y

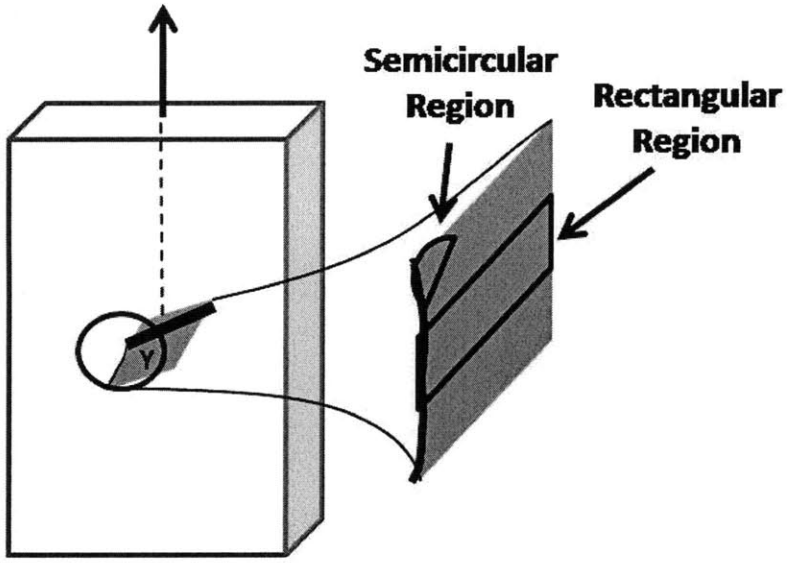

Figure 4-12: Close-up of (e) from Figure 3-4. The regions outlined were imaged by ESEM; the ESEM images are displayed in Figures 4-13 and 4-15.

The triangular corner region of Figure 4-12 revealed a few microcracks (Figure 4-13). However, microscope settings again provided less than optimal imaging. A faulty electron detector coupled with spotlighting (discussed in Section A.2.1) minimized the contrast of microcracks, so fewer microcracks were identified (Figure 4-14).

A new electron detector in conjunction with optimized microscope settings yielded improved images for the rectangular region of Figure 4-12. This exposed surface of the process zone yielded an abundance of process zone microscale features upon observation with ESEM (Figure 4-15).

Again, by not polishing the specimen or preparing the surface, the original crack pattern is preserved. Particular regions of microcracking and debris are indicated in the figure, and are displayed at high magnification (Figures 4-16, 4-17, 4-18, and 4-19). Red arrows in these figures indicate microcracks.

Similar to the microcracking visible in Figure 4-4, at the Y-axis orientation microcracks also propagate through grain boundaries (Figure 4-16). Spalling is visible between the two

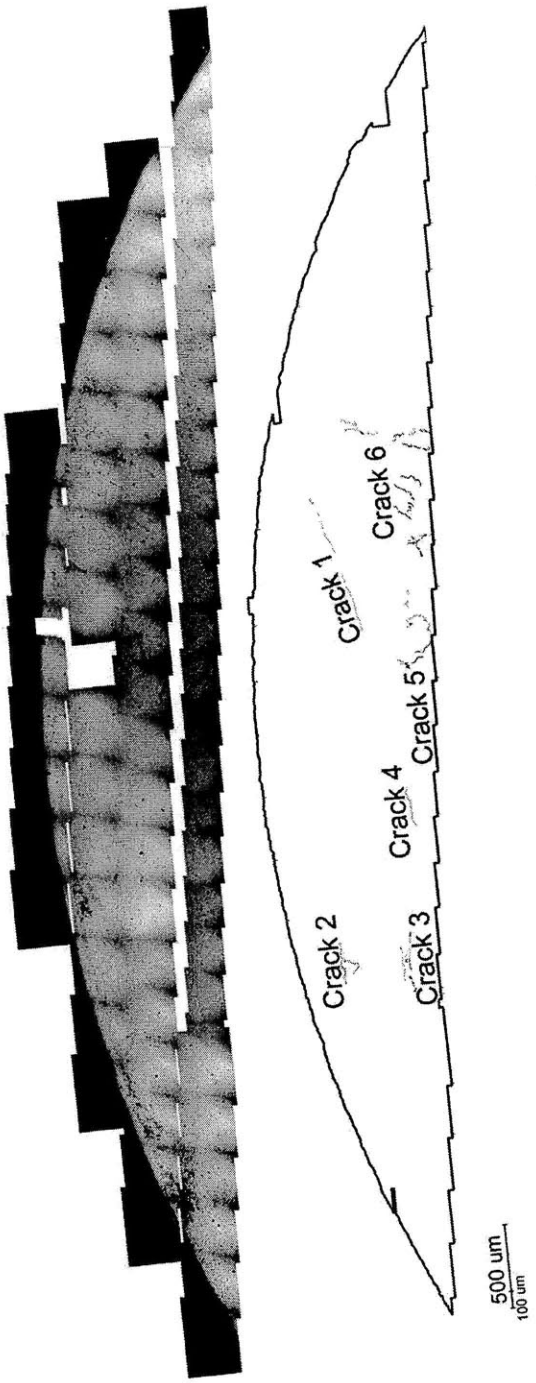

Figure 4-13: Semicircular region from Figure 4-12. A few microcracks are apparent in the corner region of Specimen Y. Detail of Crack 1 and Crack 2 is presented in Figure 4-14.

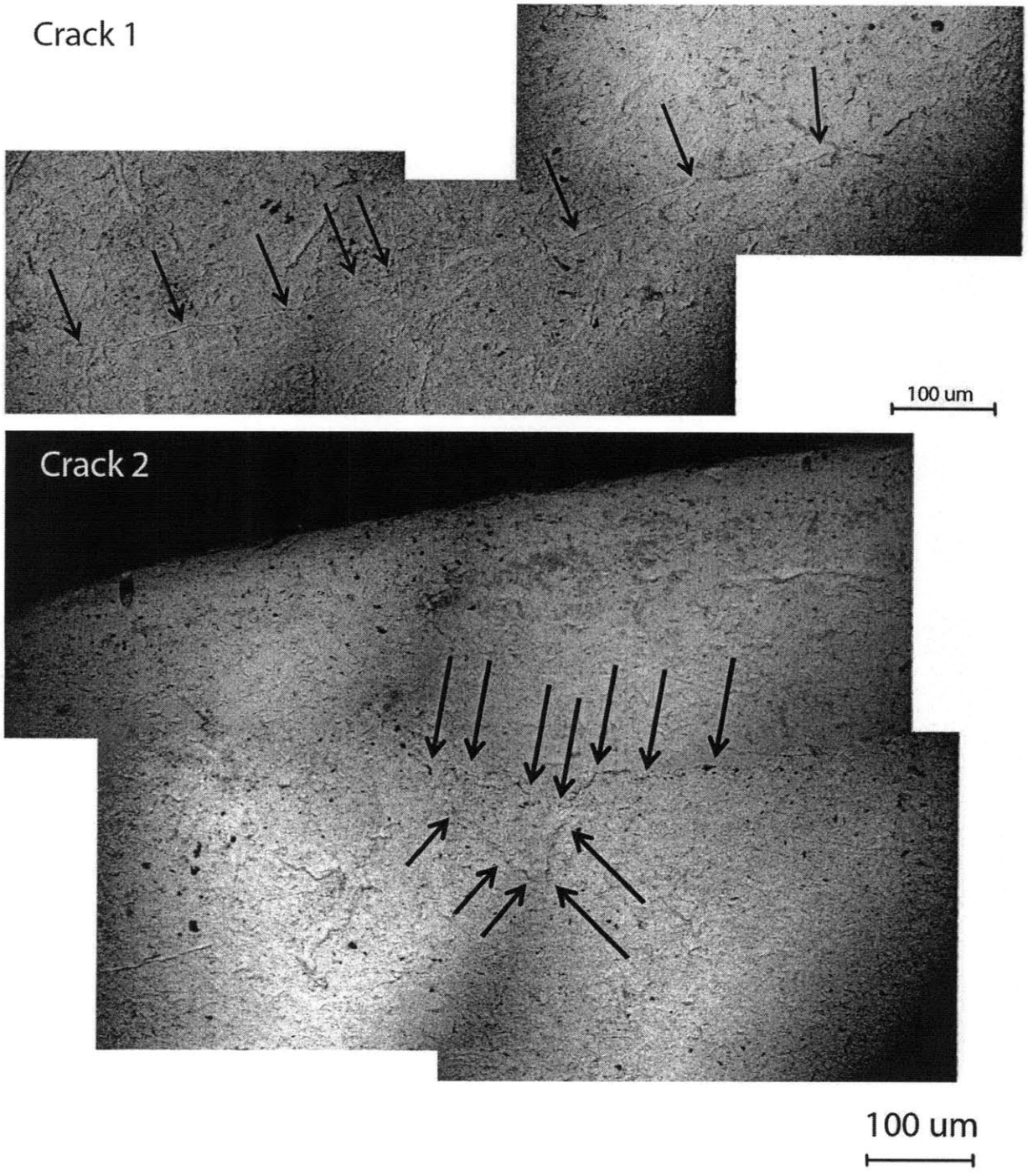

Figure 4-14: Close-up of cracks on Figure 4-13. Detail of the few identifiable microcracks in the semicircular corner region of Specimen Y.

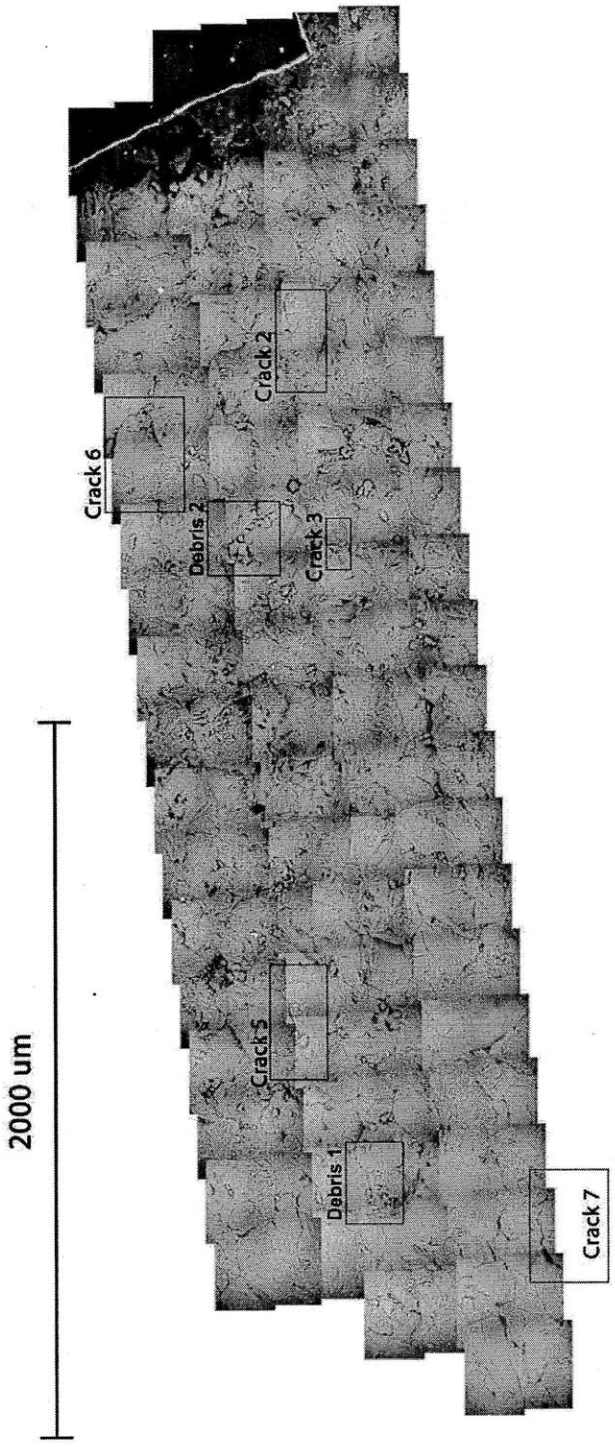

Figure 4-15: Rectangular region of Figure 4-12. Both microcracks and naturally abraded debris are visible in the exposed white patching surface of Specimen Y. Detail of boxed areas is presented in the next figures.

rightmost arrows in Figure 4-16, (a). An additional feature of interest in the image is the texture of the specimen. In Figure 4-16, (b), parallel lines within the marble grain indicate the regular crystalline structure of the material near Crack 6.

Figure 4-17, (a), shows another microcrack, Crack 5, which has propagated around a marble grain. Figure 4-17, (b) also shows a microcrack: Crack 3. However, Crack 3 has an approximate length of less than 50 μm. In comparison with other microcracks (Figures 4-16, 4-17, 4-18), this microcrack has a very short length. Three factors suggest that this crack can be defined as an intragranular crack: i) the short length of this crack, ii) the proximity of other cracks in Figure 4-17, (b), and iii) the typical size of Carrara marble grains (40 to 200 μm, [51]). Rather than surrounding an entire marble grain, the relatively short Crack 5 has most likely cut across a marble grain and can thus be defined as an intragranular crack.

As they propagate along grain boundaries, microcracks interact with marble grains, and in some cases may dislodge them from surrounding material (Figure 4-18). The leftmost edge of the grain surrounded by Crack 7 casts a shadow on the surrounding material, which suggests either that significant spalling has occurred at the edges of the grain, or that the grain has been shifted from its original intact position.

A final feature of interest is the presence of debris in the images, most notable in Figure 4-19. ESEM does not require surface preparation, and thereby allows for the imaging of abraded material on the specimen surface. Abraded material is a defining feature of cracks that open in shear [9]. This material may also contribute to the white appearance of the process zone in marble.

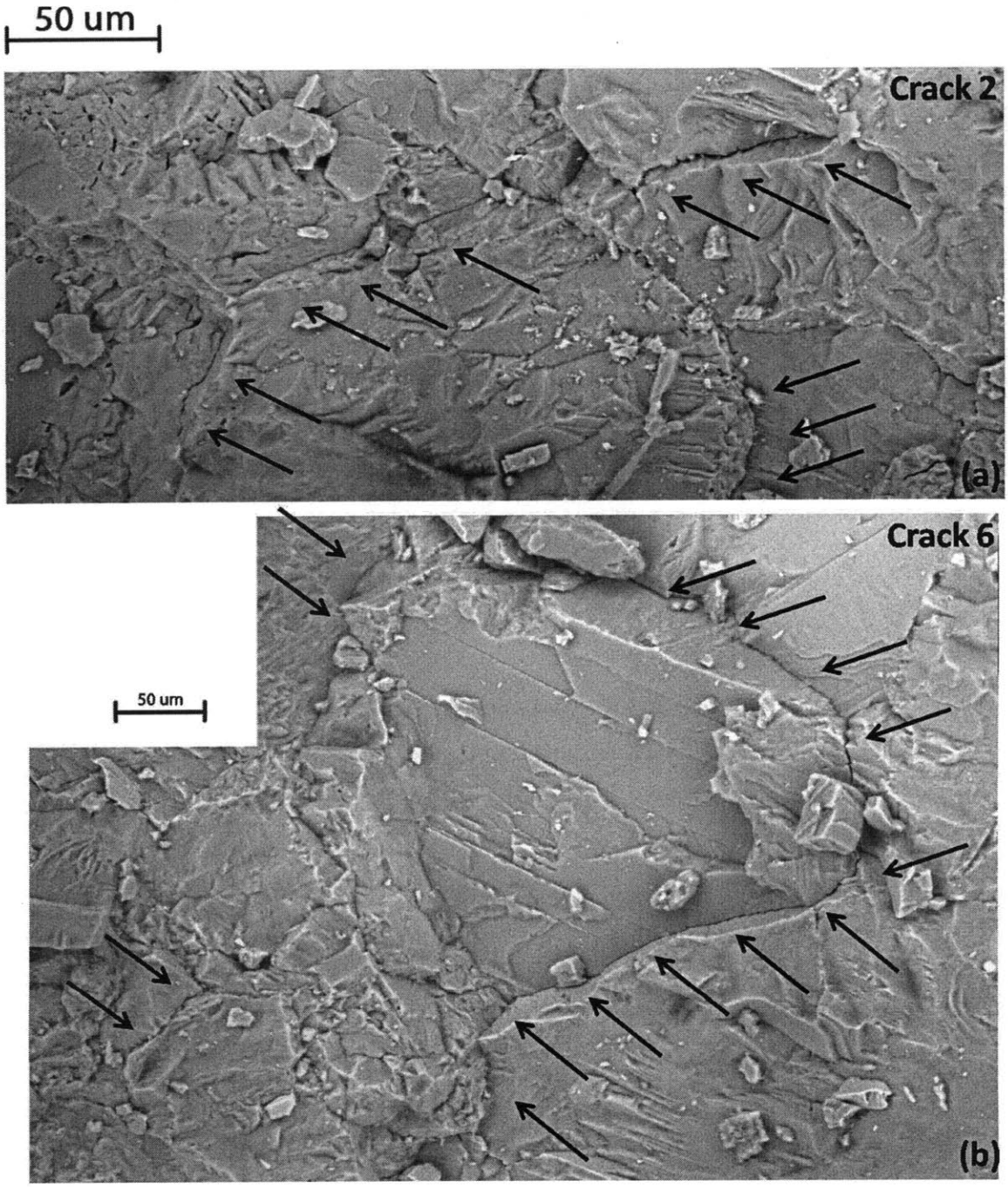

Figure 4-16: Crack 2 (top) and Crack 6 (bottom). Microcracks manifest as a separation along grain boundaries.

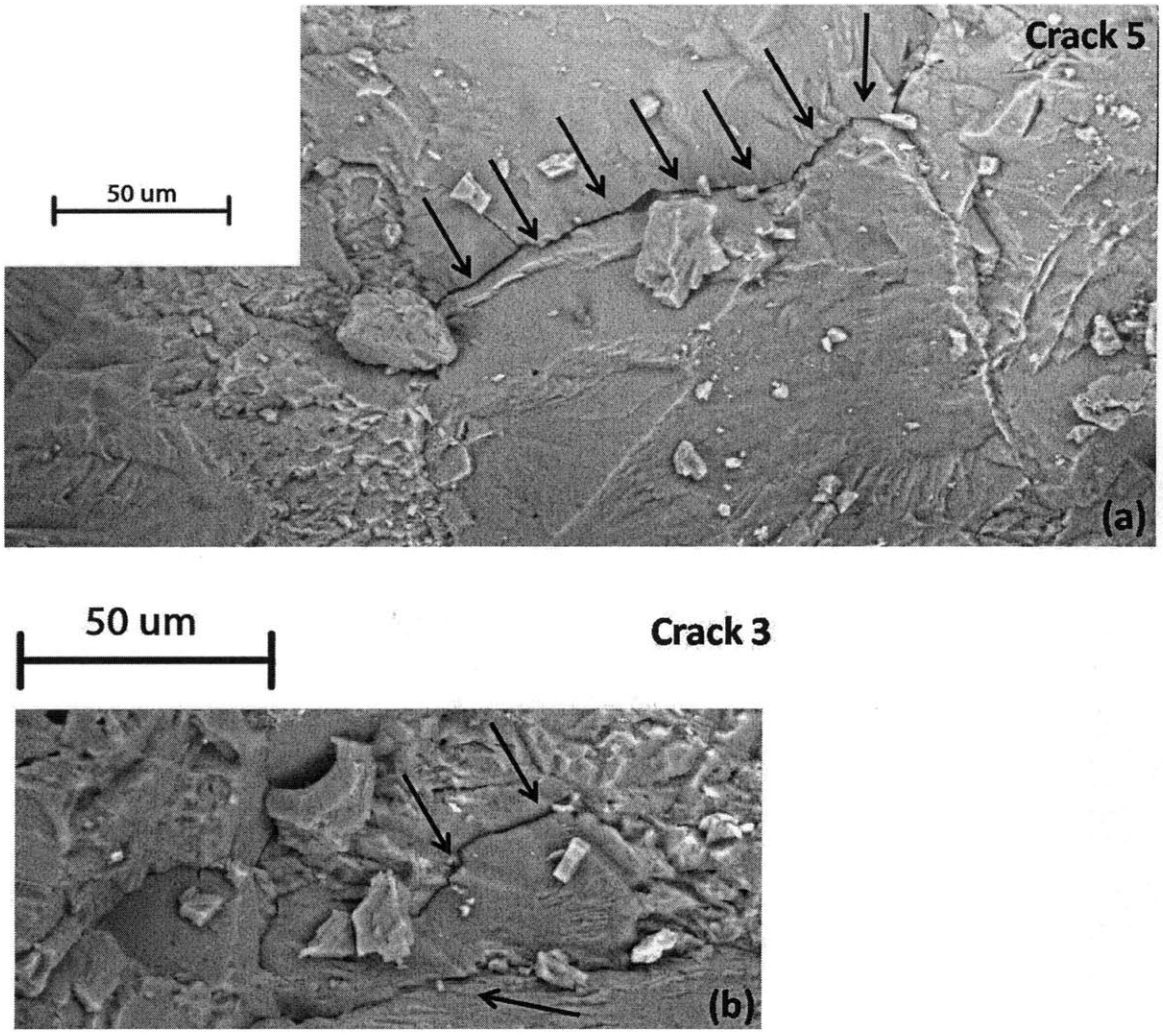

Figure 4-17: (a) Crack 5; (b) Crack 3. As shown particularly in Crack 3, microcracks may propagate within a marble grain.

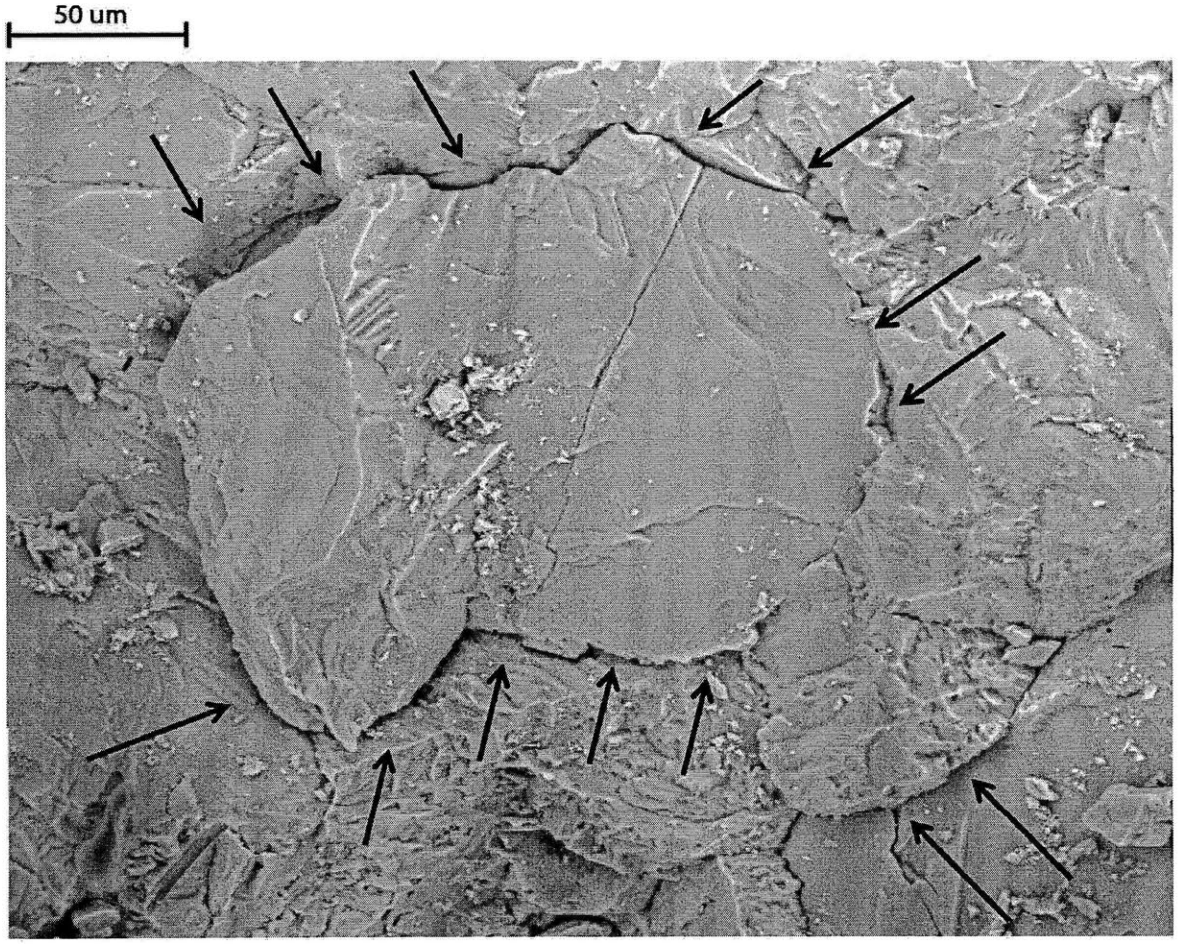

Figure 4-18: Crack 7. Particularly on the left edge, the microcrack appears to have dislodged the central marble grain from surrounding marble grains.

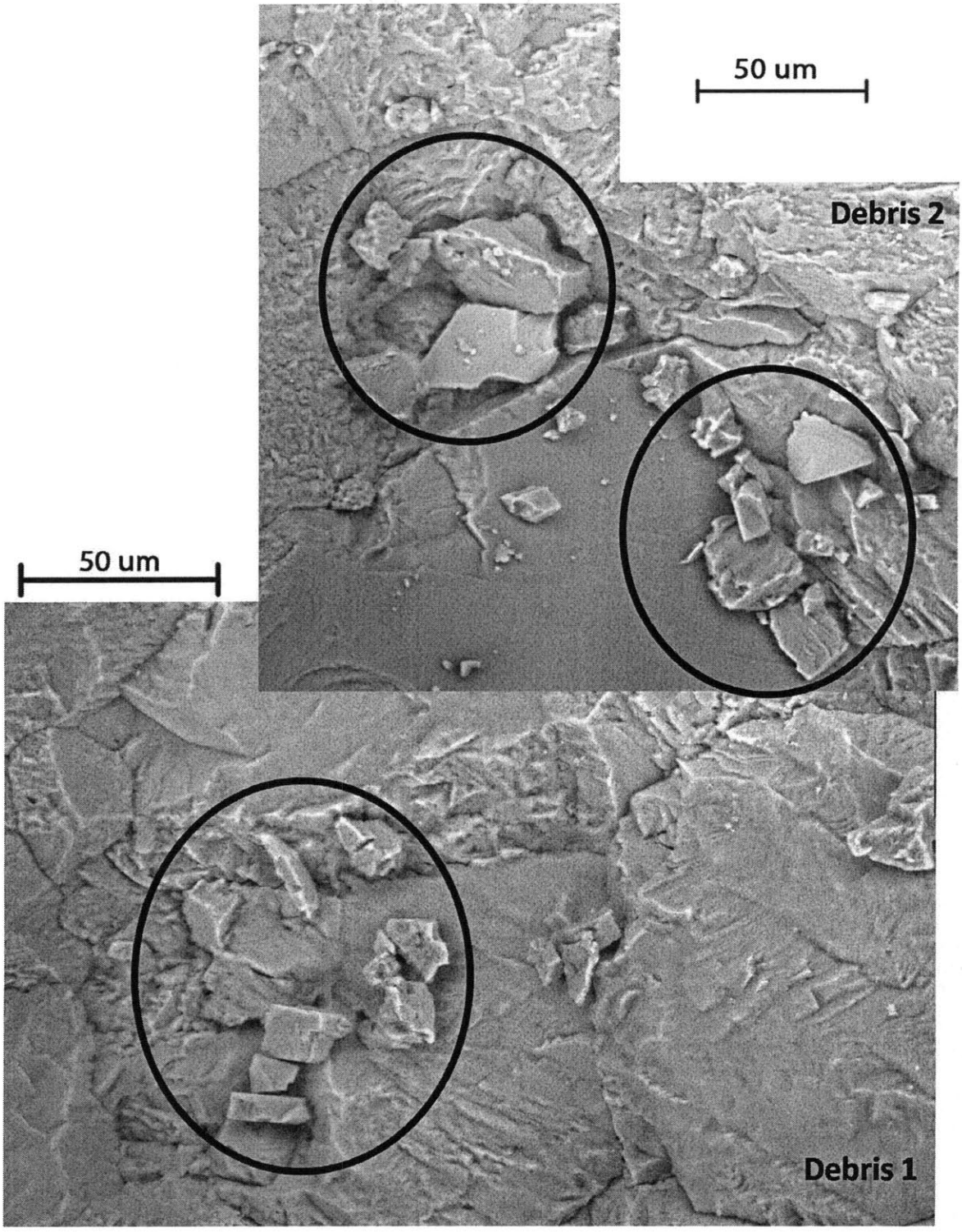

Figure 4-19: ESEM does not require surface preparation and therby allows for the imaging of abraded material on the specimen surface.

Crack Density Analysis

A final analysis assesses the microcrack density of the image of Specimen Y. First, all the microcracks in the original image were traced (Figure 4-20;).

In order to assess the density of microcracking, and relate the level of microcracking with previously established qualitative crack density levels (CDL; length of crack per given area; [73]), the existing qualitative levels were first translated into quantitative levels. This was accomplished by evaluating the crack density of each of the qualitative levels (Figure 4-21 and Table 4.1). This evaluation yielded four maximum crack density levels.

Next, the image of Specimen Y (Figure 4-15) was divided into square regions (100 μm x 100 μm) and the crack density for each region (total length of microcracking in a single square region) was evaluated. Three of the typical microcrack density levels exist in the imaged region (Figure 4-22). Averaged over the entire image, there is an average of 120 μm of crack per 10,000 μm^2 of material, which corresponds to Low CDL. However, particular regions of Medium and Background CDL can be seen in the image. It is hypothesized that further loading of the specimen would have exaggerated the process zone and increased the crack density, potentially yielding regions of High Crack Density as well.

The images and crack density analysis collectively describe process zone microstructure: an abundance of microcracks both around and within marble grains, as well as debris. Crack density under the particular loading conditions generated an average Low CDL within this process zone region. Microcracks and potentially debris contribute to the white appearance of the process zone in marble. The mechanical properties of this region at this scale, the

Qualitative Crack Density Level (CDL)	**Quantitative CDL (Crack Length per 10000 μm^2 of Marble)**
Background	62.3
Low	169
Medium	391
High	630

Table 4.1: In order to assess the density of microcracking, and relate the level of microcracking with previously established qualitative crack density levels (CDL; length of crack per given area, the existing qualitative levels were first translated into quantitative levels. This was accomplished by evaluating the crack density of each of the qualitative levels.

microscale, are explored in the next section.

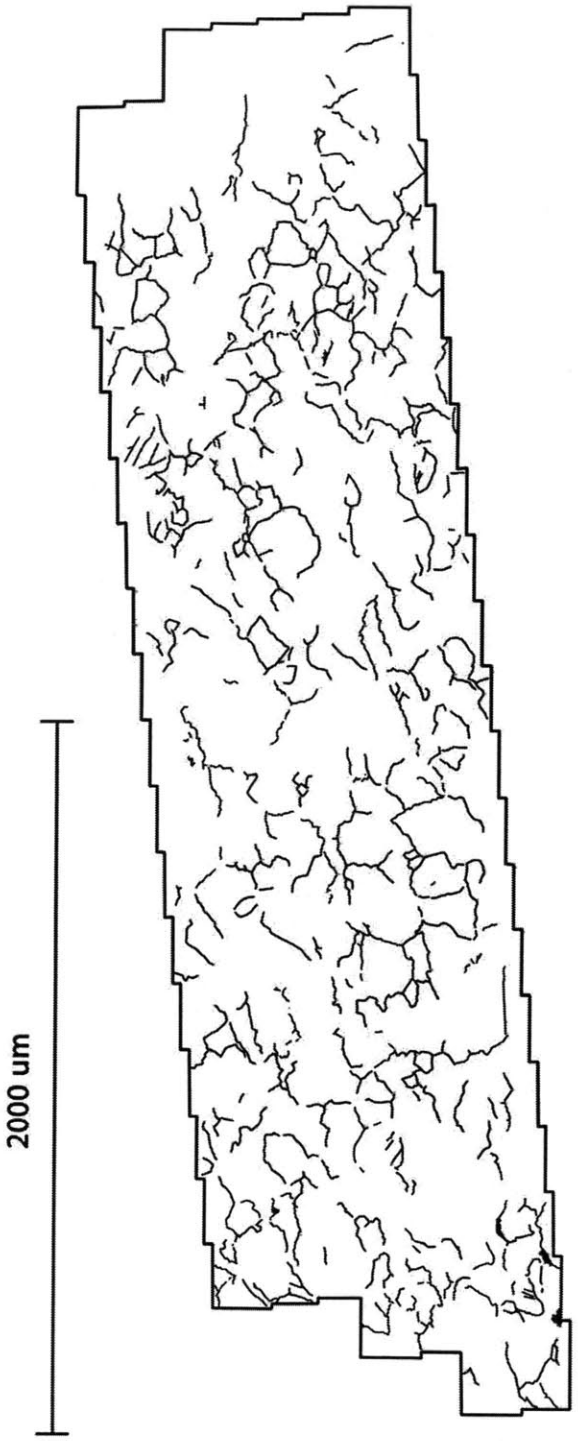

Figure 4-20: Region originally shown in Figure 4-15. Microcracks cover nearly the entire surface of the region imaged on Specimen Y.

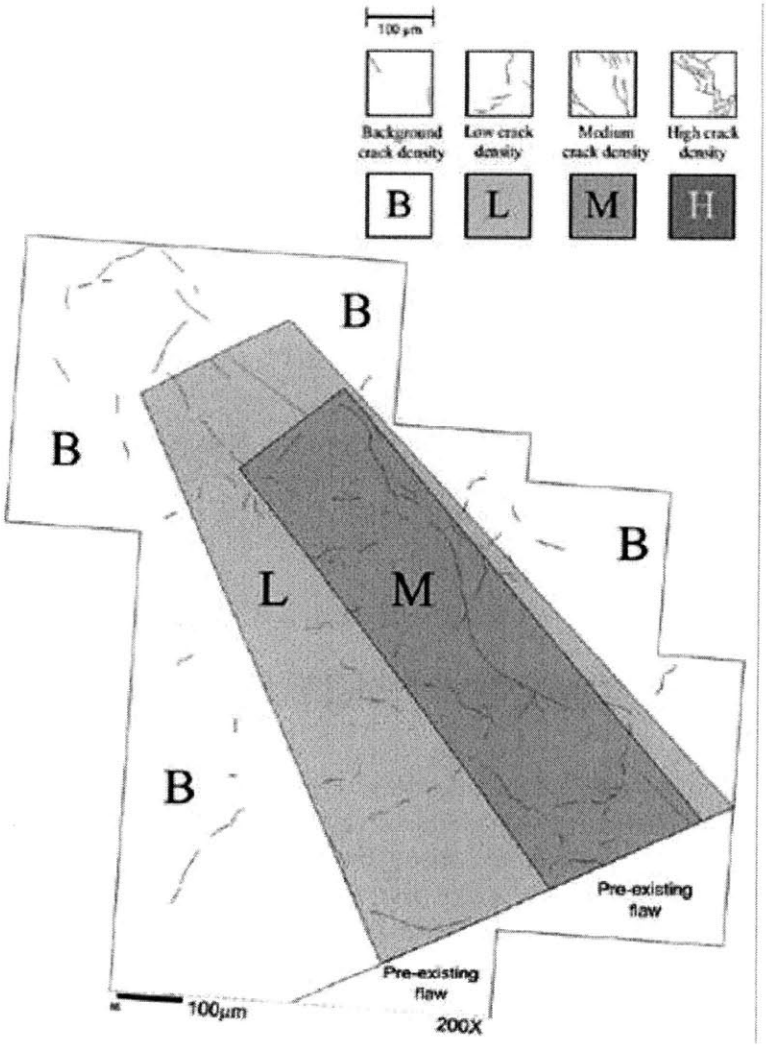

Figure 4-21: Wong established four qualitative levels of microcrack density by visual observation and a relative assessment of the frequence of microcracking [Wong 2008].

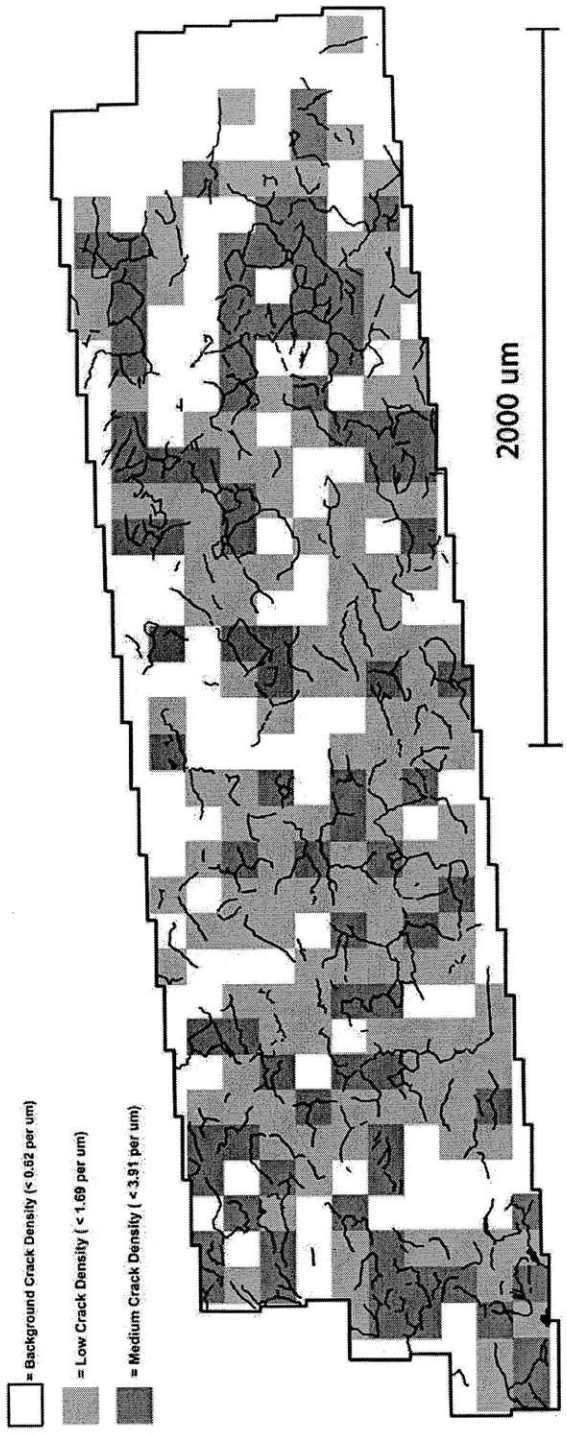

Figure 4-22: Three of Wong's microcracking densities are found on Specimen Y: Background (no color), Low (light gray), and Medium (dark gray).

4.2 Nanoindentation Results

This section details the test results and analytical tools which reveal trends in nanomechanical properties, and compares these trends with the results of a previous study on the crack tip process zone in marble.The second tool used to probe the crack tip process zone is the measurement of differences in nanomechanical properties between intact and process zone materials. Trends and variation of nanomechanical properties over extensive areas are crucial components of this investigation.

One trend in particular characterizes the results of all nanoindentation testing: as shown below, marble exhibits a lower indentation modulus and hardness in and near the crack tip process zone when compared with the typical indentation modulus and hardness of intact material.

4.2.1 Nanoindentation Data

In this study, a nanoindentation "test" consists of several hundred nanoindentations over an area. Typically, each line consisted of 300+ individual nanoindentations; a total of 4,732 indentations inform the results presented in this section. The nanoindentation tests were conducted on the two material types which govern this investigation: intact material, and process zone material. For both material types, anisotropy was explored by conducting tests on differently oriented surfaces of material (Figure 4-23). As detailed in Sections 4.2.3 and 4.2.4, on the surfaces of the material in the process zone, two to three nanoindentation tests were conducted progressively closer to the process zone as a means of exploring the trends in micromechanical properties near the process zone.

Nanoindentation data are presented in box plot form (Figure 4-24). A box plot provides a first-order means of data analysis for this investigation because it presents a concise summary of the spread and typical values of each nanoindentation test. The bottom and top of the whiskers correspond to the average nanoindentation value (either modulus or hardness), respectively minus and plus one standard deviation. The central value corresponds to the median value, and the bottom and top of the box correspond to the 25th and 75th percentile of the data. Median expresses the typical value from hundreds of nanoindentations without being susceptible

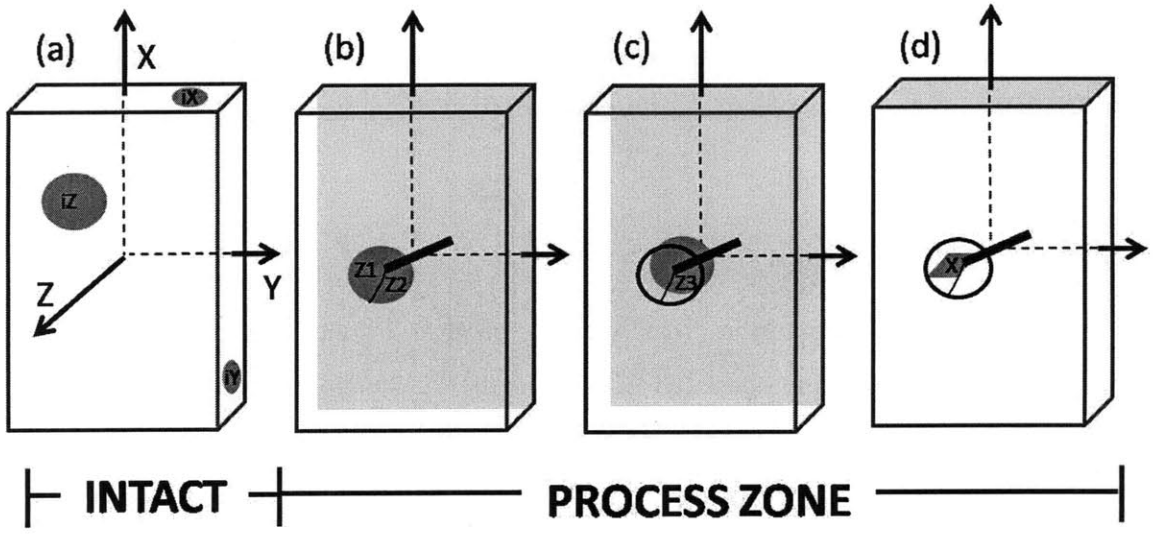

Figure 4-23: Excerpt from Figure 4.0.1. Dark gray regions indicate cylindrical cores containing surfaces on which nanoindentation testing was performed. (a) "Intact" Specimen, testing surfaces normal to X, Y, and Z, (b) "Process Zone" Specimen, testing surface normal to Z (i.e., parallel to top surface of cylindrical specimen) (c) "Process Zone" Specimen, testing surface within slab normal to Z (i.e., parallel to top surface of cylindrical specimen) (d) "Process Zone" Specimen, testing surface normal to X (i.e., parallel to long axis of cylindrical specimen).

to outlier values, in the way that mean is susceptible. Note that for normally distributed data sets, approximately 25% of the data can be found between the mean and the 25th or 75th percentile. The closeness of the ends of the box (25th/75th percentile) to the ends of the whiskers (average +/- one standard deviation) indicates the spread of the data. Data sets with little spread will have larger boxes, and smaller distances from box to whiskers; data sets with more spread will have larger boxes, and greater distances from box to whiskers. The box plot thus presents a concise summary of the spread and typical values of the data from each nanoindentation test series.

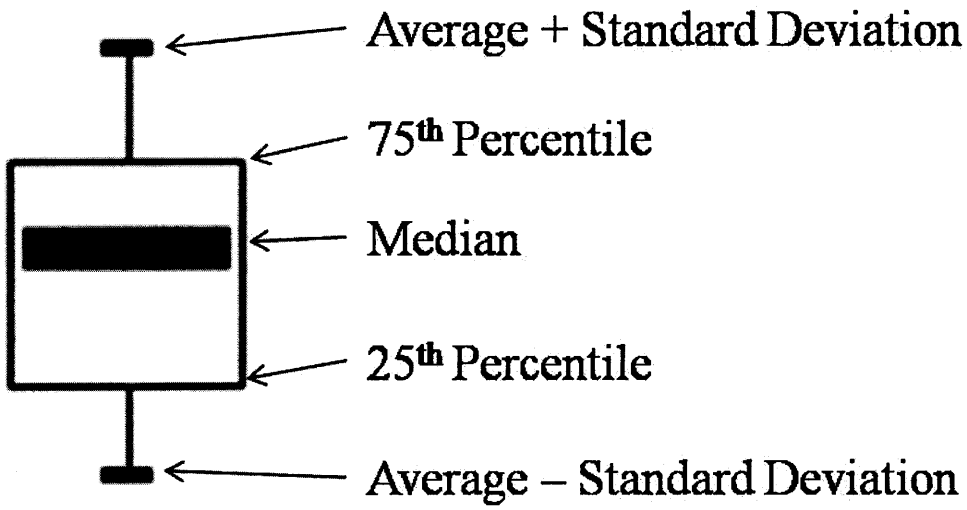

Figure 4-24: A box plot succintly captures the spread and typical value of a test comprised of many individual nanoindentations.

4.2.2 Weak Anisotropy of Intact Marble

In order to check for possible anisotropy, 478 nanoindentations were conducted on three orthogonal faces of the Intact Specimen. Inspection of the nanoindentation results (Figure 4-25) reveals a higher modulus and hardness (73.52 GPa modulus, and 2.98 GPa hardness) on the Z-face (i.e., the face to which the Z-axis is normal) compared to the other two faces (Y-face: 68.8 GPa modulus and 2.78 GPa hardness; X-face: 68.8 GPa modulus and 2.90 GPa hardness). Note also the larger spread of moduli (larger box size) on the Z-face compared to the other two

Surface	Modulus(GPa)	Standard Deviation (GPa)
X	68.8	4.35
Y	67.33	3.82
Z	73.52	5.49

Table 4.2: Median and standard deviation of modulus of intact marble. There is a higher modulus and hardness on the Z-face (i.e., the face to which the Z-axis is normal) compared to the other two faces.

Surface	Hardness(GPa)	Standard Deviation (GPa)
X	2.90	0.17
Y	2.78	0.17
Z	2.98	0.12

Table 4.3: Median and standard deviation of hardness of intact marble. There is a higher modulus and hardness on the Z-face (i.e., the face to which the Z-axis is normal) compared to the other two faces.

faces (Tables 4.2 and 4.3).

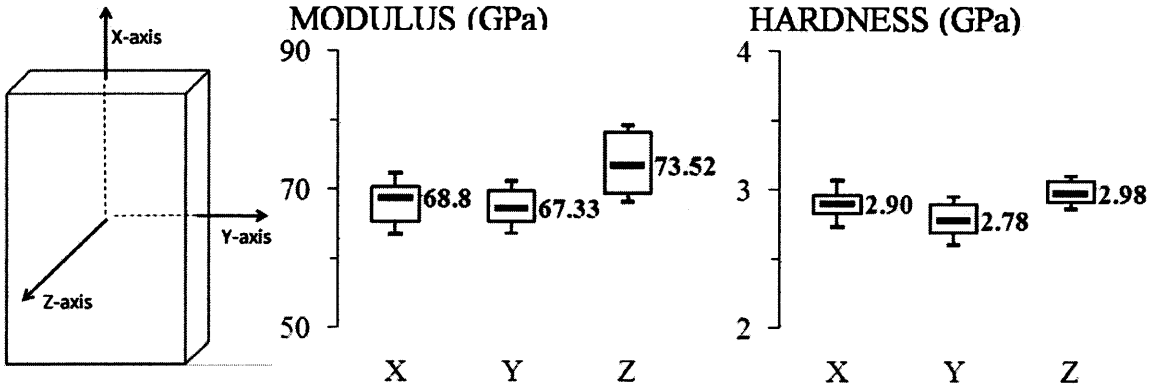

Figure 4-25: Indentations corresponding to the Z-axis reveal a slightly higher modulus and hardness.

The differences in the median modulus and hardness between the Z-face and the other two faces (X-face, Y-face) suggest a slight pre-existing anisotropy of the intact material. However, the Z-face also exhibits a higher spread (standard deviation) of data for modulus values. Thus, the potential for anisotropy may be overshadowed by the exisitng local variation (i.e., standard deviation) in properties. This slight pre-existing anisotropy will be considered when process zone results are presented and compared.

4.2.3 Decreased Modulus and Hardness at Grain Boundaries

Grid nanoindentation testing of intact marble (an intact region of the Process Zone specimen) reveals lower hardness and modulus values near the boundaries of marble grains. A comparison of a spatial plot of modulus values, a spatial plot of hardness values, and an optical microscopy image illustrates this finding (Figure 4-26). The color of each square in the pixel plot corresponds to a particular modulus or hardness value; the highest values are red (90 GPa modulus, and 4.5 GPa hardness), and the lowest values are dark blue (50 GPa modulus, and 1.5 GPa hardness).

Both plots contain a dark blue line-shaped region in the lower left corner of the plot. This region corresponds to the grain boundary in the lower left corner of the optical image. Note that in the modulus plot, the dark blue line-shaped region is bounded above by a lighter blue line, above that by a light green line, and still above that by a yellow region. Thus, while both plots indicate the grain boundary with a region of low (dark blue) modulus/hardness values, the Modulus plot indicates a gradient (light blue, light green, yellow) of values near the boundary. This is most likely due to the fact that the material response sampled by the elastic unloading involves a larger volume than the one responsible for the strength-hardness behavior (Section 2.1.4, Figure 2-6; [70][44]). Modulus values reflect the behavior of a larger volume of material; that larger volume (and thus the modulus) can contain a grain boundary from a greater distance than the smaller volume associated with hardness values, which reflect the behavior of a smaller volume of material.

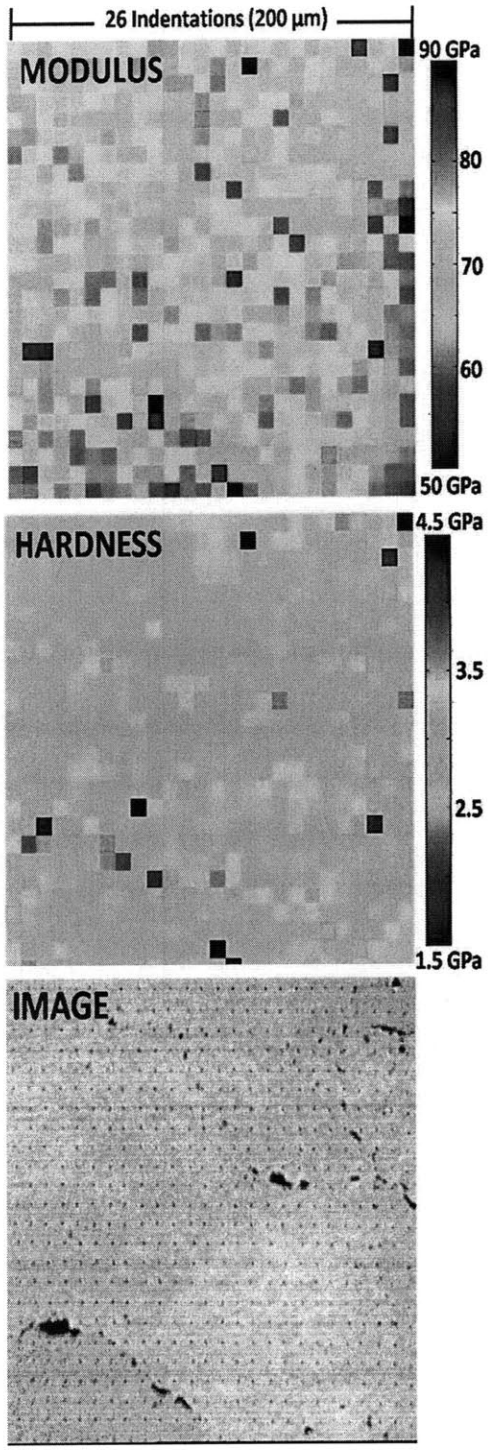

Figure 4-26: A comparison of a spatial plot of indentation modulus values, indentation hardness values, and an optical image of the region reveals lower modulus and hardness near grain boundaries of intact material.

4.2.4 Decreased Modulus and Hardness Near Process Zone

Line nanoindentation testing reveals lower modulus values near and within the process zone. Three lines of 300+ nanoindentations each were conducted progressively closer to the process zone on four specimens: Surfaces Z1, Z2, and Z3 contain a tested surface with a z-axis normal, and Surface X a surface with an x-axis normal.

Surface Z1 is a half-circular shaped specimen, and the process zone lies on the rightmost edge (Figures 3-4, 4-27). Proceeding from left to right towards the process zone, the boxplots drop from a typical indentation modulus of 72.96 GPa farthest from the process zone, to 67.74 GPa closest to it. Hardness also drops from left to right, with a typical indentation hardness of 3.36 GPa farthest from the process zone, to 2.73 GPa closest to it.

Surface Z2 is a quarter-circular shaped specimen, and lies on the opposite side of the process zone from Specimen Z1 (Figures 3-4, 4-28). Proceeding from right to left towards the process zone, no significant or steady decrease in either micromechanical property is apparent on this surface. The modulus values peak slightly in the center of the specimen at 72.73 GPa. This modulus value is just below the typical modulus of intact material on the Z-face (73.52 GPa; (a) of Figure 4-23; MODULUS plot of Figure 4-25). The hardnesses are relatively steady around 2.87 GPa, which is also just below the typical hardness value of the Z-face (2.98 GPa, Figure 4-25).

Surface Z3 is a quarter-circular shaped specimen, and lies at depth in the slab (i.e., parallel to and approximately one centimeter behind Specimen Z2; Figures , 4-29). Similar to Specimen Z2, no significant or steady decrease in either micromechanical property is apparent on this specimen. The typical modulus values (67.5 GPa, Figure 4-29) lie below the typical moduli of Surface Z2 (70.14 GPa, Figure 4-28), and also lie below the typical modulus of intact material on the Z-face (73.52 GPa; Figure 4-25). The hardnesses are also relatively steady around 2.7 GPa (Figure 4-29), which lie below the hardness values of Surface Z2 (2.87 GPa, Figure 4-28), and also below the typical hardness value of the Z-face (2.98 GPa, Figure 4-25).

Surface X (Figure 4-30) also shows a downward trend. The surface exhibits a typical indentation modulus of 71.8 GPa farthest from the process zone, and 68.76 GPa closest to it. The hardnesses are relatively steady, with a typical indentation hardness of 2.65 GPa farthest from the process zone, and 2.75 GPA closest to it.

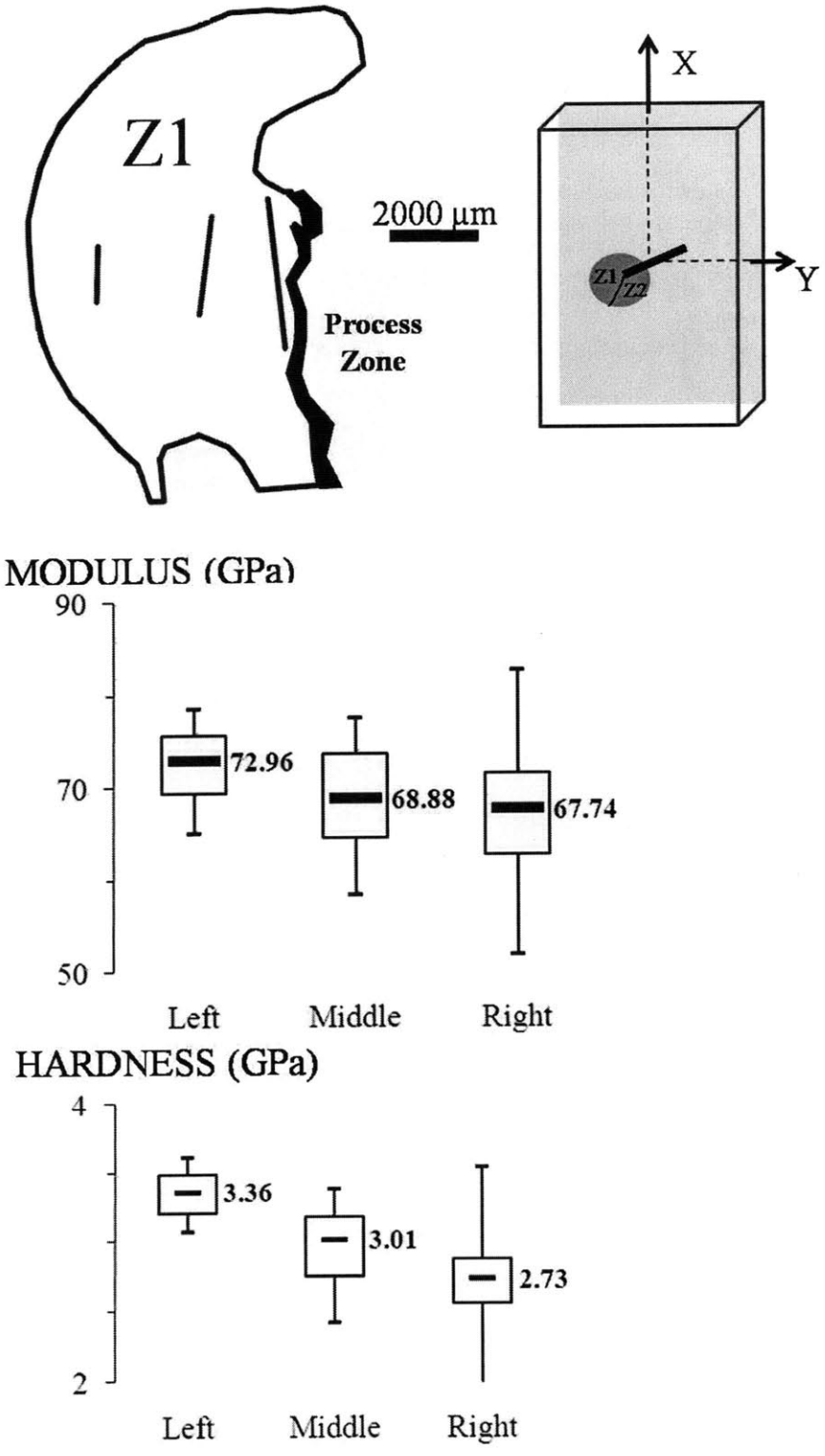

Figure 4-27: The results of line nanoindentation testing on the Z1 Surface.

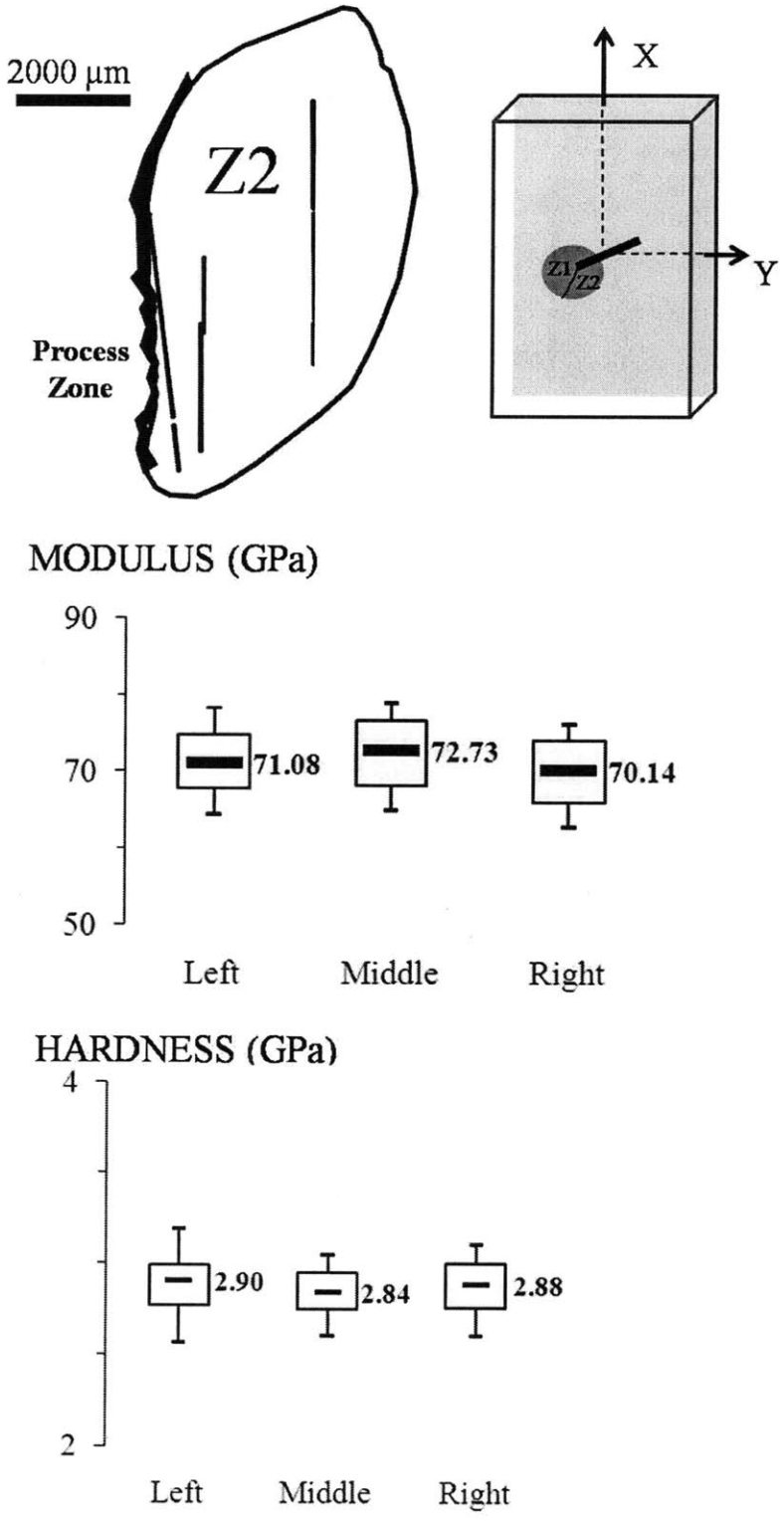

Figure 4-28: The results of line nanoindentation testing on the Z2 Surface.

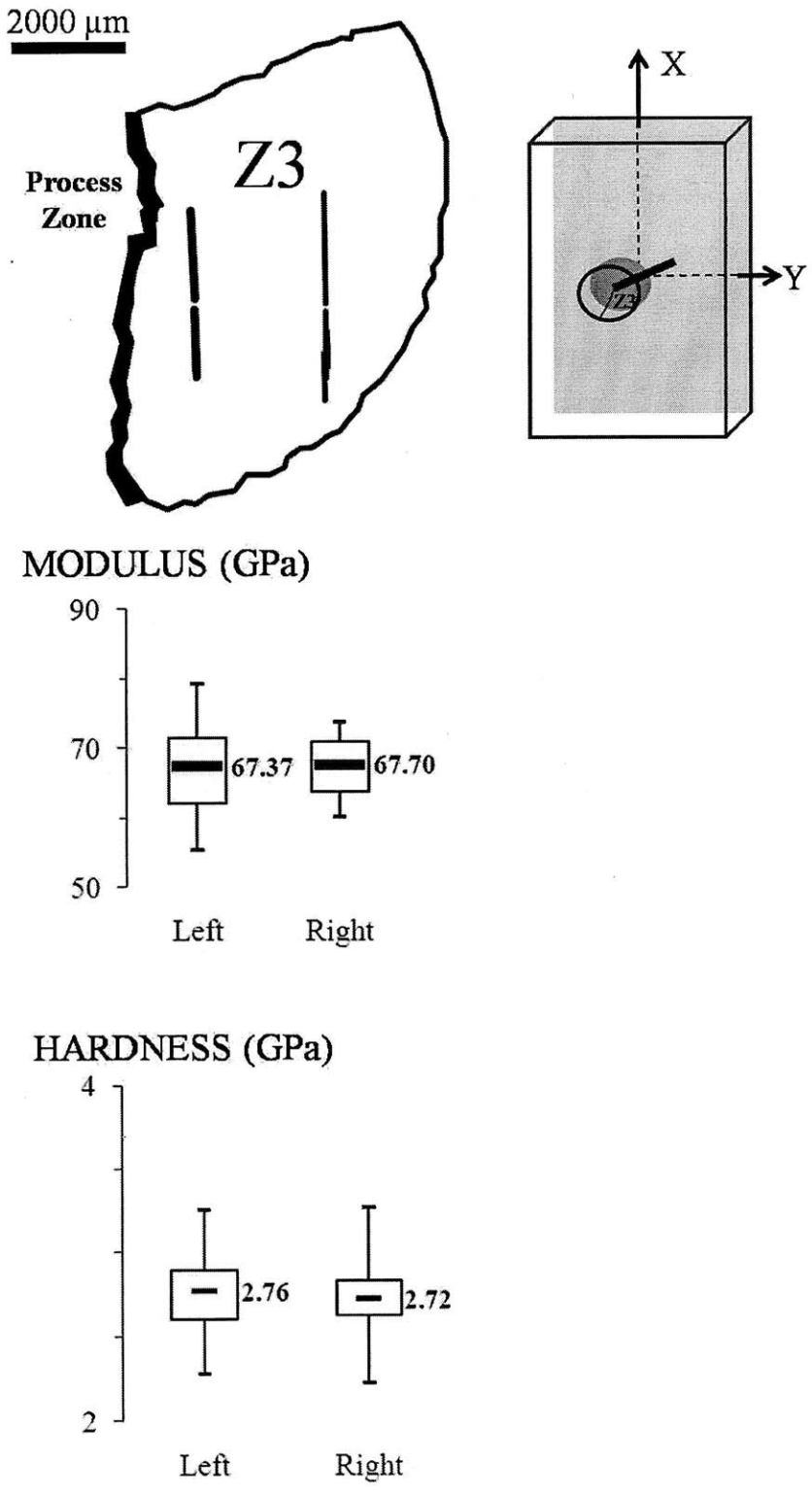

Figure 4-29: The results of line nanoindentation testing on the Z3 Surface.

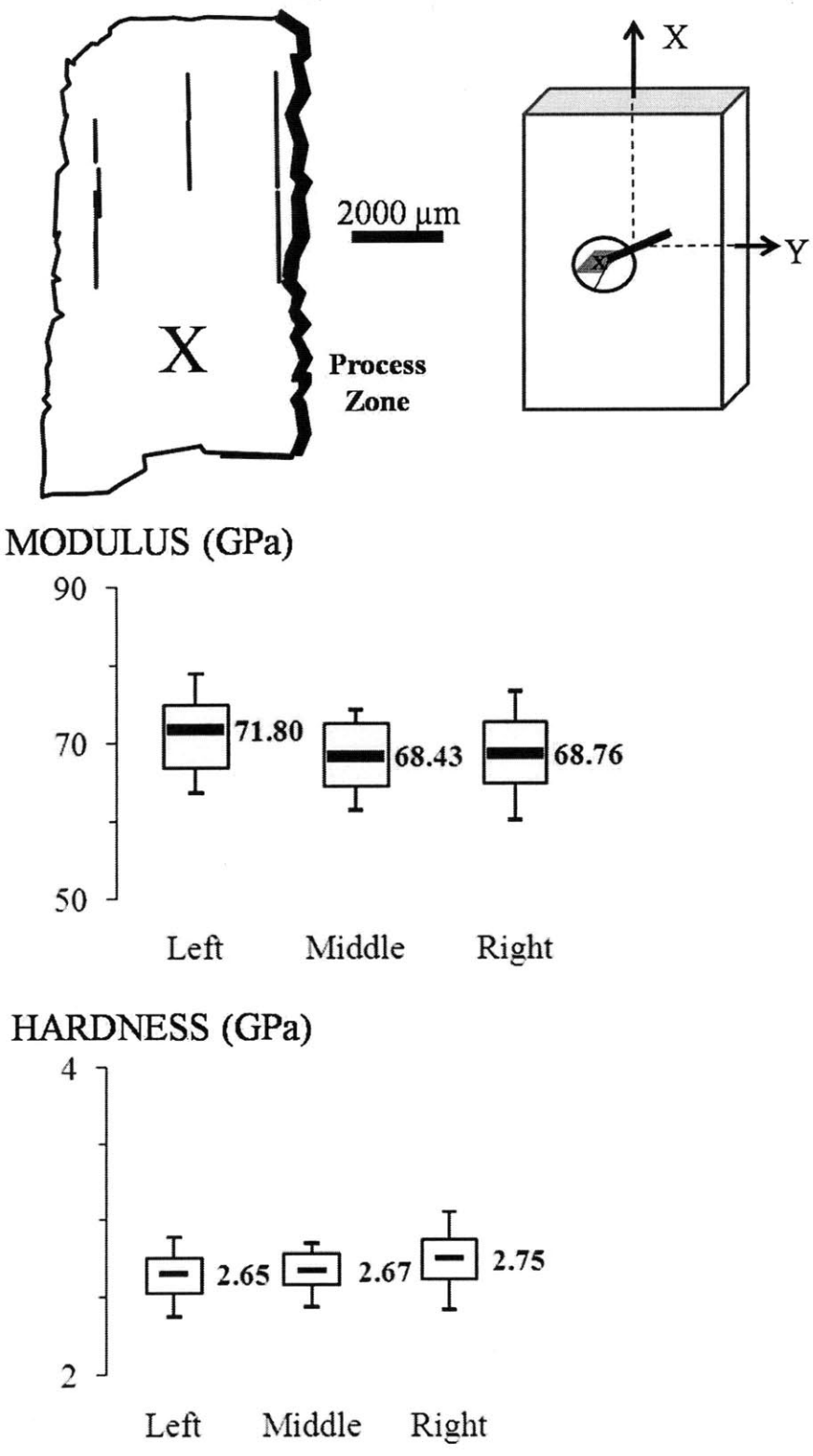

Figure 4-30: The results of line nanoindentation testing on the X Surface.

4.3 Chapter Summary

This study explores the interaction between crack initiation and nanomechanical properties in the crack tip process zone (zone of microcracking at the tip of a propagating crack) of a brittle geomaterial. Samples of Carrara marble with pre-existing cracks ("flaws") were loaded in a uniaxial testing machine until the process zone appeared at the tips of the pre-existing cracks in the form of "white patching". Three techniques were then used to obtain nanomechanical properties of the process zone and relate them to macroscale crack initiation:

Digital Photography, to visually assess the macrostructure and crack formation,

ESEM, to visually assess microstructure, and

Nanoindentation, to yield nanomechanical properties and assess nano/microheterogeneities.

The techniques explored intact and process zone material at various orienations, as indicated in Figure 3-4.

The investigation used ESEM to assess the microstructure of both intact and process zone material. Two types of ESEM images revealed information: individual images, and collaged images (for more explanation, see Appendix A). Individual ESEM images provided a high-resolution interpretation of microstructural features in their most natural state. Collaged ESEM images assessed the relative locations and distributions of the microstructural features at a slightly larger scale. ESEM was validated as an effective tool to probe process zone microstructure. The lack of sample preparation allowed for the observation of the three characteristic process zone microstructural features in their most natural state: intergranular microcracks, intragranular microcracks, and spalling. An additional feature, debris, was also captured in the images. The ESEM investigation also quantified the four established [73] qualitative Crack Density Levels of microcracks by interpreting and assigining particular density (i.e. length of crack per area) ranges to each of the qualitative levels.

Nanoindentation testing was comprised of lines and grids of single nanoindentations located both near and far from the process zone. The purpose of nanoindentation testing was to investigate the underlying trend in nanomechanical property change between intact and process zone marble.

Analysis of nanoindentation testing results showed a decrease of both modulus and hardness (a) near grain boundaries in intact material, and (b) with closeness to the process zone, with

some deviation. Ultimately, the study confirms that the crack tip process zone manifests itself as an area of reduced nanoindentation hardness and nanoindentation modulus in marble. The ESEM and nanoindentation findings are analyzed and discussed in the next chapter.

Chapter 5

Analysis and Discussion

This chapter links the presented ESEM and nanoindentation results to the guiding question of the study: *What fundamental micro-mechanism controls the cracking of a brittle material? Does the mechanism drive cracking, retard cracking, or both? What is the precise scale of this micromechanism?* The chapter opens with a comparison of the findings with pre-existing work, then highlights key findings and discusses them. The discussions of the findings both analyze the findings, and tie them back to the research question.

5.1 Comparison with Previous Work

It is necessary and interesting to compare the experimental results with existing information available in the literature. As discussed in Chapter 2, the literature contains extensive information on three defining aspects of the investigation (nanoindentation, process zone, and geomaterials), but this study is the first to combine these elements in such a way (Table 5.1) The ESEM investigation provided a small-scale, accurate depiction of the microfeatures of cracked materials, while the nanoindentation tests provided information on their nanomechanical properties in the form of nanoindentation modulus and nanoindentation hardness. This information provides an experimental supplement to extensive existing work on the macroscale cracking of brittle materials [38][5]. This information provided is also a powerful complement to existing process zone micro- and nanomechanical information on metals and ceramics [68]. Additionally, the study applied and extended established geomaterial nanoinvestigative techniques

	Barenblatt 1959 [5], Irwin 1957 [38]	**Uguz 1996 [68]**	**Bobko 2008 [10]**	**Wong 2008 [73]**	**Current Study**
Geomaterial	Y	Y	N	Y	Y
Process Zone	Y	N	Y	Y	Y
Microstructure	N	Y	Y	Y	Y
Nanomechanical Properties	N	Y/N	Y	N	Y

Table 5.1: Although the topics of geomaterials, process zone, microstructure, and nanomechanical properties have been pursued individually in the literature, this study presents the first occasion to bring all four elements together in such a way.

to cracked (i.e, process zone) geomaterials [10]. The most closely related previous work, that of Wong 2008, provided a solid foundation for the investigation. Ultimately, the investigation enhances the qualitative microstructural process zone assessment conducted by Wong [73] by refining the crack density levels with actual density values, and by also providing information on the material property change in the process zone region at the nanoscale.

5.2 Findings, Analysis, and Discussion

The experimental results provide clues towards aspects of the governing process zone mechanism. In this section, a method of analysis is presented (statistical significance), the results are presented and analyzed, and clues are discussed.

5.2.1 Statistical Signifiance of Results

This section presents the means of identifiying statistically significant differences for this investigation [49][60]. In particular, the t-test provides an effective means of classifying the statistical significance of the results of this investigation. This test considers a particular outcome – for the purposes of this investigation, this outcome is a difference in the mean value of two populations – and determines whether the outcome is attributable to random chance (i.e., the spread of each populations may overlap or lie very close), or to some more important fundamental difference in the populations. The latter option signifies a statistically significant difference between the populations.

The t-test proceeds by forming a null hypothesis and selecting a confidence level α of mistakenly rejecting the null hypothesis. This confidence level is $\alpha = 5\%$ for this investigation; this particular level is common in scientific investigations [10], and provides a reasonable level of confidence (95%) in the results of the statistical analysis. This confidence level also corresponds to a particular t value (t_{student} or $t_{\text{WS}} = 1.6449$ for the large degree of freedom, $N > 100$, of all tests analyzed in this investigation). The t-test then determines the actual t value with a consideration of the parameters of the two populations: count n_1 and n_2, sample spread (standard deviation) s_1 and s_2, and sample mean (average) x_1 and x_2. A test statistic t is calculated as a function of the parameters. In the case when the populations have the same (or very similar) spreads s_1 and s_2, the Student's t-distribution test statistic is determined [49]:

$$s^2_{\text{student}} = \frac{(n_1 - 1)s_1^2 + (n_2 - 1)s_2^2}{n_1 + n_2 - 2} \tag{5.1}$$

$$t_{\text{student}} = \frac{x_1 - x_2}{s_{\text{student}}\sqrt{\frac{1}{n_1} + \frac{1}{n_2}}} \tag{5.2}$$

In addition to having equal variance, the Student's t-distribution test statistic rests on two other assumptions: that the populations are independent, and that the populations are normally distributed. In the case when the populations have very different spreads s_1 and s_2, the Welch-Satterthwaite test statistic is determined [60]:

$$s^2_{\text{WS}} = \left(\frac{s_1}{n_1}\right)^2 + \left(\frac{s_2}{n_2}\right)^2 \tag{5.3}$$

$$t_{\text{WS}} = \frac{x_1 - x_2}{s_{\text{ws}}} \tag{5.4}$$

The null hypothesis is rejected if the magnitude of t_{student} or t_{WS} is much greater than 1.6449. Based on the pre-selected α value of 5%, the "rejection of the null hypothesis" means that there is only a 5% chance that the difference between the two populations is due to random chance, and a 90% chance that a more fundamental, statistically significant difference between the population dominates [49]. As discussed in the next section, either t_{student} and t_{WS} were used in the tests analyzed based on the difference in the spreads of the tests. The statistically significant t values are presented here (Figures 5-1, 5-2, 5-3, and 5-5) for the tests on intact and process zone material, in addition to the t values for Surface Z3 (Figure 5-4), which were not

statistically significant. These t-statistics are discussed in the following parts of this section.

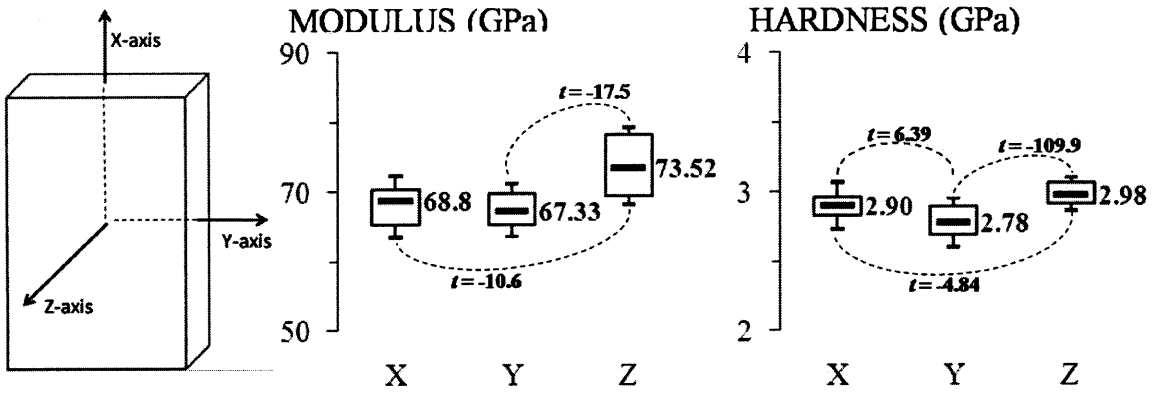

Figure 5-1: Statistically significant ($|t| > 1.664$) Student's t-distribution test statistics for indentation tests on intact material; this statistical analysis enhances data initially presented in Figure 4-25.

Note that Specimen Z3 exhibited no statistically significant t values.

5.2.2 Microstructure of Process Zone

The non-invasive nature of ESEM allowed for extensive imaging of unprepared process zone surfaces. The study verified the existence of typical process zone identifiers (microcracks and spalling) in a minimally disturbed (i.e., unprepared) specimen, and depicted the appearance of these identifiers in such a specimen. Additionally, images of this debris were recorded at high resolution in this study

The microscopy results suggest some interesting conclusions. Firstly, the debris may contribute to the white appearance of the process zone in marble. Debris is an abundant process zone microfeature; its significant presence has a strong likelihood of contributing to the macroscale appearance of the process zone. The second microscopy conclusion relates to the quantified crack density levels (Section 4.1.2): no single crack density governs process zone material. As indicated and quantified in the crack density analysis, a variety of densities may be found in process zone areas. Further analysis beyond the microscopy of the specimen in the current investigation would enhance these conclusions.

Surface	Far (GPa)	Middle (GPa)	Near (GPa)	Decrease Near P.Z.
Z1	3.36	3.01	2.73*	18.8%*
Z2	2.88	2.84	2.90	-0.7%
Z3 (*Z2, at depth)*	2.72	—	2.76	-1.5%
X	2.65	2.67	2.75*	-3.8%*
Average	**2.90**	**2.84**	**2.79**	**3.2%**

Table 5.2: Summary of nanoindentation results (median Hardness values) on Process Zone (P.Z.) specimen surfaces. The test marked with * are compared with intact material values in Section 5.2.4.

5.2.3 Weak Anisotropy of Intact Marble

The surface with a Z-axis normal axis exhibits a slightly higher average indentation hardness and modulus than the surfaces with X- and Y-axis normals. The t-statistics (Figure 5-1) confirm the statistical significance of this difference; the t-statistics when comparing the Z-axis modulus values with X-axis and Y-axis modulus values are statistically significant, i.e., possessing a magnitude greater than 1.664 (-10.6 and 17.5, respectively), and the t-statistics when comparing the Z-axis hardness values with X-axis and Y-axis hardness values are statistically significant (4.84 and 109.9, respectively). The t-statistics between X-axis and Y-axis modulus values are not statistically significant. This result suggests the conclusion that, based on the experiments on the specimen in the current investigation, a slight but statistically significant anisotropy exists for this sample of Carrara marble.

5.2.4 Decreased Modulus and Hardness near Process Zone

In this section, the decrease in indentation values (modulus and hardness) on each process zone surface (Surface Z1, Z2, Z3, and X) is discussed, and the statistical significance of the decrease is analyzed. Then, the decrease in indentation values (modulus and hardness) on the process zone surfaces with respect to intact material is discussed, and the statistical significance of the decrease is analyzed. This section closes by linking this statistically significant decrease in modulus and hardness with a more fundamental mechanism.

Both modulus and hardness decrease on the process zone specimens. The experimental results which inform this trend are displayed in Tables 5.2, 5.5, 5.4, and 5.3. The tables display the median values and spread (standard deviations) of line indentation tests conducted

Surface	Far (GPa)	Middle (GPa)	Near (GPa)
Z1	0.27	0.48	0.77
Z2	0.25	0.22	0.31
Z2, at depth	0.52	—	0.49
X	0.26	0.21	0.32
Average	**0.33**	**0.30**	**0.47**

Table 5.3: The spread (i.e., standard deviation) of Hardness values on process zone surfaces.

Surface	Far (GPa)	Middle (GPa)	Near (GPa)	Decrease Near P.Z.
Z1	72.96	68.88	67.74*	7.2%*
Z2	70.14	72.73	71.08	-1.3%
Z3 (*Z2, at depth)*	67.70	—	67.37	0.5%
X	71.80	68.43	68.76*	4.2%*
Average	**70.65**	**70.01**	**68.74**	**2.6%**

Table 5.4: Summary of nanoindentation results (median Modulus values) on Process Zone (P.Z.) specimen surfaces. The test marked with * are compared with intact material values in Section 5.2.4.

on process zone surfaces at different orientations and progressively closer to (i.e., near) the process zone, and the decrease in indentation values (modulus and hardness) between the test farthest from the process zone on the specimen ("Far") and the test nearest the process zone ("Near").

Tables 5.2 and 5.4, in conjunction with Figures 5-2, 5-3, 5-4, and 5-5 analyze the statistical signicance of the decrease in hardness and modulus with closeness to the process zone. For Surface Z1, the t-statistic between the "Near" test and the "Far" test is large for both modulus ($t = 4.65$) and hardness ($t = 12.1$); a statistically signifant decrease in modulus and hardness near the process zone exists for Surface Z1. For Surface Z2, the t-statistic between the "Near" test and the "Far" test is large for the modulus ($t = 4.65$). A statistically significant decrease in modulus near the process zone exists for Surface Z2. For Surface Z3, at depth, analysis

Surface	Far (GPa)	Middle (GPa)	Near (GPa)
Z1	6.81	9.59	15.4
Z2	6.73	7.00	6.92
Z2, at depth	6.81	—	11.9
X	7.65	6.40	8.31
Average	**7.00**	**7.66**	**10.6**

Table 5.5: The spread (i.e., standard deviation) of Modulus values on process zone surfaces.

yielded no statistically significant t-statistics; there is no significant decrease in modulus or hardness on Surface Z3 (Figure 5-4). Also, for Surface Z2 modulus values, and Surface X hardness values, the t statistics between the two tests furthest from the process zone are not statistically significant (not shown); this result implies that trends are more apparent near and far from the process zone. Finally, for Surface X, the t-statistic between the "Near" test and the "Far" test is large for both modulus ($t = -4.74$) and hardness ($t = 4.56$); a statistically signifant decrease in modulus and hardness near the process zone exists for Surface X. With a consideration of all of the t-statistics presented above, the significant decrease in modulus and hardness thus occurs on the side of the process zone which corresponds to Surfaces Z1 and X.

Next, a comparison is made with a t-test between the indentation values (modulus and hardness) nearest the process zone on Surfaces Z1 and X (marked with "*" in Table 5.2 and 5.4), and those on intact material. Before the t-test is presented, note that he average spread of modulus and hardness values in process zone surfaces (Tables 5.5 and 5.3) is greater than that of typical intact material (Tables 4.2 and 4.3). This difference in spreads between intact and process zone material necessitates the use of the Welch-Satterthwaite t-statistic, t_{WS} in determining the statistical significance of the difference between intact and process zone material.

A t-test between the Z1 Surface ("Near") in the process zone, and the intact Z values yields t-statistics of -110.8 in the case of modulus, and -110.6 in the case of hardness. Thus, a stastically significant difference in both modulus and hardness exists between intact and process zone material with a Z-axis normal. Another t-test between the X Surface in the process zone ("Near"), and the intact X values yields t-statistics of 15.0 in the case of modulus, and -130.1 in the case of hardness. Thus a statistically significant difference in both modulus and hardness exists between intact and process zone material with an X-axis normal. In all cases except the X-axis modulus, this difference corresponds to a lower modulus and hardness in process zone material; in the case of the X-axis, the process zone exhibits a slightly higher modulus. Nevertheless, the majority of results suggest that a decreased modulus and hardness dominate process zone material.

The decrease in both hardness and modulus near the process zone suggest two phenomena that affect the material response in the process zone:

(i) Change in strength

(ii) Damage, at a scale smaller than the indentation depth; i.e., here less than 250 nm.

Change in Strength

The change in strength is suggested by the trends in hardness (Table 5.2). In this particular experiment, hardness decreases by 18.8% in the nanoindentation tests near the surface closest to the process zone (Surface Z1, Table 5.2). Hardness is very low for all nanoindentation tests within the marble slab (below 3 GPa, Surface X, which lies on a horizontal plane within the marble slab, and also Surface Z2 at depth, which lies on a vertical plane within the marble slab, Table 5.2 and Figure 3-4). Note that the hardness value closest to the process zone is very similar to the hardness value near the grain boundaries; both grain boundaries and process zone material exhibit low hardnesses (below 3 GPa, light green in Figure 4-26). Note also that the hardness is the lowest in Surface X. This result potentially couples the slight pre-existing anisotropy of the parent slab with the reorientation of calcium carbonate unit cells near the process zone.

Hardness links with material strength, so a change in hardness suggests that the material has changed. The process zone manifests itself as a zone of reduction of strength, much in the same way as grain boundaries (discussed in the next section, Section 5.2.5). Further experimentation and analysis beyond the results of the current study will better illuminate this potential change in strength.

Damage, at a Scale Smaller Than the Indentation Depth

The damage is suggested by the trends in modulus identifed in the current investigation. Modulus decreases to values near and below 68 GPa in the nanoindentation tests closest to the process zone (Surfaces Z1, Z2 at depth, and X, Table 5.4). In the nanoindentation tests nearest the surface and close to the process zone, modulus decreases by 7.2% (Surface Z1, Table 5.2). Note that the modulus value closest to the process zone is very similar to the modulus value near the grain boundaries; both grain boundaries and process zone material exhibit low moduli (below $\approx$68 GPa, light green in Figure 4-26).

Similar to the decrease in modulus found at the grain boundaries, such a damage is typically

the signature of cracks and other imperfections at smaller scales. The extent of this damage zone may be inferred by collectively assessing both nanoindentation values and locations.

This damage occurs at a scale smaller than the characteristic material length scale sensed by nanoindentation. In fact, nanoindentation to a typical depth of 250 nm has identified a change near the process zone. The mechanism, which has induced this damage, must be smaller than the depth of indentation. The length scale of this mechanism is therefore less than 250 nm. Ultimately, nanomechanical property trends nevertheless suggest a change in the microstructure of the experimental material within the process zone. Further experimentation and analysis beyond the results of the current study will better illuminate this potential mechanism and material damage.

5.2.5 Decreased Modulus and Hardness at Grain Boundaries

As indicated in Figure 4-26, both modulus and hardness decrease from grain centers to grain boundaries. Based on the figure, the decreases are approximately 10 GPa (from 75 GPa to 65 GPa, a decrease of about 14%) in the case of modulus, and 0.5 GPa (from 3 GPa to 2.5 GPa, a decrease of about 17%) in the case of hardness. In this particular instance, these decreases are on the same order as the decrease in modulus and hardness near the process zone, discussed in the previous section and in Tables 5.2 and 5.4. The statistical significance of the intact-process zone decrease thus implies the statistical significance of the grain-boundary decrease

A lower hardness at grain boundaries corresponds to local weakness. This nanoindentation result suggests a strength-related conclusion: when compared to the center of the grain, the marble nearest the grain boundaries sustains a lower stress before inelastic deformation.

A lower modulus at grain boundaries potentially indicates grain damage near the boundaries. The nanomechanical property of modulus responds to geometrical changes of the material, rather than to a change in the intrinsic strength of the material as indicated by hardness. If microcracks are considered geometrical changes, a decrease in modulus near grain boundaries potentially indicates an increase in dislocations and microcracks near grain boundaries. Additionally, this conclusion serves as a nano-mechanical validation of a conclusion of existing microcrack studies: microcracks are more frequent near grain boundaries [74]. Further experimentation and analysis beyond the results of the current study will better illuminate this

potential change in strength and material damage.

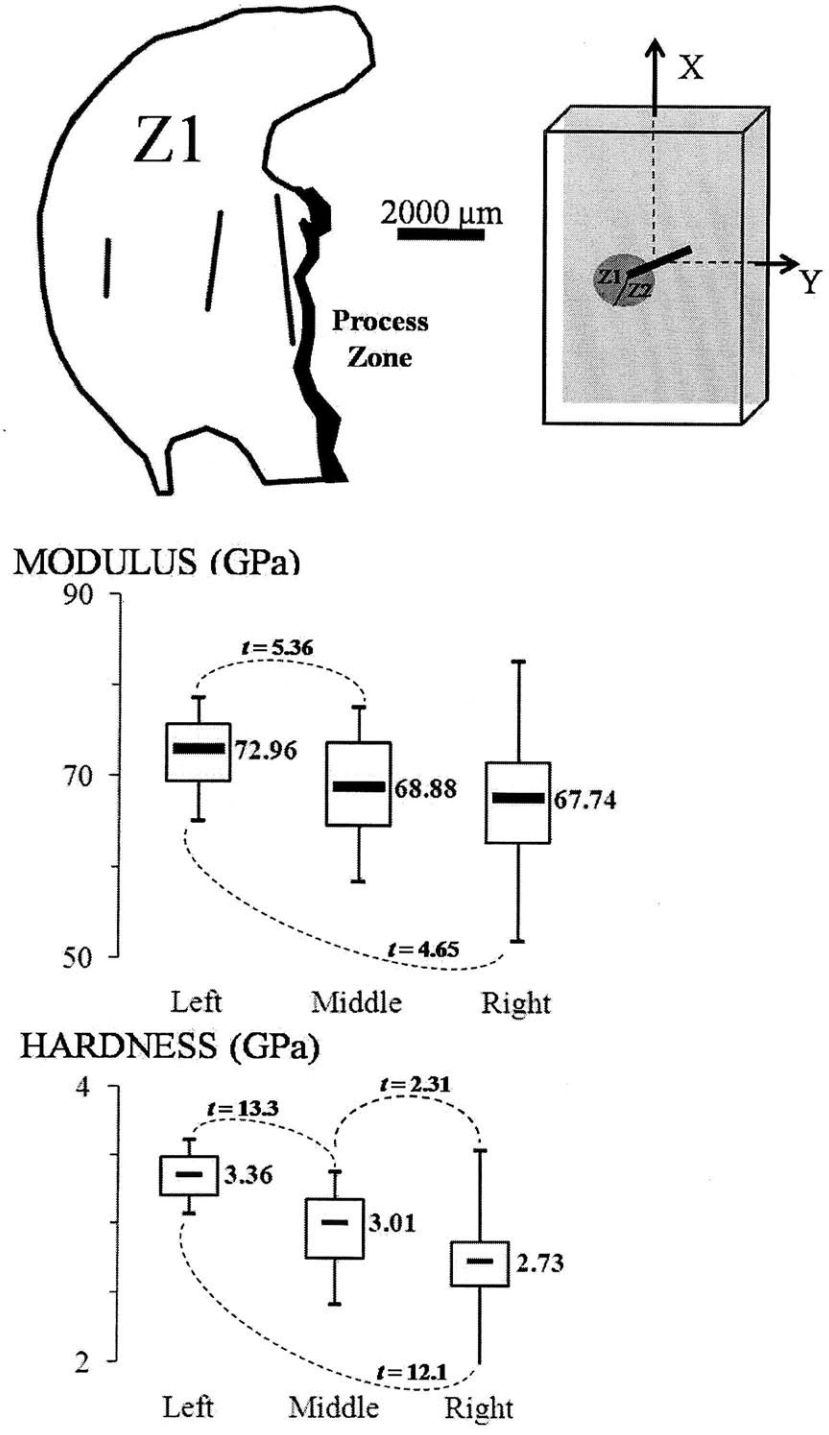

Figure 5-2: Statistically significant ($|t| > 1.664$) Student's t-distribution test statistics for indentation tests on process zone material, Specimen Z1. This statistical analysis enhances data initially presented in Figure 4-27.

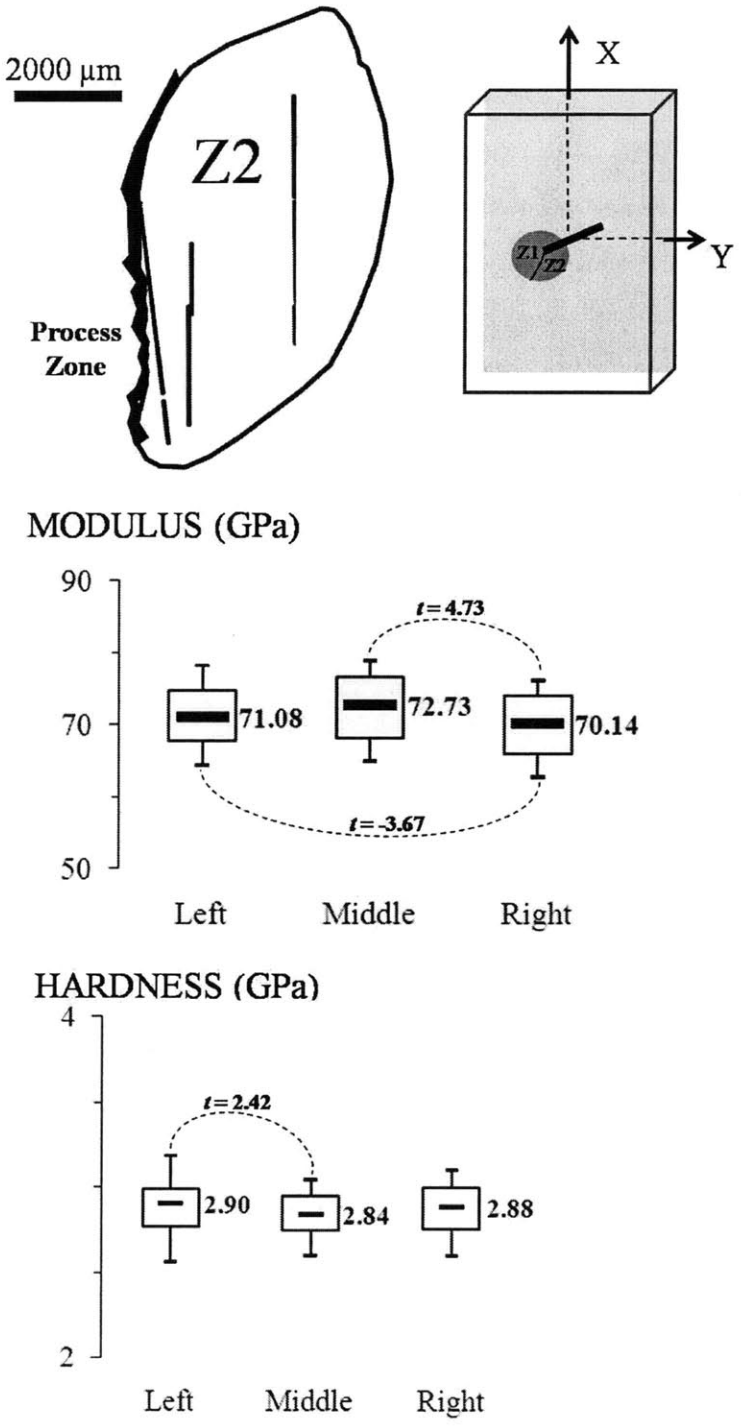

Figure 5-3: Statistically significant ($|t| > 1.664$) Student's t-distribution test statistics for indentation tests on process zone material, Specimen Z2. This statistical analysis enhances data initially presented in Figure 4-28.

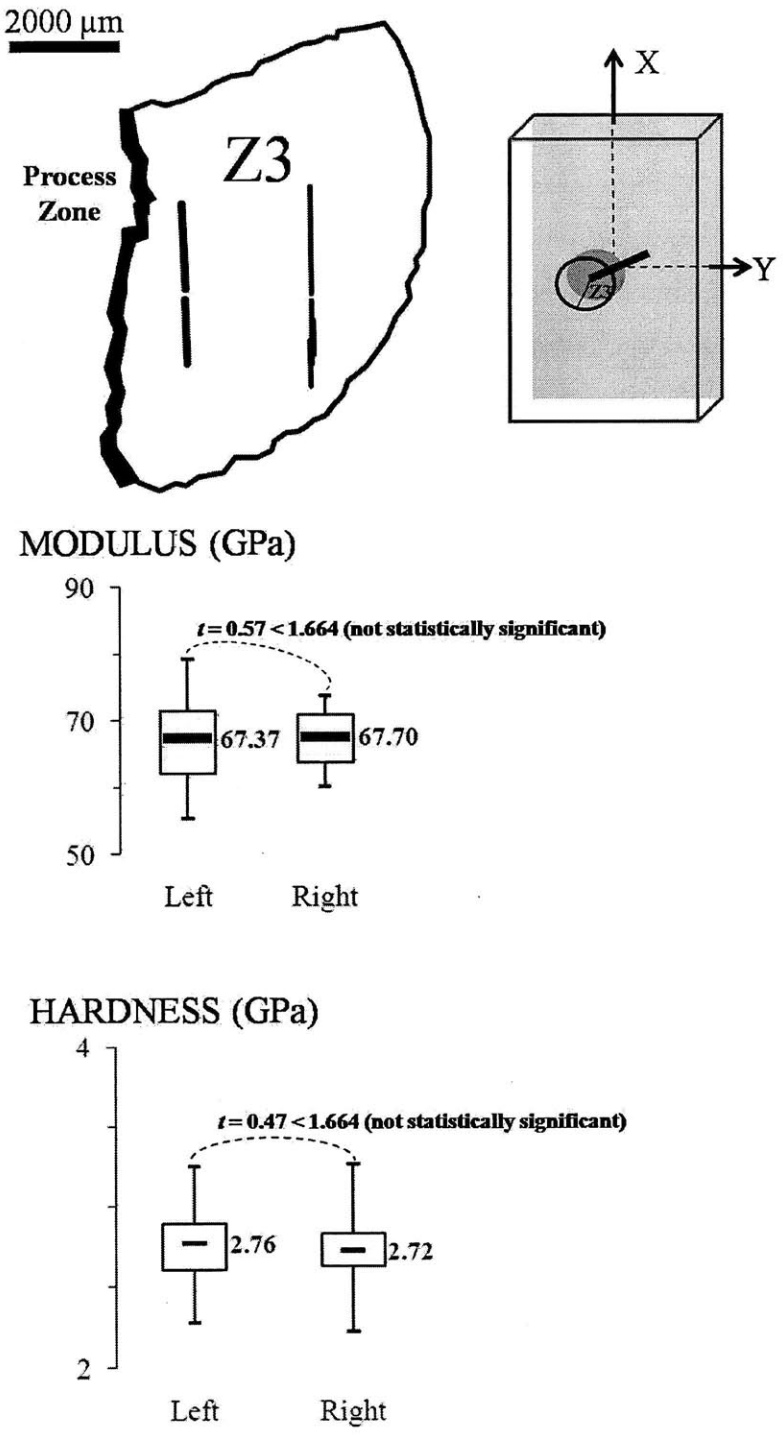

Figure 5-4: Student's t-distribution test statistics for indentation tests on process zone material, Specimen Z3. This statistical analysis enhances data initially presented in Figure 4-29.

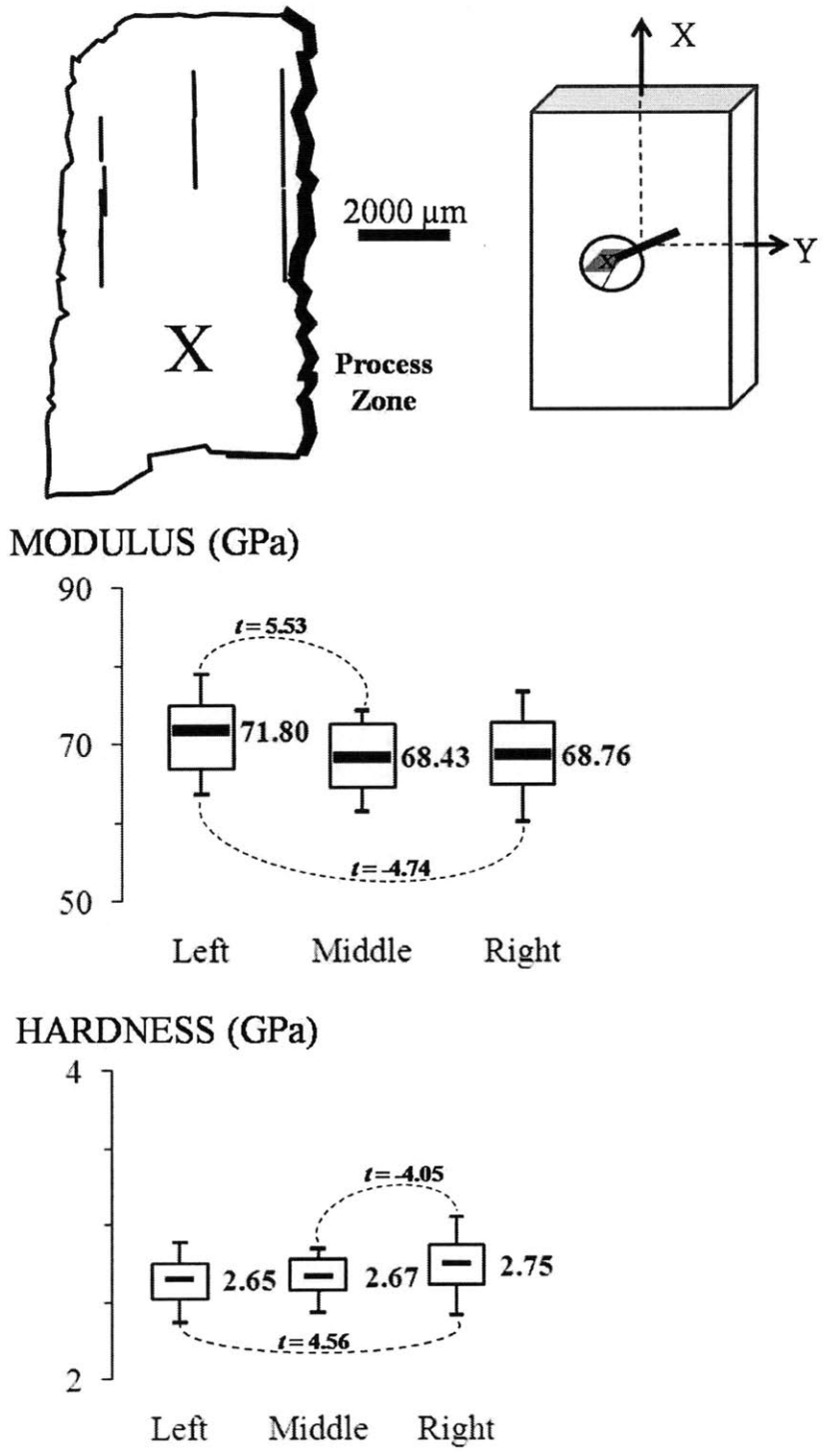

Figure 5-5: Statistically significant ($|t| > 1.664$) Student's t-distribution test statistics for indentation tests on process zone material, Specimen X. This statistical analysis enhances data initially presented in Figure 4-30.

5.3 Chapter Summary

This chapter has returned to the research question with a review of experimental highlights, presentation and analysis of the results, and a discussion of the first answers to the research question. The results suggest a scale for the mechanism under question, and confirm a statistically significant correlation between property change and material state (i.e., intact or process zone). The results of the investigation ultimately point towards the significant existence of a nanomechanism (length scale less than 250 nm) in the marble process zone which deteriorates both the elastic behavior and strength of the marble. Nevertheless, a part of the question remains for further research: the precise form of the mechanism, as well as whether the process zone induces the mechanism, or whether the mechanism pre-exists and thereby encourages the process zone.

Chapter 6

Summary and Perspectives

This investigation sought to take a first step towards understanding the fundamental micromechanism which governs the cracking of marble. An understanding of both the scale and function (i.e., to drive and/or retard cracking) of the micromechanism were vital components to the completion of the investigation. The investigation necessarily included the development of a multi-disciplinary investigative technique to assess both intact and process zone material, an assessment of the fundamental properties of both intact and process zone material, and finally an identification of the sought-after micromechanism.

This chapter closes this investigation. The chapter presents both immediate contributions and limitations of the work (Section 6.1: Contributions, Section 6.2: Limitations), and closes with the next steps in this developing research area (Section 6.3: Recommendations for Future Research).

6.1 Contributions

6.1.1 Research Contributions

The ESEM investigation provides images of established process zone microstructural features in their most natural state: on specimens that have undergone no surface preparation. The study extends this information by quantifying the otherwise qualitative assessment provided by an image (Section 4.1.2). The crack density levels quantified by the study provide steps towards a complete picture of process zone damage. This picture includes two pieces of information:

change in nanomechanical properties (discussed in the next paragraph), and a quantifiable level of microcracking.

The nanoindentation investigation provides nanoindentation values of both intact and process zone marble. Given the relative newness of the technology that allows for investigation at such a small scale (Section 2.1.6), nanomechanical information of brittle materials such as rock is a very recent research area. Nanomechanical information of process zone materials is also a very recent research area. The study thus presents new quantitative information that contributes to two developing and increasingly important fields.

6.1.2 Practical Contributions

This work provides an idea on possible strengthening mechanisms for application to cracked materials. If the scale of damage in such structures with pre-existing cracks is the nanoscale, the solution should lie at this scale as well. The most applicable effect of the study on the practice of engineering is a deeper understanding of the cracking mechanism and some idea of the extent of cracking around the process zone.

6.2 Limitations

In this study, the basis for comparison of intact and process zone materials are two different areas of a specimen post-cracking. Ideally, a study should evaluate microproperties of the same area before and after cracking, or during the crack propagation. Currently the surface preparation for accurate nanoindentation (Section 3.2.1: Specimen Preparation) precludes conducting nanoindentation on large specimens prior to loading to generate a process zone. Due to uneven weight distribution, surface irregularities, and size, larger samples are harder to polish than small samples; any final polish obtained on the sample size of this study would be unsuitable for nanoindentation. However, the possiblity exists to physically scale down the research approach. Smaller samples may be prepared, polished, tested with nanoindentation for microproperties at the crack tip, then cracked and re-tested with nanoindentation at the crack tip.

A technique that may provide even more relevant data is an evaluation of microproperty

change *during* cracking, using a similar method as the x-rays employed in the study of the ferroelastic ceramic [41]. Nanoindentation during loading in a uniaxial testing machine is currently unfeasible. However, the study may again be scaled down and apparati designed to accomodate such an experiment. A simple approach may be to confine a specimen in a chamber controlled by screws, insert the specimen and chamber into the nanoindentation machine, and determine the microproperties during various levels of confinement.

6.3 Recommendations for Future Research

Influence of Loading Type. It is anticipated that marble specimens with different initial crack geometries will exhibit similar trends of indentation modulus and hardness, as well as microstructural features, following process zone generation. Additionally, the microproperty change around process zones of marble samples with pre-existing cracks loaded in tension or dynamically loaded may be explored.

Zone of Modulus Decrease. This study identified damage within the crack tip process zone. This zone of damage extended halfway across the diameter of the testing specimen, a length of approximately 7000 μm. Ultimately, the zone of microproperty change due to cracking of uniaxially loaded samples may be defined in all directions around the crack tip of a marble specimen. Testing of cracks at different flaw geometries and in different geomaterials may further define the zone of damage. The determination of common trends in microproperty change in process zone areas across different geomaterials, load types, and crack types will provide a valuable link between macroscopic cracking and the corresponding change of microproperties for a geomaterial.

Influence of Material. Nanoindentation results have confirmed a change in material strength (evidenced by decreased hardness) as well as abundance of microcracks (evidenced by decreased modulus) near grain boundaries and in the process zone of marble. Nanoindentation in other granular materials, as well as more heterogeneous granular materials, such as granite, will help to refine the mechanism at play near grain boundaries and in the process zone. In order to ultimately predict the reduction in hardness and modulus, a final goal for the investigation would be a material- and scale-independent model of strength reduction near grain boundaries

and within the process zone.

Bibliography

[1] Alber, M., and U. Hauptfleisch. "Generation and Visualization of Microfractures in Carrara Marble for Estimating Fracture Toughness, Fracture Shear and Fracture Normal Stiffness." International Journal of Rock Mechanics and Mining Sciences 36.8 (1999): 1065-71.

[2] Alber, M., and A. Brardt. "Factors Influencing Fracture Toughness KIC from Simple Screening Tests." International Journal of Rock Mechanics and Mining Sciences 40.5 (2003): 779-84.

[3] Atkinson, B. K. "Fracture Toughness of Tennessee Sandstone and Carrara Marble using the Double Torsion Testing Method." International Journal of Rock Mechanics and Mining Sciences & Geomechanics Abstracts 16.1 (1979): 49-53.

[4] Austin, N. J. Grain Size Evolution and Strain Localization in Deformed Marbles. Doctor of Philosophy in Earth, Atmospheric, and Planetary Sciences Massachusetts Institute of Technology, 2008 Massachusetts Institute of Technology.

[5] Barenblatt, G. I. "The Formation of Equilibrium Cracks during Brittle Fracture. General Ideas and Hypotheses. Axially Symmetric Cracks." Journal of Applied Mathematics and Mechanics 23.3 (1959): 434-44.

[6] Barenblatt, G.I. Scaling, Self-Similarity, and Intermediate Asymptotics. New York, N.Y.: Cambridge University Press, 1996.

[7] Beste, Ulrik, and Staffan Jacobson. "Micro Scale Hardness Distribution of Rock Types Related to Rock Drill Wear." WEAR: An International Journalon the Science and Technology of Friction, Lubrication andWear.254 (2003): 1147-54.

[8] Bobet, A. Fracture Coalescence in Rock Materials: Experimental Observations and Numerical Predictions. Doctor of Science in Geotechnical Engineering Department of Civil and Environmental Engineering, Massachusetts Institute of Technology, 1997.

[9] Bobet, A., and H. H. Einstein. "Fracture Coalescence in Rock-Type Materials Under Uniaxial and Biaxial Compression." International Journal of Rock Mechanics & Mining Sciences 35.7 (1998): 863-88.

[10] Bobko, C. Assessing the Mechanical Microstructure of Shale by Nanoindentation: The Link between Mineral Composition and Mechanical Properties. Doctor of Philosophy in Structures and Materials Massachusetts Institute of Technology, 2008 Massachusetts Institute of Technology.

[11] Borodich, F. M., L. M. Keer, and C. S. Korach. "Analytical Study of Fundamental Nanoindentation Test Relations for Indenters of Non-Ideal Shapes." Nanotechnology (2003): 803-8.

[12] Brace, W. F., et al. "Cracks and Pores: A Closer Look." Science 178 (1972): 162-4. \def\@biblabel#1{\hspace*{-\labelsep}}

[13] Broz, Margaret E., Robert F. Cook, and Donna L. Whitney. "Microhardness, Toughness, and Modulus of Mohs Scale Minerals." American Mineralogist 91 (2006): 135-42.

[14] Buckingham, E. "On Phyiscally Similar Systems; Illustrations of the use of Dimensional Equations." Physical Reviews 4 (1914): 345-76.

[15] Bulychev, S. I., et al. "Determining Young's Modulus from the Indentor Penetration Diagram." Industrial Laboratory (1976): 1409-12.

[16] Bulychev (b), S. I., et al. "Mechanical Properties of Materials Studied from Kinetic Diagrams of Load Versus Depth of Impression during Microimpression." Problemy Prochnosti 9 (1976): 79-83.

[17] Butenuth, C., et al. "Observations on the Measurement of Tensile Strength using the Hoop Test." International Journal of Rock Mechanics and Mining Sciences & Geomechanics Abstracts 30.2 (1993): 157-62.

[18] Constantinides, G., Ulm, F.-J., & Van Vliet, K. (2003). 'On the use of nanoindentation for cementitious materials', Materials and Structures 36 (257): 191-196.

[19] Constantinides, G. Invariant Mechanical Properties of Calcium-Silicate-Hydrates (C-S-H) in Cement-Based Materials: Instrumented Nanoindentation and Microporomechanical Modeling. Doctor of Philosophy in the field of Structures and Materials Massachusetts Institute of Technology, 2006 Massachusetts Institute of Technology.

[20] Constantinides, G., et al. "Grid Indentation Analysis of Composite Microstructure and Mechanics: Principles and Validation." Materials Science and Engineering: A 430.1-2 (2006): 189-202.

[21] Cowie, P. A., and C. H. Scholz. "Physical Explanation for the Displacement-Length Relationship of Faults using a Post-Yield Fracture Mechanics Model." Journal of Structural Geology 14.30 (1992): 1133-48.

[22] CSM Instruments SA (2004) Nanohardness Test Users Manual. Peseux, Switzerland.

[23] DeJong, M. J., and F. -J Ulm. "The Nanogranular Behavior of C-S-H at Elevated Temperatures (Up 700 Deg. C)." Cement and Concrete Research 37 (2007): 1-12.

[24] Doerner, M. F., and W. D. Nix. "A Method for Interpreting the Data from Depth-Sensing Indentation Instruments." Journal of Materials Research 1.4 (1986): 601-9.

[25] Dormieux, L., D. Kondo, and F. -J Ulm. Microporomechanics. West Sussex, England: John Wiley & Sons, Ltd., 2006.

[26] Dugdale, D. S. "Yielding of Steel Sheets Containing Slits." Journal of the Mechanics and Physics of Solids 8 (1960): 100-4.

[27] Ganneau, F. P., G. Constantinides, and F. -J Ulm. "Dual-Indentation Technique for the Assessment of Strength Properties of Cohesive-Frictional Materials." International Journal of Solids and Structures 43.6 (2006): 1727-45.

[28] Goldstein, J., et al. Scanning Electron Microscopy and X-Ray Microanalysis. New York: Kluwer Academic/Plenum Publishers, 2003.

[29] Gradicek, S. 3.074/3/34: Imaging of Materials. Course Notes ed. Massachusetts Institute of Technology, Cambridge, MA, USA:, 2010.

[30] Griffith, A. A. "The Phenomena of Rupture and Flow in Solids." Philosophical Transactions of the Royal Society of London.Series A, Containing Papers of a Mathematical or Physical Character (1920): 163-98.

[31] Hawkes, I. and M. Mellor. "Uniaxial testing in rock mechanics laboratories." Engineering Geology, 4 (1970): 177-285.

[32] Hay, J.C., Bolshakov, A. & Pharr, G.M. "A critical examination of the fundamental relations used in the analysis of nanoindentation data." Journal of Materials Research 14, 6 (1999): 2296-2305.

[33] Hedia, H. S., et al. "The Influence of Nanoadhesives on the Tensile Properties and Mode-I Fracture Toughness of Bonded Joints." Engineering Fracture Mechanics 73 (2006): 1826-32.

[34] Hertz H. Miscellaneous papers. London: Macmillan, 1896.

[35] Hodge, H. C., and J. H. McKay. "The "Microhardness" of Minerals Comprising the Mohs Scale." The American Mineralogist 19 (1934): 161-8.

[36] Inglis, C. E. "Stresses in a Plate due to the Presence of Cracks and Sharp Corners." Spring Meetings of the Fifty-Fourth Session of the Institution of Naval Architects. March 14, 1913.

[37] Irwin, G.R. "Onset of fast crack propagation in high strength steel and aluminum alloys." Sagamore Research Conference Proceedings, 2 (1956): 289-305.

[38] Irwin, G.R. "Analysis of stresses and strains near the end of a crack traversing a plate." Journal of Applied Mechanics (1957), 24, pp. 361-364.

[39] Jaeger, J. C. "Failure of Rocks Under Tensile Conditions." International Journal of Rock Mechanics and Mining Science & Geomechanics Abstracts 4.2 (1967): 219-27.

[40] Jobmann, M., Th Wilsnack, and H. -D Voigt. "Investigation of Damage-Induced Permeability of Opalinus Clay." International Journal of Rock Mechanics & Mining Sciences (2009): 1-7.

[41] Jones, J. L., et al. "Crack Tip Process Zone Domain Switching in a Soft Lead Zirconate Titanate Ceramic." Acta Materialia 55 (2007): 5538-48.

[42] Khan, S. M. A., and M. K. Khraisheh. "A New Criterion for Mixed Mode Fracture Initiation Based on the Crack Tip Plastic Core Region." International Journal of Plasticity 20 (2004): 55-84.

[43] Kilburn, Christopher R. J., and David N. Petley. "Forecasting Giant, Catastrophic Slope Collapse: Lessons from Vajont, Northern Italy." Geomorphology 54.1-2 (2003): 21-32.

[44] Larsson, P.-L. et al. 1996. Analysis of Berkovich indentation. Int. J. Solids Structures. 33.2: 221–248.

[45] Li, J. H., et al. "Permeability Tensor and Representative Elementary Volume of Saturated Cracked Soil." Canadian Geotechnical Journal.46 (2009): 928-42.

[46] Love, A. E. H. A Treatise on the Mathematical Theory of Elasticity. New York, N.Y., U.S.A.: Dover Publications, Inc., 1927.

[47] Love, A. I. Three-Dimensional Problems of the Theory of Elasticity. Ed. J. R. M. Radok. New York, NY, USA: Interscience Publishers, 1964.

[48] Marini, P., and R. Bellopede. "Bowing of Marble Slabs: Evolution and Correlation with Mechanical Decay." Construction and Building Materials 23.7 (2009): 2599-605.

[49] Mendenhall, W. & Sincich, T. Statistics for Engineering and the Sciences, 4th Ed. Prentice Hall, Upper Saddle River, NJ, 1995.

[50] Miller, Mahalia; Bobko, Christopher; Vandamme, Matthieu; and Ulm, Franz-Josef. "Surface roughness criters for cement paste nanoindentation." Cement and Concrete Research, 38, 467-476 (2008)

[51] Molli, G., et al. "Microfabric Study on the Deformational and Thermal History of the Alpi Apuane Marbles (Carrara Marbles), Italy." Journal of Structural Geology 22 (2000): 1809-25.

[52] Failure Mechanisms in Building Construction. Ed. David H. Nicastro. New York, NY: American Society of Civil Engineers Press, 1997.

[53] Oliver, W.C. and Pharr, G.M. "An Improved Technique for Determining Hardness and Elastic Modulus using Load and Displacement Sensing Indentation Experiments." Journal of Materials Research 7.6 (1992): 1564-83.

[54] Peng, S., and A. M. Johnson. "Crack Growth and Faulting in Cylindrical Specimens of Chelmsford Granite." International Journal of Rock Mechanics and Mining Sciences & Geomechanics Abstracts 9.1 (1972): 37,42, IN5-IN6, 43-60, IN7-IN14, 61-74, IN15-IN18, 75-86.

[55] Pough, Frederick H. Rocks and Minerals. Boston, Massachusetts: Houghton Mifflin Company, 1996.

[56] Purcell, A. H., and J. Weertman. "Crack Tip Area in Fatigued Copper Single Crystals." Metallurgical Transactions 5 (1974): 1805-9.

[57] Reichelt, Rudolf. "Scanning Electron Microscopy." Science of Microscopy. Ed. Peter W. Hawkes and John C. H. Spence.Springer Science+Business Media, LLC, 2007. 133-272.

[58] Reyes, O. Experimental Study and Analytical Modelling of Compressive Fracture in Brittle Materials. Doctor of Philosophy in Civil Engineering Massachusetts Institute of Technology, 1991 Massachusetts Institute of Technology.

[59] Rice, J.R. 1968. A path independent integral and the approximate analysis of strain concentration by notches and cracks. J. Appl. Mech. 35: 379–386.

[60] Ruxton, G. D. "The Unequal Variance t-Test is an Underused Alternative to Student's t-Test and the Mann-Whitney U Test." Behavioral Ecology. (2006): 688-690.

[61] Saxena, A., and S. D. Antolovich. "Low Cycle Fatigue, Fatigue Crack Propagation and Substructures in a Series of Polycrystalline Cu-Al Alloys." Metallurgical Transactions A 6A (1975): 1809-28.

[62] Schulson, Erland M. "Brittle Failure of Ice." Engineering Fracture Mechanics 68.17-18 (2001): 1839-87.

[63] Singer, J. A., C. A. Link, and S. R. Iverson. "High Resolution Seismic Refraction Tomography for Determining Depth of Blast Induced Damage in a Mine Wall." The Journal of Explosives Engineers (2010): 34-43.

[64] Sneddon, I. "The Relation between Load and Penetration in the Axisymmetric Boussinesq Problem for a Punch of Arbitrary Profile." International Journal of Engineering Science. 3 (1965): 47-57.

[65] Sprunt, Eve S., and W. F. Brace. "Direct Observation of Microcavities in Crystalline Rocks." International Journal of Rock Mechanics and Mining Science & Geomechanics Abstracts, 11.4 (1974): 139-50.

[66] Stillwell, N.A., & Tabor, D. (1961) "Elastic recovery of conical indentations." Proceedings of Physical Society 78: 169-179.

[67] Tabor, D. "A Simple Theory of Static and Dynamic Hardness." Proceedings of the Royal Society of London: Series A, Mathematical and Physical Sciences. 192.1029 (1948): 247-74.

[68] Uguz, A., and J. W. Martin. "Plastic Zone Size Measurement Techniques for Metallic Materials." Materials Characterization 37 (1996): 105-18.

[69] Ulm, F. -J. Fracture Modes, Stress Intensity Factors and Toughness. Course Notes: 1.570, Durability Mechanics. ed. Massachusetts Institute of Technology:, 2010.

[70] Vandamme, M., and F. -J Ulm. The Nanogranular Origin of Concrete Creep: A Nanoindentation Investigation of Microstructure and Fundamental Properties of Calcium-Silicate-Hydrates. Doctor of Philosophy Department of Civil and Environmental Engineering, Massachusetts Institute of Technology, 2008.

[71] Vermilye, J. M., and C. H. Scholz. "The Process Zone: A Microstructural View of Fault Growth." Journal of Geophysical Research 103.B6 (1998): 12223-37.

[72] Wang, E.Z. and Shrive, N.G. "Brittle fracture in compression: mechanics, models and criteria." Engineering Fracture Mechanics, 52, 6 (1995): 1107 – 1126.

[73] Wong, N. Y. "Crack Coalescence in Molded Gypsum and Carrara Marble." Doctor of Philosophy in the field of Geotechnical and Geoenvironmental Engineering Massachusetts Institute of Technology, 2008.

[74] Wong, N.Y. 2009. Crack coalescence in molded gypsum and Carrara marble: Part 2 – Microscopic observations and interpretation. Rock. Mech. Rock.Eng. 42: 513–545.

[75] Zhang, Z. X. "An Empirical Relation between Mode I Fracture Toughness and the Tensile Strength of Rock." International Journal of Rock Mechanics and Mining Sciences 39.3 (2002): 401-6.

[76] Zhu, W., et al. "Nanoindentation Mapping of Mechanical Properties of Cement Paste and Natural Rocks." Materials Characterization 58 (2007): 1189-98.

Appendix A

Microscopic Image Manipulation

Microscopic imaging provides a good description of process zone microstructure. The purpose of microscopic image manipulation is to highlight relevant microstructural features such as microcracks and spalling. There are two types of microscopic images used in the study: single images, and collaged images.

Single images have a typical size (length of image) between 100 and 800 μm and present local phenomena and features.

Collaged images have a typical size upwards of 2,000 μm and present trends in microstructural features over large areas. Collaged images consist of many single images stitched together in an overlapping fashion to ultimately create a single image.

The steps in the manipulation of each image type follow. Note that the particular steps followed for each image, as well as the degree to which they are followed, varies from image to image; it is a function of the original image quality and the microstructural features contained in the image. All steps should be followed only as necessary.

A.1 Single Images ("Spotlighting" Correction)

After the image is opened in Photoshop, spotlighting is corrected. Dark corners are apparent in the image of a microcrack (Figure A-1); the image appears to be illuminated by a single spotlight above its center. ESEM images exhibit this effect when the distance between the electron beam and the sample surface is too large; the backscattered electrons on the edges

of the image are farthest from the detector, and may be lost before being detected. Select a rectangular central portion of the image (Figure A-1).

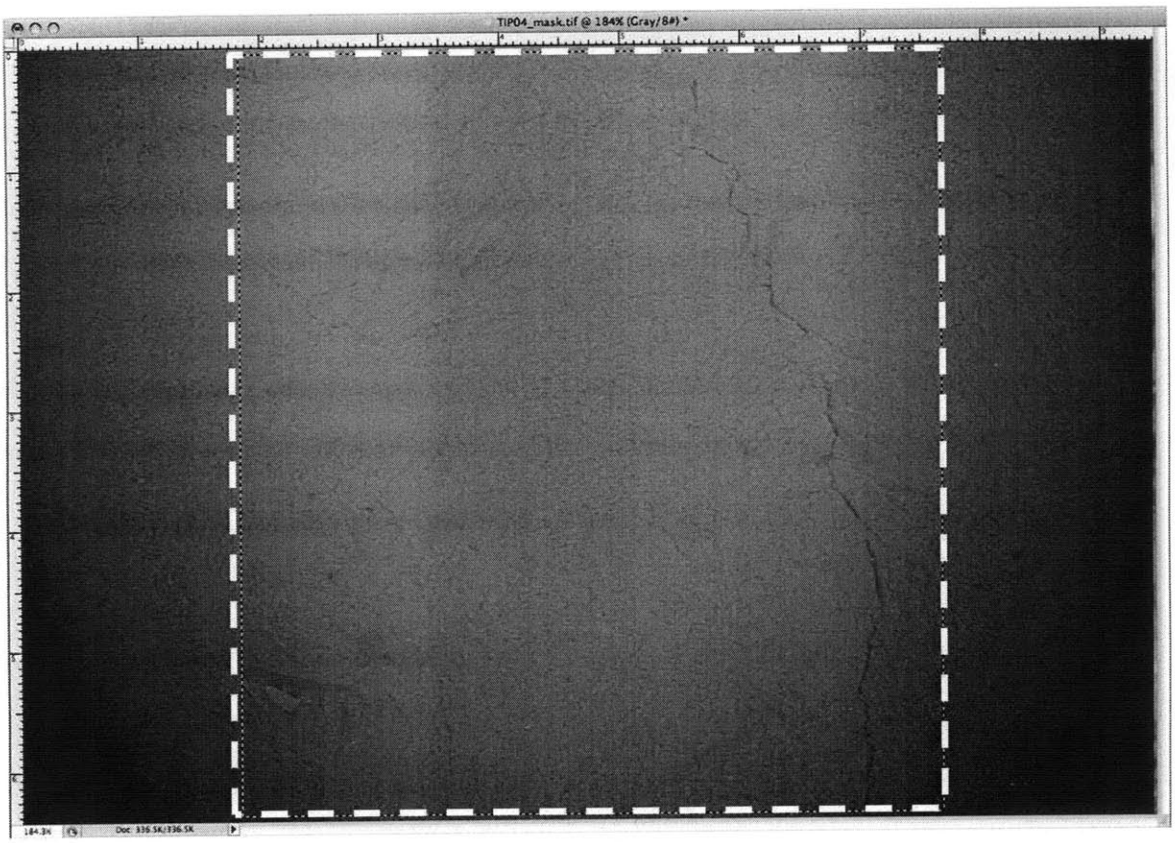

Figure A-1: The dashed line indicates the selected area.

Next, the edges of the selection are feathered; in this case the edges were feathered by 30 pixels (Figure A-2). Feathering is a Photoshop command which rounds the sharp edges of a rectangular selection.

Then, the inverse area is selected (Figure A-3). This will focus the next actions on everything outside of the current rectangular selection.

A Brightness/Contrast Adjustment Layer is then created by selecting the option shown in the image (Figure A-4). The Adjustment Layer is simply a layer in the shape of the inverse selection, which lies over the inverse selection. The Adjustment Layer can be adjusted without changing the original image.

The Brightness/Contrast of this layer mask (Figure A-5) is adjusted.

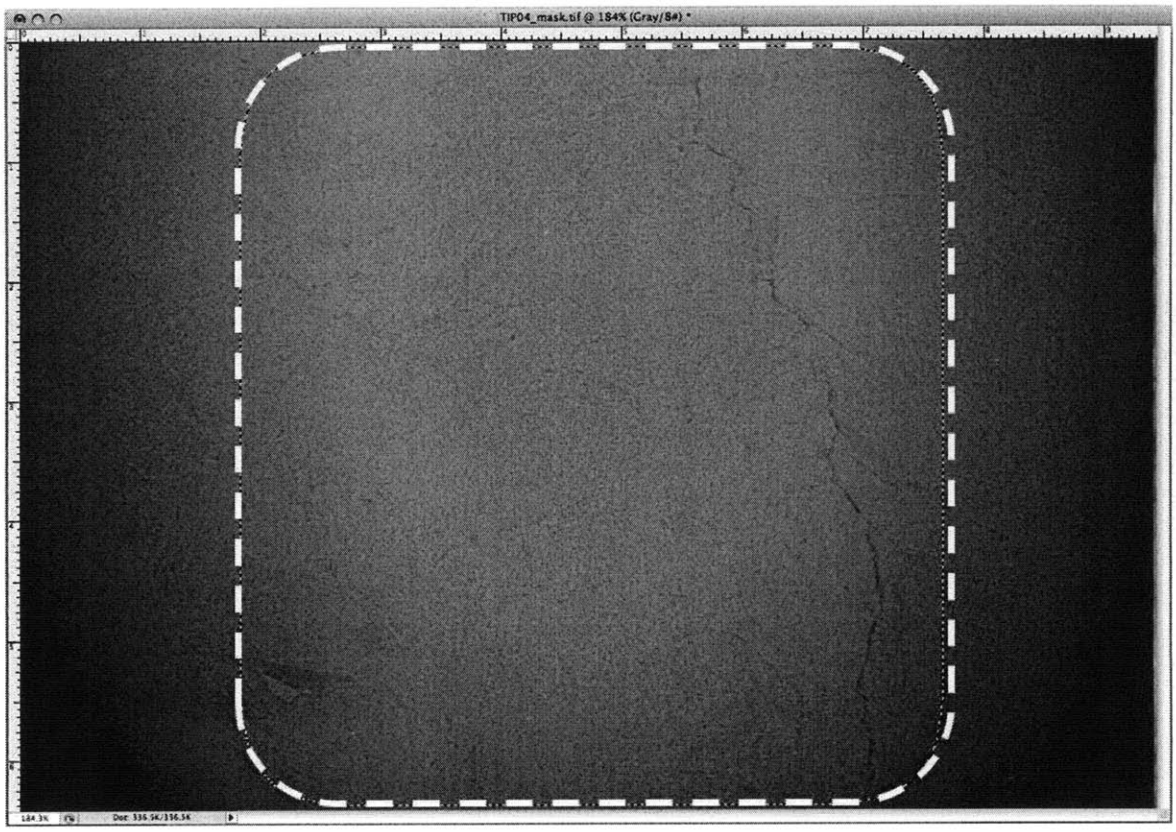

Figure A-2: Feathering the edges rounds the sharp edges of the rectangular selection.

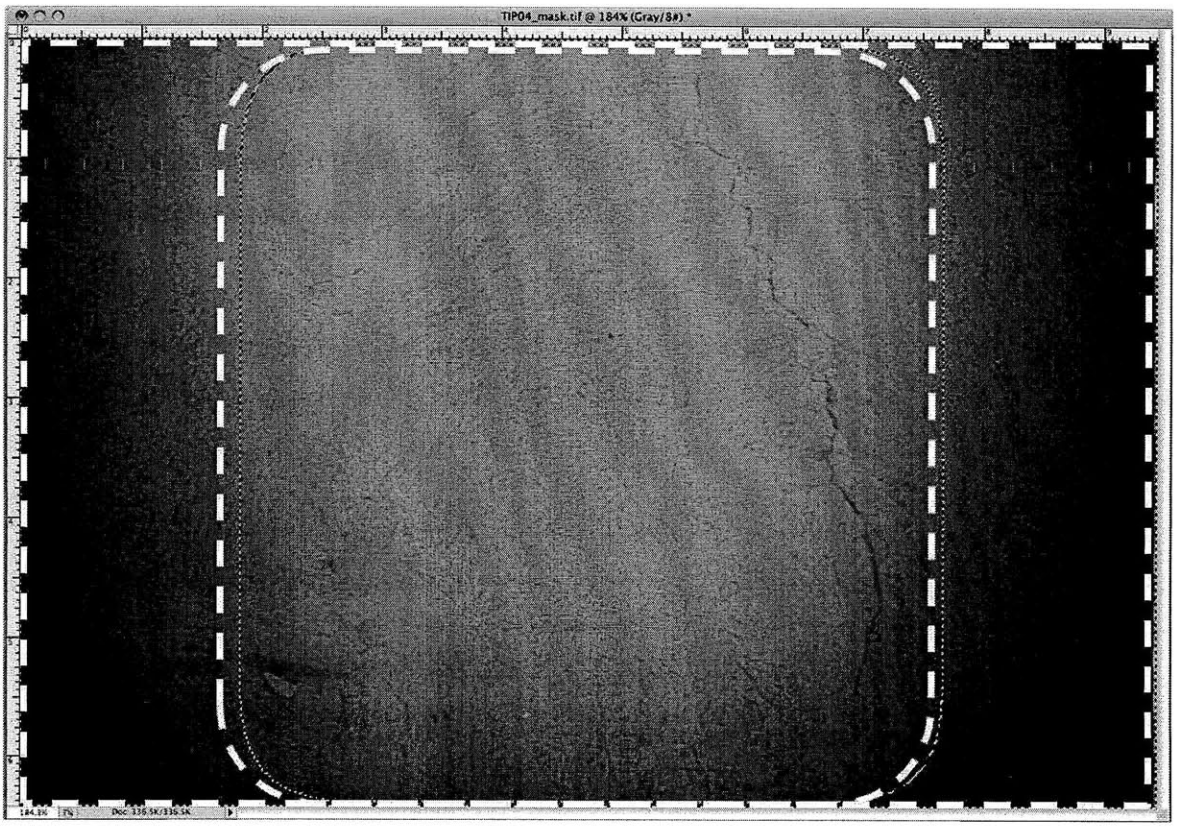

Figure A-3: Inverse Selection. The area outside of the rectangle is now selected.

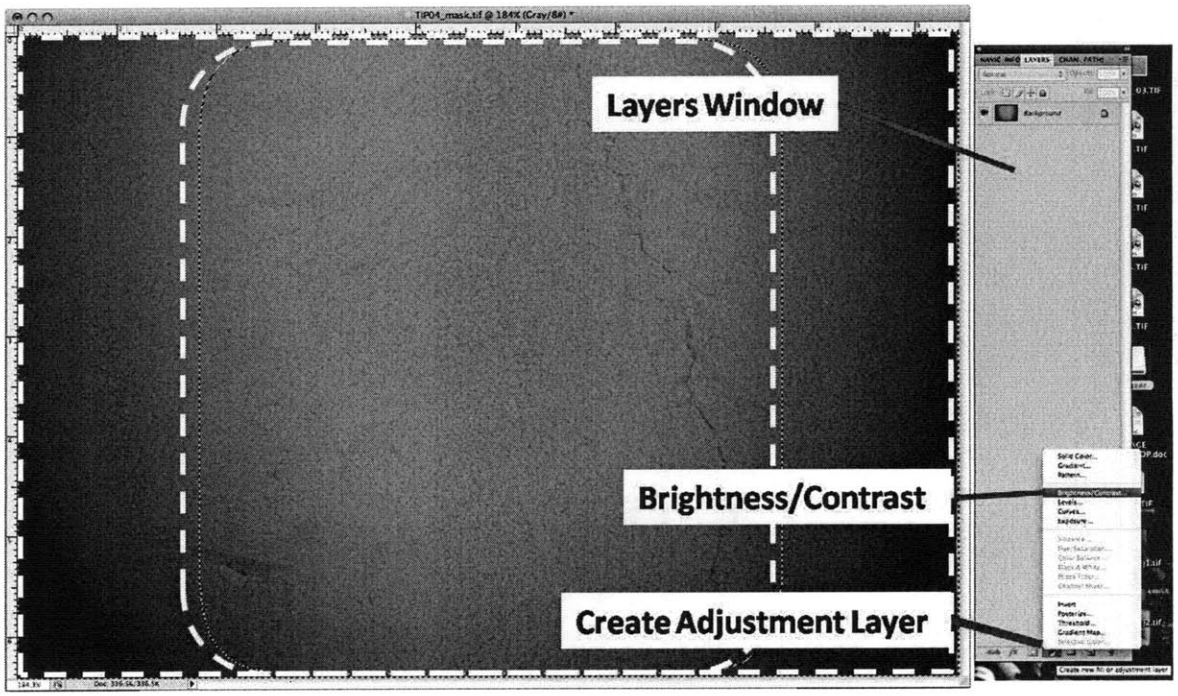

Figure A-4: An Adjustment Layer is created by selecting the Brightness/Contrast option in the Create Adjustment Layer button at the bottom of the Layers Window.

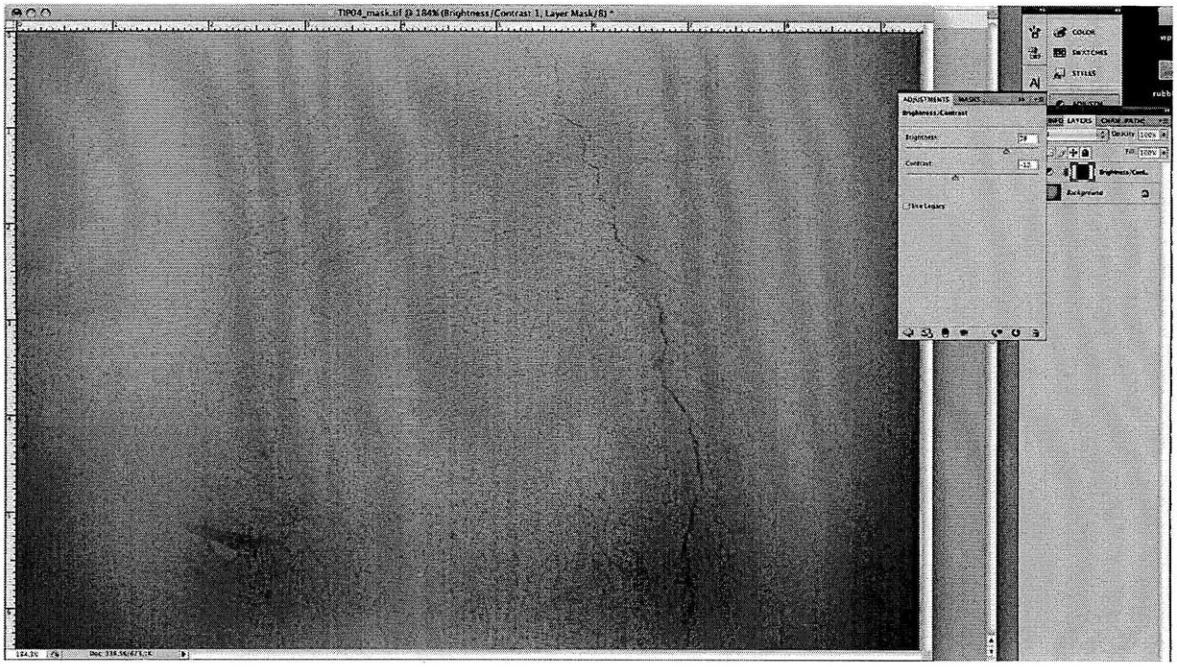

Figure A-5: The spotlighting has been reduced, and the crack is now more visible as the only dark region in the image.

If desired, this Adjustment Layer is then drag/dropped onto multiple images with the same spotlighting problem. All layers are merged using the Merge command to stamp the Adjustment Layer on top of the original image.

Microstructural features of interest are noted, and as well as an particular aspects of the feature to emphasize. In this image (Figure A-5), the crack down center of the image is the most interesting feature. Reducing the spotlighting has better defined the crack by helping it to stand out as the darkest part of the image.

If desired, the overall Image Brightness and Contrast are adjusted until the features of interest are delineated (Image → Adjustments → Brightness/Contrast; see in Section A.2.1: "Brightness/Contrast Adjustment" for an explanation of the Brightness/Contrast adjustment.)

A.2 Collaged Images

Two images are opened, as well as a new blank Photoshop document (called a "canvas"; File → New). The canvas should be approximately large enough to hold all of the images after they have been stitched together.

Both images are drag-and-dropped onto the canvas with the mouse. The first image will land on its own layer, and the second image will land on a layer above the first (Figure A-6).

The second layer to is reduced to 50% opacity, then the overlapping portions of the images are aligned (Figure A-7) by dragging the second image over the first until features align.

The second layer is then restored to 100% opacity.

The layers are blended. (Edit → Auto-Blend Layers → Panorama. Both layers should be selected; Figure A-8). Depending on how the images overlap, blending is often improved when four images that meet at a corner are blended; thus, blending more than two aligned images at once may be optimal.

The layers are merged using the Photoshop Merge command; this will stamp the contents of all selected layers onto a single layer. If necessary, spotlighting is corrected and Brightness/Contrast is adjusted as indicated in Section A.2.1.

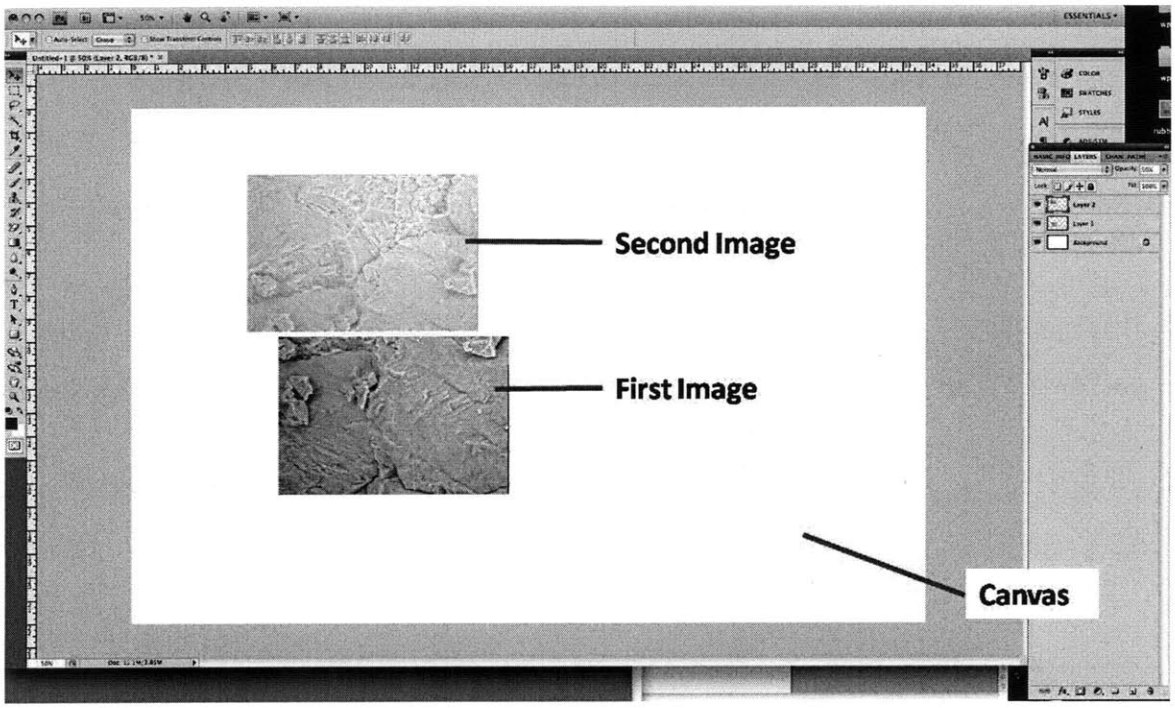

Figure A-6: The first and second images have been dropped onto the canvas. The layer window at right indicates a layer each for the canvas, first image, and second image. The layer with the second image is visible (highlighted in blue); its opacity has been reduced to 50% in order to facilitate alignment of overlapping features in the next step.

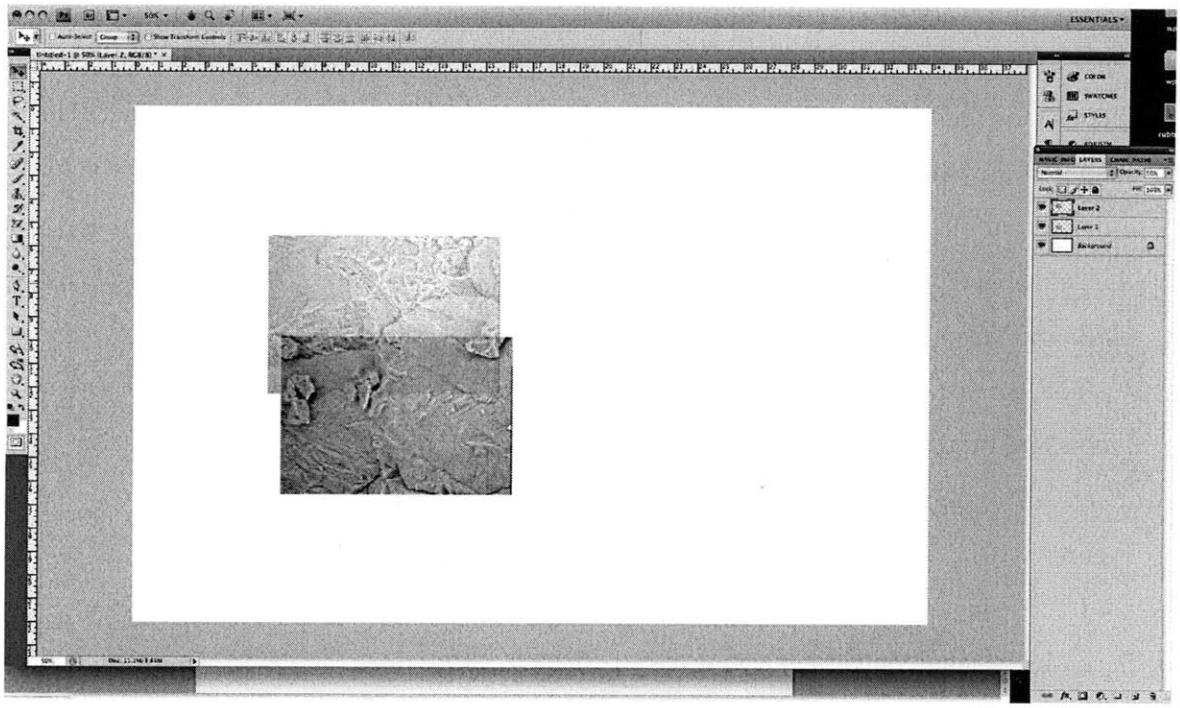

Figure A-7: The second layer dropped onto the palette is at the top. In the layer palette, the opacity of this layer has been reduced to 50%.

A.2.1 Brightness/Contrast Adjustment

Adjusting the Brightness/Contrast of an image allows microstructural features such as microcracks and spalling to be seen more easily. The function essentially makes dark areas darker, and light areas lighter – or vice versa; the user "Plays" with the function until the features of interest have reached the desired visibility.

An understanding of the image histogram is key to understanding the mechanism employed when the user executes a Brightness/Contrast adjustment. The image histogram displays the distribution of tones in an image (See Figure A-9). The tones ("Levels") are plotted along the x-axis, and the corresponding number of pixels along the y-axis. Black (Level 0) plots on the leftmost end of the x-axis, and white (Level 256) plots on the rightmost end. The various shades of gray lie between black and white (Levels 1 through 255). If desired, for color images, a histogram of each of the three RGB color channels (i.e., the color red, the color green, and the color blue) may be extracted and viewed separately. However, this project chiefly involves black and white images.

The Brightness/Contrast tool works by changing the tones of all the pixels in the image. Increasing brightness shifts all the pixels to a lighter tone. This shift can be easily seen on the image histogram as a shift of all tones towards the right (i.e., towards white at Level 256; see Figure A-10).

Decreasing brightness shifts all tones towards the left (i.e., towards black at Level 0). Similarly, increasing contrast exaggerates all tones by stretching the histogram in both directions (See Figure A-11).

While applying a change in Brightness/Contrast, the image must be closely monitored for clipping of highlights and shadows. "Clipping" a highlight and/or shadow simply refers to moving the tones all the way to either black (Level 0) or white (Level 256), and manifests as extreme lightening or darkening of the image.

The "best" brightness/contrast adjustment for each image depends on the features of interest in the image. Ultimately, the adjustment may be a combination of an increase/decrease in brightness, and an increase/decrease in contrast. For the image in Figure A-12, the final adjustment accentuates the edges of the rubble in the center, as well as the shadows the rubble casts.

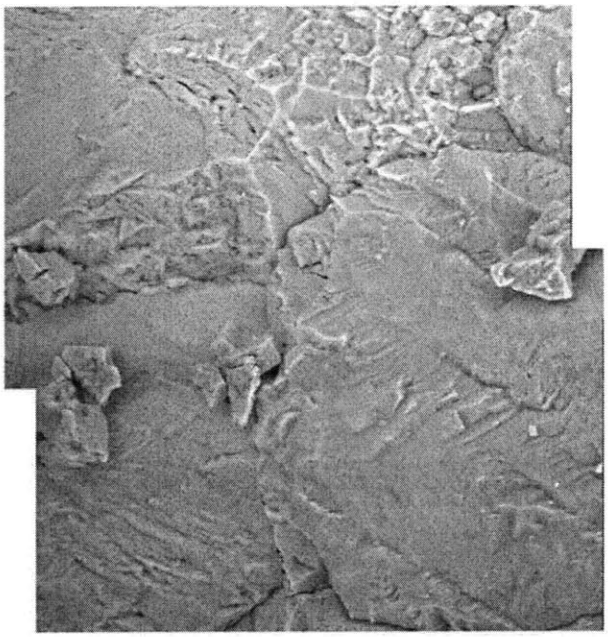

Figure A-8: Auto-Blend seamlessly blends the aligned layers.opacity of this layer has been reduced to 50%.

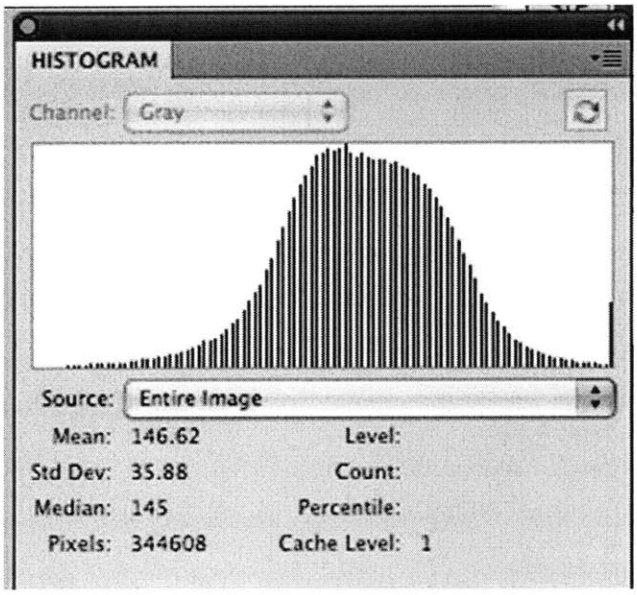

Figure A-9: The image histogram plots tones (from black to white) on the x-axis against number of pixels, on the y-axis.

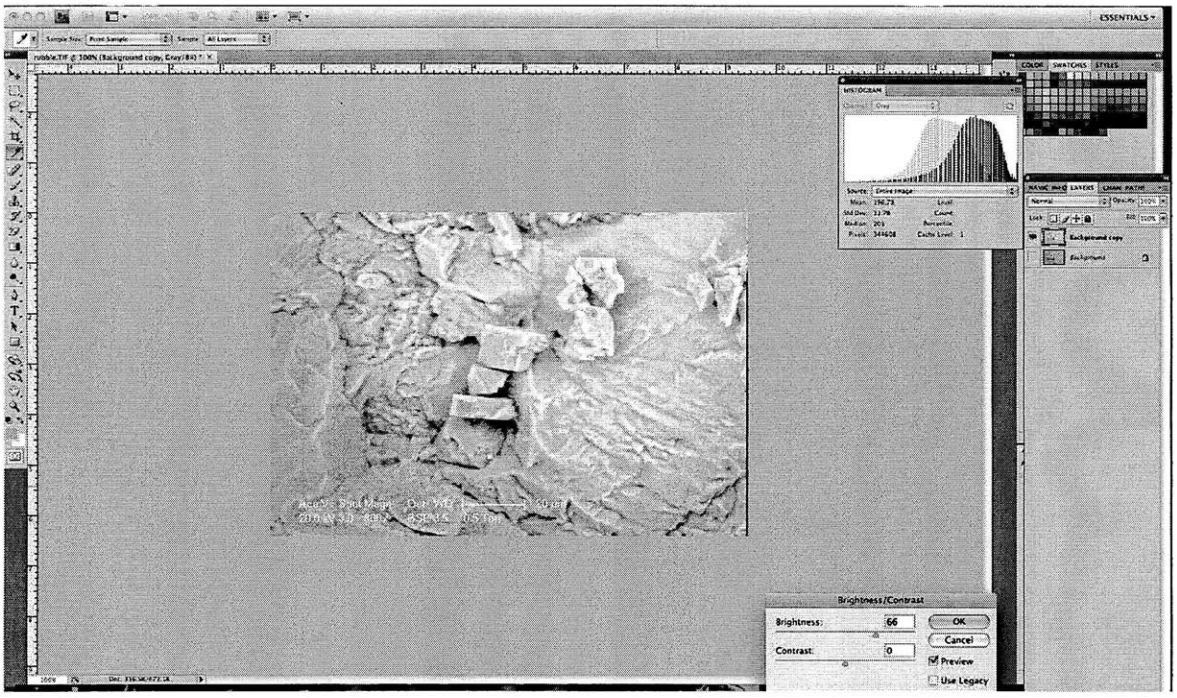

Figure A-10: The histogram in the upper right corner indicates tonal distribution before increasing brightness (grayed out distribution) and after increasing brightness (darker distribution). The tones of all pixels have increased towards white at Level 256.

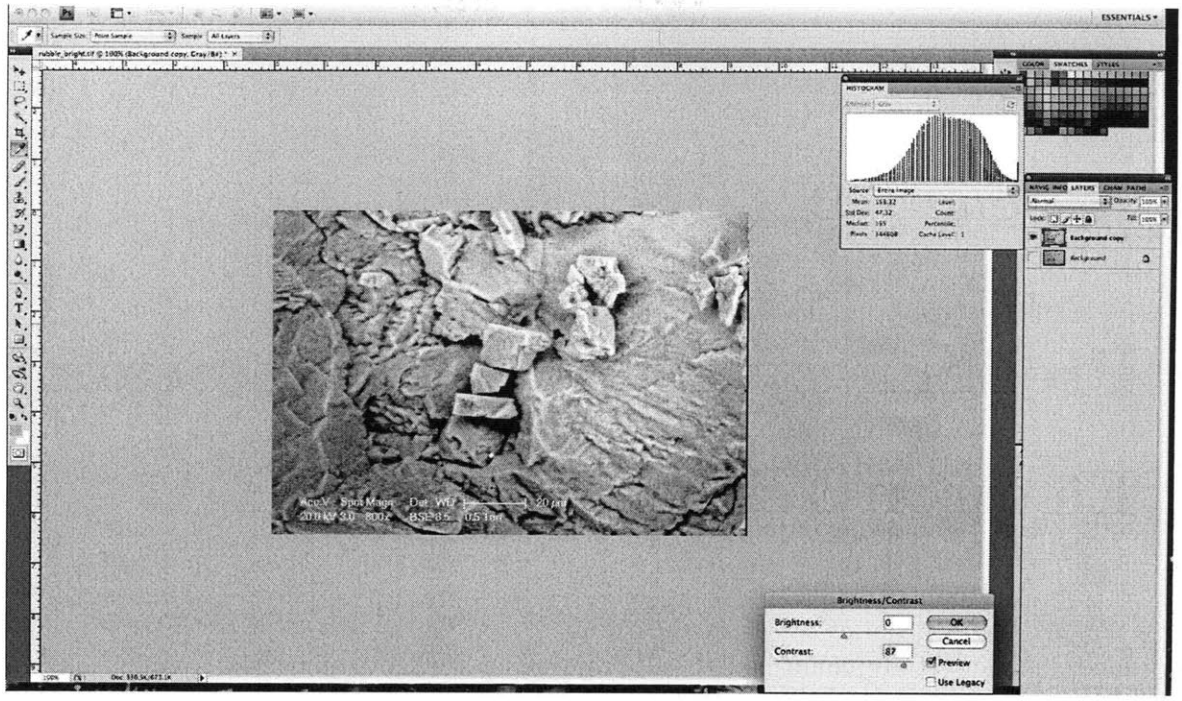

Figure A-11: The histogram in the upper right corner indicates tonal distribution before and after increasing contrast. The distribution has been "squished" towards the extremes (more pixels now have tones at the white (Level 256) and black (Level 0) ends of the distribution.

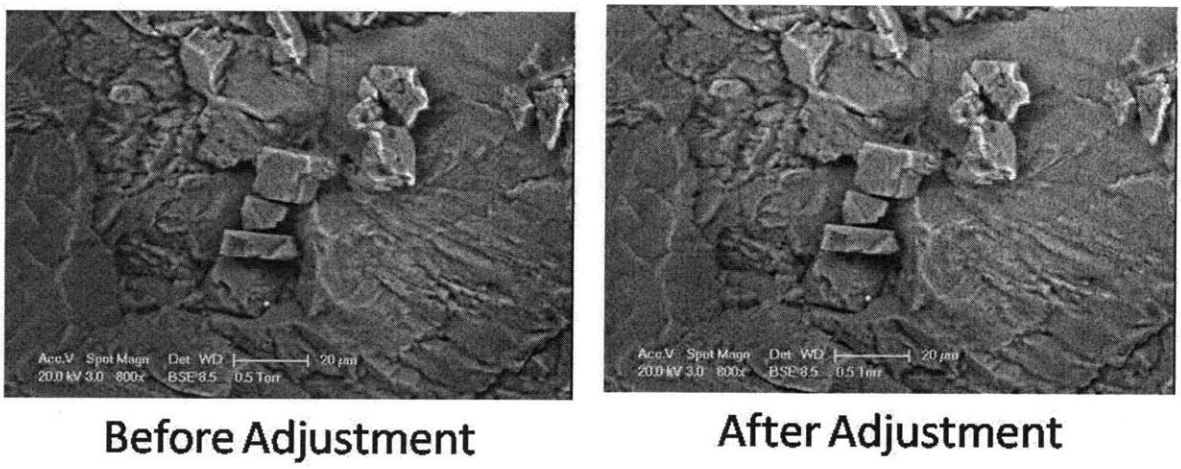

Figure A-12: The final brightness/contrast adjustment accentuates the edges of the rubble in the center, as well as the shadows the rubble casts

Appendix B

Preliminary Environmental Scanning Electron Microscopy (ESEM)

A preliminary study confirmed the appropriateness of environmental scanning electron microscopy (as opposed to standard scanning electron microscopy) for the investigation. This preliminary investigation was conducted as a first step towards investigating the appropriateness of ESEM. The image quality obtained with ESEM was improved upon in later parts of the study and with more practice on the ESEM in the calibration of the microscope settings for a particular specimen. Nevertheless, some important process zone microstructural information is visible in the preliminary images, and is reported in this section.

Prior to the investigation reported in the main section of this thesis, a marble sample with pre-existing flaw was loaded until white patching was visible near the tips of the flaw. Two of the three established microcracking identifiers (intergranular cracking and spalling, but not intragranular cracking) [73] were visible athigh magnification in ESEM (Figure B-1).

These identifiers (Integranular Cracking, Spalling Zone) were also visible under standard SEM, and originally classified by Wong 2008.

Integranular cracking (Figure B-2) was indicated by a long, connected and often winding crack on the specimen surface. This crack typically follows grain boundaries, and differentiates itself as a widening of the grain boundary.

Spalling was usually indicated by an irregular, but triangular impression or series of impres-

sions (Figure B-3).

Intragranular cracking manifests as short, straight cracks entirely contained by grain boundaries, but was not positively identified in the preliminary investigation. However, later investigation on a separate specimen revealed intragranular cracking (Figure 4-17).

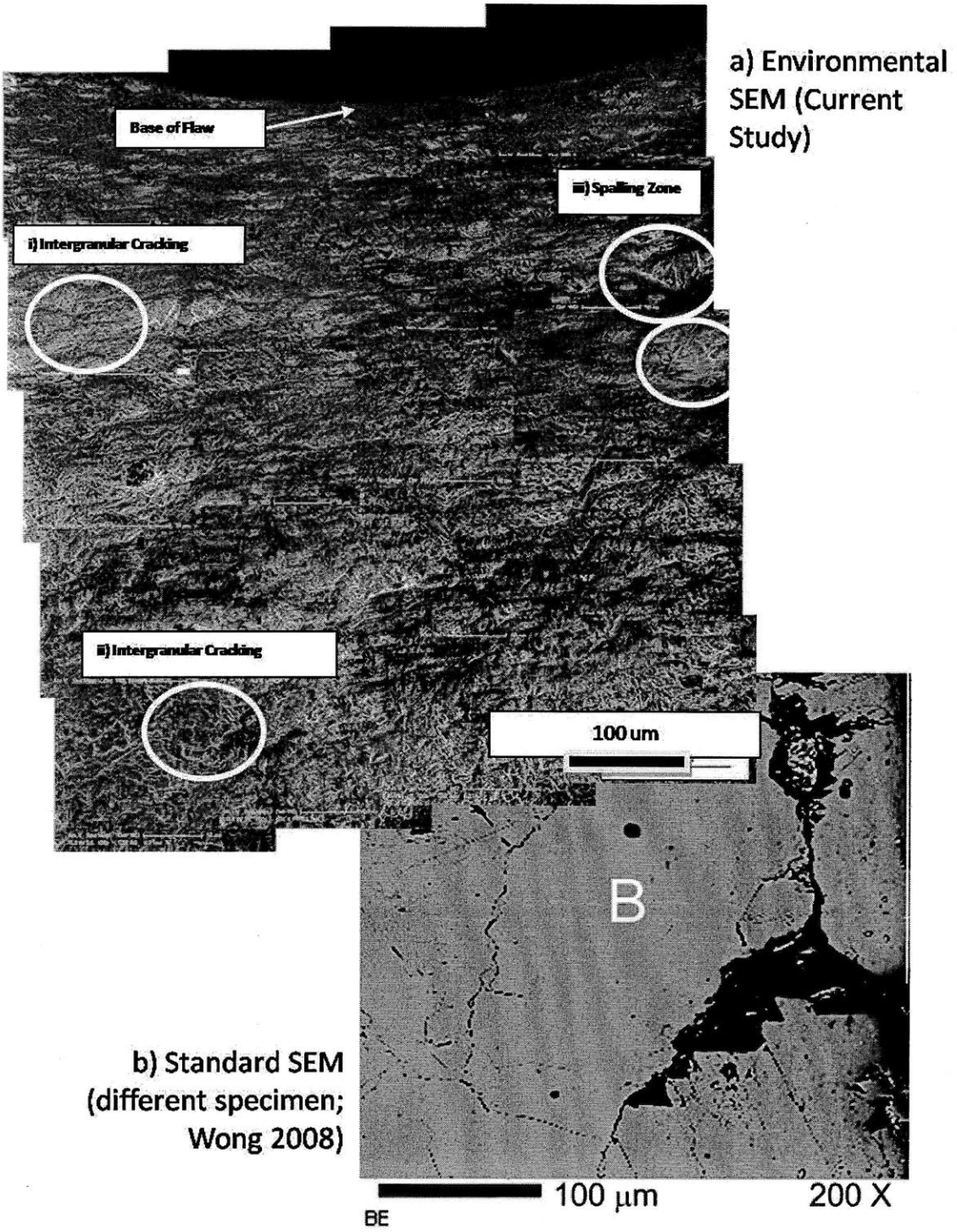

Figure B-1: A comparison of an ESEM image and standard SEM image. ESEM reveals two standard process zone microstructural features: spalling, and intergranular cracking. Detail of these features is provided in following images.

i)Intergranular Cracking

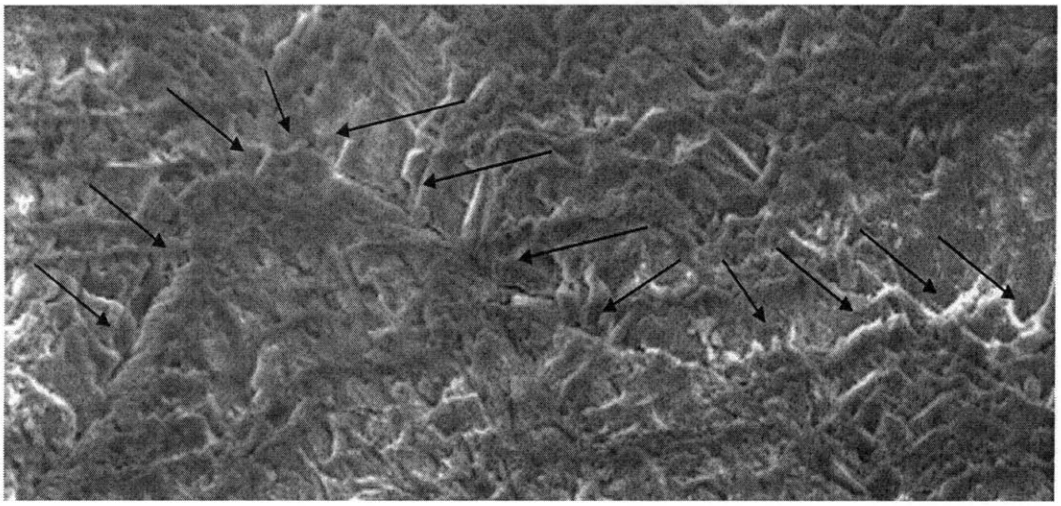

ii) Intergranular Cracking

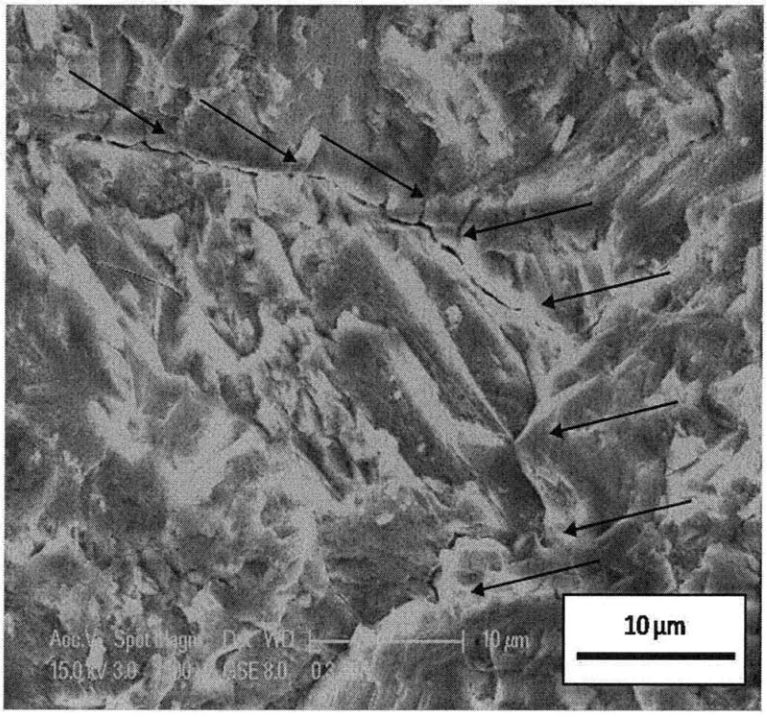

Figure B-2: Detail of (i) and (ii) in Figure B-1. Extended cracking between marble grains is visible on specimens. The tortuous crack path is indicated by arrows.

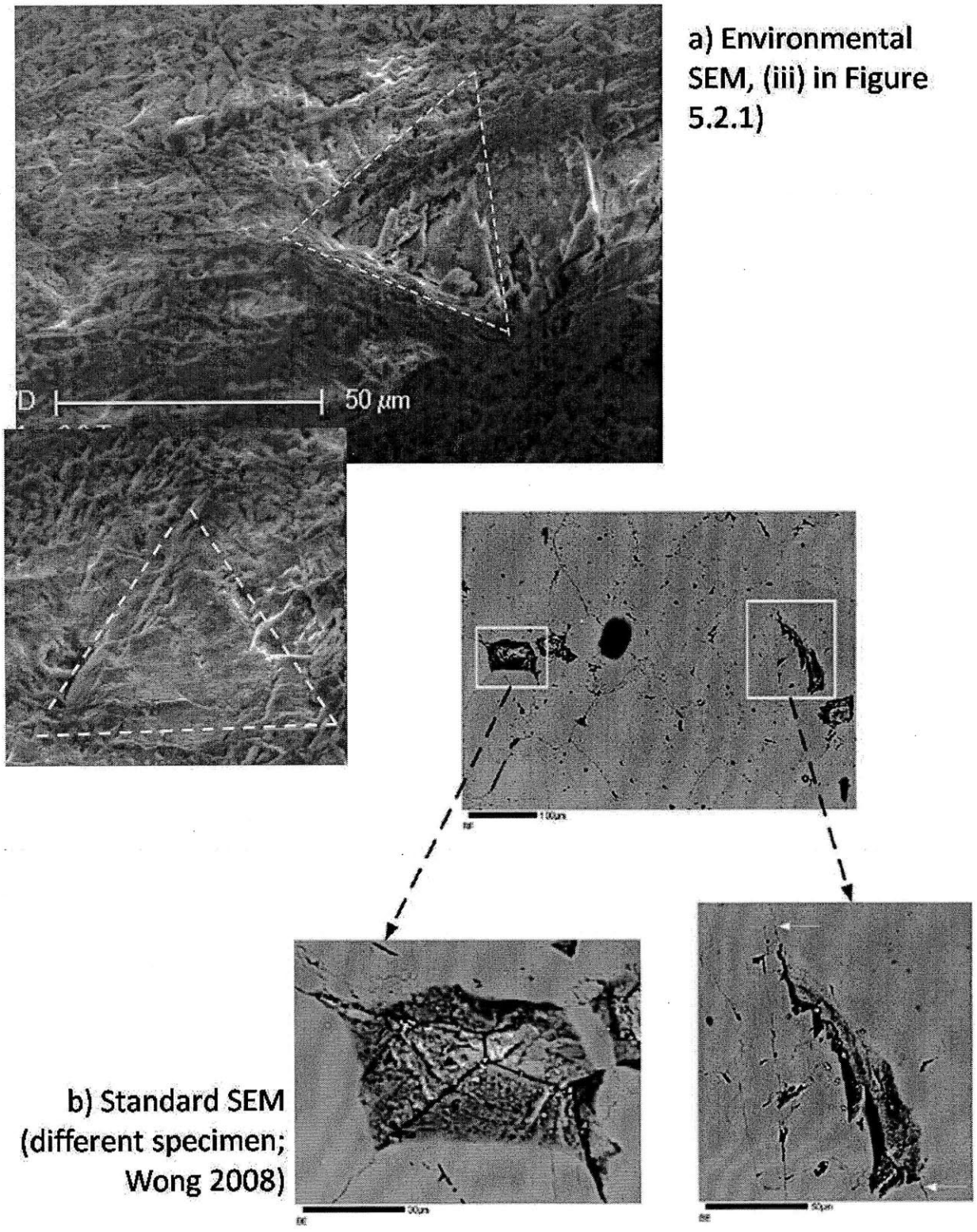

Figure B-3: Detail of spalling zones, (iii) in Figure B-1.. Spalling, or stress-induced impressions on the surface, is visible on both the unpolished ESEM sample, left, and polished SEM samples, right [Wong 2008].